Synthesis and Coordination of the Arylazo Ligands 1-(2-pyridylazo)-2-phenanthrol and 1-(8-quinolynazo)-2-phenanthrol

Robin A. Taylor, BSc.

Submitted in partial fulfilment of the requirements
for the degree of Master of Science

Faculty of Mathematics and Science, Brock University
St. Catharines, Ontario

Abstract

The use of ligands 1-(2-pyridylazo)-2-phenanthrol and 1-(8-quinolinazo)-2-phenanthrol has afforded twelve new complexes that feature many different structural, magnetic, and electronic properties.

Chapter one deals with the aspects of materials chemistry which are pertinent to the material presented in this thesis. This includes inorganic chemistry, magnetism, luminescence, and redox active ligands. The second chapter includes the experimental details of all the complexes and ligands presented herein. The main body of this work has been split into three parts. The first part presented in chapter three includes complexes of 1-(2-pyridylazo)-2-phenanthrol with the following transition metals [V(V), Cu(II), Co(II), Ru(II), Fe(II) and Fe(III)]. Of particular interest in this chapter is the Co(II) complex which exhibits thermal spin-crossover, and the Fe(II) complexes which offer interesting structural properties including a structural phase transition.

The second part (chapter four) examines three lanthanide complexes (Gd, Tb, and Dy) with the ligand 1-(2-pyridylazo)-2-phenanthrol. These complexes feature intense absorptions in the visible region which results in these complexes having dye-like properties. Of particular note is the luminescence studies performed on these complexes.

The final part (chapter five) of the work presented examines the synthesis and characterization of the ligand 1-(8-quinolinazo)-2-phenanthrol, and it's coordination chemistry (Fe(II), and Co(III)). The ligand offers quasi-reversible ligand centered reductions at low potentials, which should offer the first step in the synthesis of valence-tautomer or charge-transfer complexes.

Contents

List of Figures

List of Tables

List of Schemes

List of Publications

Chapter 3

Taylor, R. A.; Lough, A.J.; Poddutoori, P.K.; Lemaire, M.T Structural features and electronic properties of a cupric complex with redox active 1-(2-pyridylazo)-9-phenanthrol (papl). *Polyhedron*, **2016**, *108*, 74-79.

Taylor, R. A.; Lough, A.J.; Lemaire, M.T. Spin-crossover in a homoleptic cobalt(II) complex containing a redox-active NNO ligand. *J. Mater. Chem. C*, **2016**, *4*, 455-459.

Taylor, R. A.; Lough, A.J.; Poddutoori, P.K.; Seda, T.; Lemaire, M.T. Di- and trivalent iron complexes with redox-active 1-(2-pyridylazo)-2-phenanthrol (papl). *Submitted to Polyhedron (Under Revision)*, **2016**.

Chapter 4

Taylor R. A.; Cibian, M; Yadav, J; Silverstein, H. J.; Wiebe, C. R.; Hanan‡, G. S.; Lemaire M. T. Homoleptic lanthanide complexes containing a redox-active ligand and the investigation of their electronic and photophysical properties. *Manuscript in preparation*, **2016**.

Abbreviations

AC	Alternating current
Arylazo	Azo-aromatic
CFT	Crystal field theory
CV	Cyclic voltammetry
DC	Direct current
DCM	Dichloromethane
DFT	Density functional theory
DMF	Dimethylformamide
DPV	Differential pulse voltammetry
$\mathbf{e^-}$	electron
EPR	Electron paramagnetic resonance
ESI	Electrospray ionization
FT-IR	Fourier transform infra-red
HOMO	Highest occupied molecular orbital
ILCT	Intra-ligand charge transfer
IR	Infra-red

LIESST	Light induced spin state trapping
LFT	Ligand field theory
LMCT	Ligand-to-metal charge transfer
Ln	Lanthanide
LUMO	Lowest unoccupied molecular orbital
M	Transition metal
MLCT	Metal-to-ligand charge transfer
NMR	Nuclear magnetic resonance
nr	Non-reversible
O_h	Octahedral ligand field
PAN	1-(2-pyridylazo)-2-naphtholate
PAPL	1-(2-pyridylazo)-2-phenanthrol
pXRD	Powder X-ray diffraction
QAPL	1-(8-quinolinazo)-2-phenanthrol
qr	Quasi-reversible
RAL	Redox active ligand
Redox	reduction-oxidation
SMM	Single molecule magnet
SOMO	Singly occupied molecular orbital
SQUID	Superconducting interferance device
TD-DFT	Time dependent density functional theory
THF	Tetrahydrofuran

UV-Vis	Ultraviolet-visible spectroscopy
VSM	Vibrating sample magnetometer
VT	Valence tautomerism

Symbols

$\hat{L}$	Orbital angular momentum operator
$\hat{S}$	Spin angular momentum operator
g	Gyromagnetic ratio
H	External magnetic field
$\hat{H}$	Hamiltonian
N	Number of particles
E	Energy
T	Temperature
P	Probability
k	Boltzmann constant
$\%T$	Percent Transmittance
$\%$	Percent
S	Spin
M	Magnetization
C	Curie constant

t	time
$E_{1/2}$	Half wave potential
δ	Chemical shift
δ	Isomer shift
ΔE_Q	Quadrupole splitting
Δ_o	ΔE between e_g^* and t_{2g} orbitals in O_h
ϕ	Weiss constant
ϵ	Molar extinction coefficient
χ	Magnetic susceptibility
χ_M	Molar magnetic susceptibility
$\hat{\mu}$	Magnetic moment
μ_B	Bohr Magneton
λ	Wavelength
λ_{max}	Maximum absorbance value

Chapter 1

Introduction

1.1 Coordination Chemistry

The chemistry of transition metals differs from that of the main group elements; as they form complexes which early chemists were not able to describe using the organic methods available at the time. The first theory of a coordination chemistry, that resembles modern theory, was purposed by Alfred Werner in 1893[1] to explain the results of his study on Co(III)-ammonia complexes. His theory has three important postulates: first, the number of groups attached to an atom (coordination number) does not need to be equal to its oxidation number (oxidation state), second, every element tends to satisfy both its coordination number and oxidation state, and third, the coordinate bonds are directed to fixed points in space and therefore can be treated by applications of structural principles. To elaborate on

the third postulate, Werner believed that in complexes such as $[Co(NH_3)_6]^{3+}$ the ammonia ions are situated symmetrically about the cobalt ion. Werner offered three structural configurations: 1)planar hexagon, 2)trigonal prism, or 3)octahedron. The first two were proved incorrect, therefore, the correct structure was determined to be an octahedron. In this way Werner was able to define the structure of many coordination compounds twenty years before the invention of X-ray crystallography.

1.1.1 Ligand Field Theory

After Werner the next major advance in coordination chemistry was crystal field theory (CFT), which utilizes group theory to describe how the degeneracy of the metal orbitals is broken by the electric field of surrounding point charges. CFT uses the symmetry of a molecule to determine the point group to which a molecule belongs. The point group allows for the determination of the relative energies of the metal orbitals, which can then be used to simulate and interpret various properties of a system. CFT evolved into ligand field theory (LFT)[2] which replaces the surrounding point charges with the ligand orbitals, allowing for LFT to describe the bonding in coordination complexes.

The Octahedral point group is one of the more common point groups that is encountered in transition metal complexes (shown in figure 1.1 left). For a transition

metal with this symmetry, there are six coordinate bonds that are of equal length, and equally spaced around the metal ion.

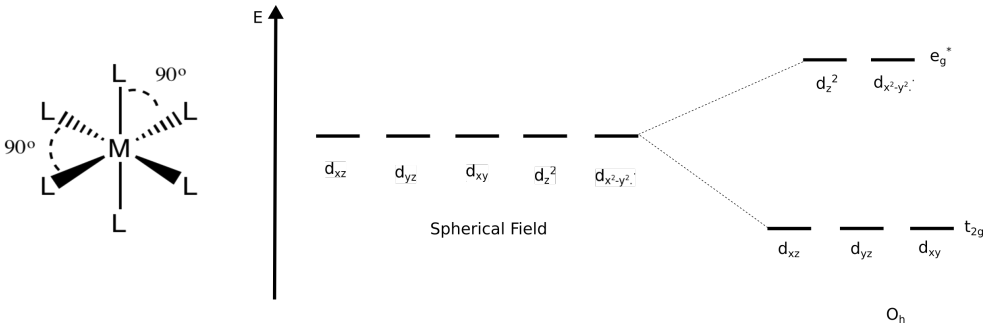

FIGURE 1.1: d-orbitals of a molecule with O_h symmetry: The diagram on the left describes a general complex belonging to the O_h point group. M is a transition metal and L is a monodentate ligand. The energy diagram on the right shows how the d-orbitals split when moving from a spherical to an octahedral ligand field.

The location of coordinated ligands about the metal center causes the five d-orbitals of the metal ion to split into two sets of degenerate orbitals. The three lower energy orbitals are of t_{2g} symmetry; they consist of the d_{xy}, d_{xz}, and d_{yz} orbitals. The higher energy orbitals are of e_g^* symmetry; consisting of the $d_{x^2-y^2}$ and d_{z^2} orbitals (figure 1.1 right). The reason for the energy difference is that the orbitals of e_g^* symmetry point directly along the coordinate bonds, and overlap with the orbitals of the ligands resulting in a large amount of e^-/e^- repulsion. The orbitals of t_{2g} symmetry are pointed between the Cartesian axes of a molecule, and therefore overlap with the orbitals of the ligands is limited, limiting e^-/e^- repulsion.

The splitting of the d-orbitals in a transition metal complex has major consequences for the ground state electronic structure. In particular, the O_h transition

metals with $d^4 - d^7$ electronic configurations can have two ground state electronic configurations. In d^1 through d^3 complexes there is only one possible ground state, which is formed from placing electrons with parallel spins in the lower energy t_{2g} orbitals. When a fourth d-electron is added there are two possible states, and the one which is present is due to two energetic constraints, the pairing energy; the energy cost of placing two electrons in the same orbital, and the splitting energy; the energy difference between orbital levels. The splitting energy is described by the spectrochemical series, which is partially shown in figure 1.2. Weak field ligands, such as I^- and NO_3^-, cause only a weak splitting of the d-orbitals which results in the high spin state being the ground state. On the other extreme of the spectrochemical series, strong field ligands such as CN^- and CO produce large energy gaps between the degenerate orbital sets, which results in the metal ion being in the low spin state. The difference between a high spin state and the low spin state for a d^6 ion is shown in figure 1.3.

$I^- < Br^- < SCN^- < Cl^- < F^- < OH^- < H_2O < NCS^- <$ bipy $<$ phen $< NO_2^- < CN^-$

FIGURE 1.2: The spectrochemical series: From small to large splitting (left to right)

Very few real systems that are actively studied in coordination chemistry belong to high symmetry (O_h, Td, or Is) point groups, rather they belong to points groups with lower symmetry. It is important to note here the difference between geometry, and symmetry. Many molecules that are described as having octahedral like (six coordinate) geometry, but are of low symmetry point groups such as C_2. In these

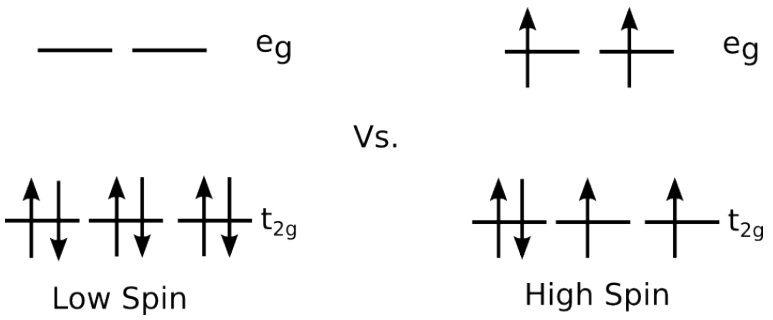

FIGURE 1.3: High spin state ($S = 2$) versus low spin state ($S = 0$) in an octahedral ligand field.

cases, only a rough estimation of the relative orbital energy can be assumed by using the higher symmetry case. To determine a more accurate description of the electronic structure chemists today use computational methods (DFT, ab initio, etc).

1.1.2 The Jahn-Teller Effect

In molecules of high symmetry, such as those which belong to the octahedral point group, orbital degeneracy in the ground state electronic configuration is common (for octahedral complexes this is d^1, d^2, d^4, low spin d^5, high spin d^6, d^7, and d^9.) In these electronic configurations one of the axes, which is termed the Jahn-Teller axis (always labelled z) distorts (usually by elongation), which causes the degenerate orbitals to split[3]. This allows for the degeneracy in the ground state to be lifted (figure 1.4). In octahedral complexes, the Jahn-Teller effect is most pronounced in the high spin d^4, low spin d^7 and d^9 configurations, and is prominent in Cu(II) complexes[4]. This is due to the electronic degeneracy being located within the

e_g^* orbitals. As the e_g^* orbitals point directly towards the ligands of the complex, there is a greater distortion of the bond lengths, which has a major effect on the stabilization of the molecule, as the e_g^* orbitals split enough to lift the degeneracy in the ground state. In contrast, for complexes where the degeneracy is confined to the t_{2g} orbitals the Jahn-Teller effect is much less pronounced. This is due to the t_{2g} orbitals being located off the Cartesian axes of the molecule, and in lower contact with the orbitals of the ligand. The elongation of the Jahn-Teller axis only weakly splits the degenerate t_{2g} orbitals offering less stability.

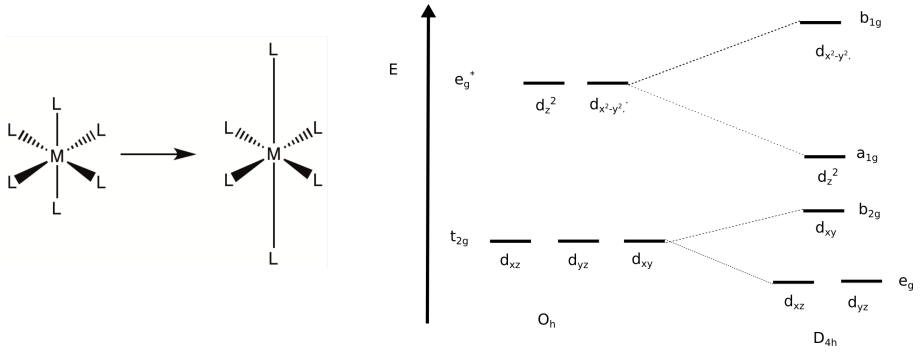

FIGURE 1.4: The Jahn-Teller Effect: Left: The octahedral complex ML_6 with a degenerate ground state, will distort (either compress or extend which is shown) the Jahn-Teller axis. Right: The energy diagram of a molecule with O_h symmetry which has undergone Jahn-Teller distortion.

1.2 Lanthanide Ions

Lanthanides(Ln) are the series of ions with atomic numbers 57 through 71 (or lanthanum through lutetium, inclusive). Lanthanides are f-block elements (with the exclusion of lanthanum) as they correspond to the filling of the valence f-orbitals, which differ from d-orbitals as they are shielded from the effects of the

ligand field. As such the orbitals of the lanthanide ions are only weakly split, making all lanthanide ions high spin, following Hund's rule.

In general lanthanide ions are much larger when compared to transition metal ions (Atomic radii of 233pm for Gd compared to 152pm for Co). As such they accept a higher number of coordinate bonds when compared to transition metals. Generally, complexes of lanthanide ions form 8-9 coordinate bonds in coordination complexes. Lanthanide ions are most commonly found with an oxidation state of 3+, and are hard Lewis acids forming stable complexes with oxygen donors more readily than nitrogen donors. In addition, coordination with monodentate ligands is difficult as coordinated aqua ligands are difficult to displace from the coordinate sphere of lanthanides. However, for polydentate ligands the chelate effect allows for the removal of water from the coordination sphere, and stable complexes to be formed.

Also of note is that lanthanide ions possess many interesting properties, including a large magnetic anisotropy which has made them useful in the study of single molecule magnetism[5], they are also luminescent[6] making them useful tools in the area of materials science. Finally, different lanthanide ions upon chelation to identical ligands tend to form complexes that are iso-structural[7][8]. This allows for the complex material properties of lanthanide complexes to be studied in depth using structural analogues which do not possess the more complex properties (i.e. Gd being used to estimate the strength of magnetic coupling in SMM complexes of Tb or Dy).

1.3 Magnetism

There are many useful textbooks, and sources of information on the subject of magnetism, and molecular magnetism, which have been used in the following section. [9][10][11]

1.3.1 A Physical Basis

Magnetic properties of materials are quantum mechanical in nature, and arise from the operators of orbital angular momentum ($\hat{L}$) and spin angular momentum ($\hat{S}$) of the electrons in a material. In quantum mechanical terms the orbital angular momentum is an observable associated with the operators $\hat{L}$ and $\hat{L}_z$ for which there exist a set of quantum numbers for L^2 and for one of the directional components M_L,

$$\hat{L}_z Y_{LM}(\theta, \phi) = M_L \hbar Y_{LM}(\theta, \phi) \tag{1.1}$$

where $Y_{LM}(\theta, \phi)$ are the spherical harmonics and

$$M_L = L, (L-1), (L-2), ..., (-L) \tag{1.2}$$

Out of quantum mechanics a second angular momentum arises which is termed the spin (or intrinsic) angular momentum. This spin angular momentum which

has a set of quantum numbers of the nature,

$$S_z = m_s \hbar \tag{1.3}$$

which for a single electron, $m_s = \pm\frac{1}{2}$.

The combined angular momentum of the orbital and spin angular momentum both contribute to the magnetic moment of the atom which takes the form,

$$\hat{\mu} = -\mu_B(\hat{L} + g\hat{S}) \tag{1.4}$$

where g is the spin g-factor, a dimensionless factor which characterizes both the magnetic moment and gyromagnetic ratio of a particle (in this case an electron). The eigenvalues of the magnetic moment in the z-direction take the form,

$$\mu_z^L = -\mu_B M_L \tag{1.5}$$

for the orbital component, and

$$\mu_z^S = -g\mu_B M_s \tag{1.6}$$

for the spin component.

When an external magnetic field (H) in what is assumed to be in the z-direction, is applied to to a material, both components of the magnetic moments of the electrons in the couple interact with the field. The energy of the magnetic moment in the field is determined quantum mechanically by the Hamiltonian operator($\hat{H}$) which is expressed as,

$$\hat{H} = -\hat{\mu}H \tag{1.7}$$

The magnitude of the Hamiltonian parallel to field is,

$$\hat{H} = -(\mu_L + \mu_s)_z H = \mu_B(\hat{L}_z + g\hat{S}_z) \tag{1.8}$$

Boltzmann statistics tells us that in a sample the number of particles (N_i) that will have a particular energy value (E_i) when in thermal equilibrium at a certain temperature (T),

$$N_i = \frac{Ne^{E_i/kT}}{\sum_i e^{-E_i/kT}} \tag{1.9}$$

where k is the Boltzmann constant. The probability of this energy state is given by the Boltzmann probability factor which is simply,

$$P_i = \frac{N_i}{N} = \frac{e^{E_i/kT}}{\sum_i e^{-E_i/kT}} \tag{1.10}$$

The total magnetization of a sample is found by using a Boltzmann weighted sum,

$$M = N_A < \mu > \tag{1.11}$$

where N_A is the Avagadro number, and $< \mu >$ is the average magnetic moment of one molecule. This is found by applying the Boltzmann probability factor to each possible magnetic moment,

$$M = N_A \sum_i \mu_i P_i = N_A \frac{\sum_i \mu_i e^{E_i/kT}}{\sum_i e^{E_i/kT}} \tag{1.12}$$

1.3.2 Spin Multiplicity

Spin multiplicity is a quantum mechanical property which describes the number of degenerate spin states that are labelled by the total spin projection quantum number M_s. For molecules with multiple electrons the spin multiplicity takes a value equal to $2S + 1$, where S is the spin of a molecule. In addition the spin multiplicity is used to name the energy state of the molecule. If there is a spin multiplicity of 1, the molecule is in a singlet state, 2 it is in a doublet state, 3 it is in a triplet state, etc.

For example, in a system with two unpaired electrons, there are four possible states the electrons can take; ↑↑, ↑↓, ↓↑, and ↓↓. As electrons are indistinguishable, the two antiparallel states are indistinguishable as written, however, by taking both the symmetric and antisymmetric combination of these two states, we can form two distinguishable states ↑↓ + ↓↑ which has a $S = 1$ and ↑↓ − ↓↑ which has $S = 0$. So overall there are four possible states which the two electrons can be in; one with $S = 0$, and therefore a singlet state, and three with S=1 which form the triplet state.

1.3.3 Magnetic Susceptibility: Paramagnetism and Diamagnetism

When a magnetic field (H) is applied to a sample, the measured response is the magnetization. If a ratio of magnetization to applied field is made, it follows the differential equation,

$$\chi = \frac{\partial M}{\partial H} \tag{1.13}$$

where χ is a useful property that is termed the magnetic susceptibility. For a sample that lacks any sort of magnetic coupling, the magnetic susceptibility becomes a proportionality constant and the equation takes the form,

$$M = \chi H \tag{1.14}$$

and is said to have Curie behaviour if it follows the Curie law,

$$\chi = \frac{C}{T} \tag{1.15}$$

where C is the Curie constant. When intermolecular coupling (coupling between molecules) is present between paramagnetic centres the Curie law no longer holds. The amended law now termed the Curie-Weiss law is simply,

$$\chi = \frac{C}{T - \phi} \tag{1.16}$$

where ϕ is the Weiss constant, which for ferromagnetic coupling the constant $\phi < 0$ and for the anti-ferromagnetic case $\phi > 0$. If no coupling is present $\phi = 0$, and the limiting case of the Curie law is reached.

Magnetization comes from two sources. The first and greater in magnitude of the two is from the spin and orbital angular momentum of unpaired electrons in the material. The unpaired electrons can have many origins including organic radicals, transition metals, and lanthanides. The unpaired electrons have both orbital and spin angular momenta, which result in a net magnetic moment. This magnetic moment acts to concentrate the magnetic field lines of the applied field

inside the sample. In real materials the unpaired moments from many electrons are all randomly oriented and, therefore, the bulk magnetic moment sums to zero. However, when a magnetic field is applied, the individual magnetic moments align with their z-components preferentially parallel with the field, resulting in a net magnetic moment that is proportional to the field, which is called paramagnetism. The magnetic susceptibility arising in paramagnetic material as a result of the unpaired electrons is likewise called the paramagnetic susceptibility.

The second source comes from the paired electrons in the molecule. Since all molecules have paired electrons, it is always present. The Aufbau principle states that the lowest energy orbitals are filled completely before higher energy orbitals can be accessed. In addition, the Pauli Exclusion Principle states that only two electrons of opposite spin can occupy the same orbital. These full or closed orbitals produce an electronic charge that, in response to an applied magnetic field and as a result the applied field, is diverted toward the outside of the material. This diversion of the magnetic field, which is termed diamagnetism, is both temperature and field independent as well as additive, so therefore, can be corrected for with the use of the well documented Pascal constants.

1.3.4 The Van Vleck Equation

The Van Vleck equation which was first derived in 1932, can be used to calculate the molar susceptibility. Derived using Boltzmann statistics, it models the populations of the various energy levels by decomposing the expression for energy using a Taylor series,

$$E_n = E_n^{(0)} + HE_n^{(1)} + H^2E_n^{(2)} \tag{1.17}$$

assuming that the applied magnetic field H is not too large and the temperature is not too low, the expression for the molar magnetic susceptibility can be derived,

$$\chi_m = N_A \frac{\Sigma_n (\frac{(E_n^{(1)})^2}{kT} - 2E_n^{(2)}) exp(\frac{-E_n^{(0)}}{kT})}{\Sigma_n exp\frac{-E_n^{(0)}}{kT}} \tag{1.18}$$

in the simplest case, i.e. where there is only the spin-degenerate term ^{2S+1}A, if we take $E_s^{(0)} = 0$ to be the reference, the van Vleck equation simplifies to,

$$\chi_m = \frac{0.125g^2}{T} S(S+1) \tag{1.19}$$

1.3.5 Coupling Between Magnetic Centres

Paramagnetic molecules with more than one spin-containing centre can exhibit magnetic exchange coupling. This exchange coupling can either lead to a ferromagnetic interaction between spins or an antiferromagnetic interaction between spins. Two important mechanisms for exchange coupling in molecules are direct exchange, and superexchange.

Direct exchange is very strong at short distances and is the dominant mechanism of magnetic coupling in this limit. However, direct exchange decays rapidly with increased separation between magnetic centres. If there is a direct overlap of magnetic orbitals, the coupling between the magnetic orbitals is strongly antiferromagnetic (figure 1.5), and if there is no quantum mechanical overlap, the coupling between the magnetic centers is ferromagnetic and follows Hund's rule.

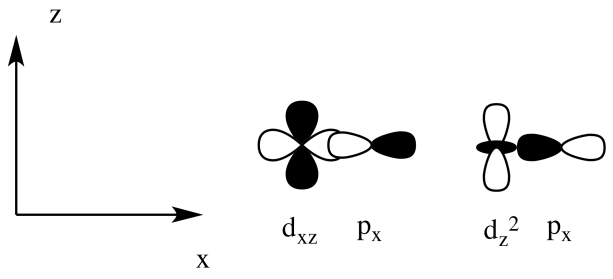

FIGURE 1.5: Direct Exchange Coupling Mechanism: Left: Antiferromagnetic coupling of the electrons due to quantum mechanical (orbital) overlap. Right: Ferromagnetic coupling

Superexchange occurs between two magnetic centers through an intermediate nonmagnetic atom or ligand. It can result in either an antiferromagnetic or ferromagnetic interaction depending on the geometry of the system (figure 1.6). It leads

to strong antiferromagnetic coupling when the angle made between the orbitals of the unpaired electrons subtended by the intermediary atom is 180 degrees. If the angle described is 90 degrees a strong ferromagnetic interaction occurs. Angles between the two maxima lead to weaker interaction and therefore weaker coupling between the two unpaired electrons.

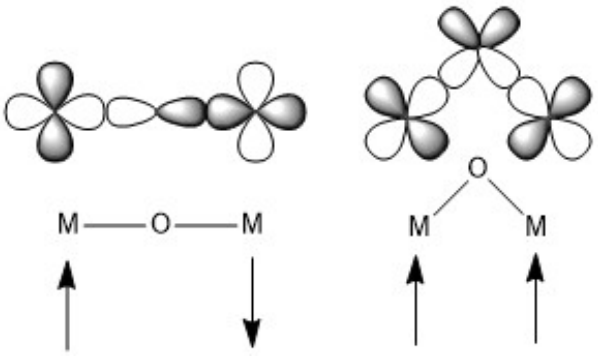

FIGURE 1.6: Superexchange Coupling Mechanism: Left figure shows a 180^o bond angle leading to antiferromagnetic coupling, and the right figure shows a 90^o bond angle leading to ferromagnetic coupling.

1.4 Molecular Magnetism

Unlike atomic materials which consist mainly of metal ions and oxygen, molecular magnets tend to lack (with a few exceptions[12]) the long range ordering that leads to physical properties, such as ferromagnetism/ferrimagnetism/antiferromagnetism.

Molecular magnets are either organic or coordination compounds that are synthesized using conventional wet chemistry, rather than the metallurgical processes

used to form atomic materials. The unpaired electron spins in molecular materials are de-localized throughout the molecular orbitals of the molecular magnet, which is built from the atomic orbitals of the individual atoms. This is in contrast with atomic based materials where the unpaired electrons, which contribute to the spin, reside entirely in the d-orbitals (or f-orbitals) of the metal ions. Molecular magnets have the same properties associated with the established atomic based magnets including coercivity and remnant magnetization, but in addition are usually soluble in organic solvents, and can possess other interesting properties not present in atomic magnets, such as conductivity, and luminescence.

The following section describes various phenomena that are unique to the area of molecular magnetism.

1.4.1 Spin Crossover

Spin crossover is one of the most interesting phenomena of molecular magnetism[13]. It is possible due to the splitting of the d-orbitals in a ligand field, which leads to two electronic ground states for d^4 through d^7 transition metals in an octahedral-like ligand field. In the special situation in which there is an intermediate ligand field, there is a possibility of having either the high spin or low spin state present depending on its environment. Manipulation of the environment, including changes in temperature, pressure or with light irradiation can result in a change of spin state.

1.4.1.1 Thermal Perturbation

First observed in the 1960's by Baker and Babonich [14], the complex $Fe(bpy)_2(NCS)_2$ was shown to undergo a thermally induced spin transition from high spin to low spin upon cooling. Over the next 50 years many more interesting complexes have been synthesized, which possess a thermally induced spin transition. Spin crossover is most commonly seen in complexes of Fe(II) and Fe(III)[13][15], though also (but rarely) in complexes of Co(II)[16],[17] Co(III)[18], Cr(II)[19][20], Mn(II)[21] and Mn(III) [22]. Most commonly probed for by variable temperature magnetometry, and most readily recognized in plots of $\chi_m T vs T$, several variations in spin crossover are formally recognized. Which type is present in a system is a result of intermolecular interactions, which can lead to co-operative behaviour. The first is classified by abrupt spin transitions, which occur over a temperature range of less then 10K. In general, it requires crystal packing that facilitates strong communication between neighbouring metal centers. In contrast, gradual spin transitions occur over a much larger temperature range, with some systems having transitions that occur over 200K. Gradual spin transition are a result of weak communication between the metal centers in a crystal lattice(shown in figure 1.7 left).

A third variation in spin crossover occurs when the transition upon cooling is different from the transition upon warming. This results in a magnetic hysteresis, and molecular bistability, which refers to a molecule (or assembly of such) that

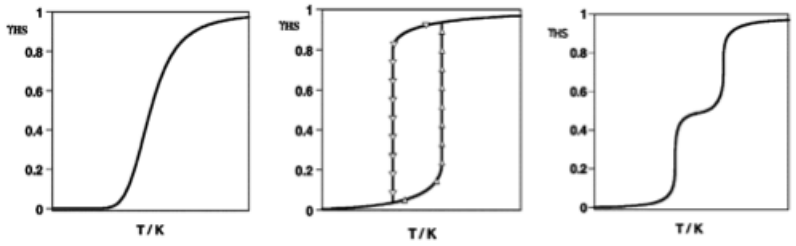

FIGURE 1.7: Variations of spin crossover: Left figure a gradual spin transition. Centre: an abrupt transition showing thermal hysteresis. Right: a multi-step spin transition. Reproduced from reference [23] with permission from the Royal Society of Chemistry

can exist in two different electronic states at the same temperature. The state which is present in the transition range is path dependent, and is an example of a molecular memory effect.

A fourth variation of spin crossover is a multistep transition (shown in figure 1.7 right). Multistep spin transitions can be interpreted in two ways. First it can be due to intrinsic differences between two spin crossover sites in a molecule or second, it can be due the presence of an intermediate phase. Multistep transitions are common in polynuclear spin crossover complexes, including systems based on metal organic frameworks[24], or polynuclear chains[25]. Finally a fifth type is one where the spin transition is incomplete[26]. Incomplete transitions are a result of equilibrium not driving the reaction completely to one spin state or the other at any temperature, and results in values for $\chi_m T$ that are different from the expected high spin or low spin values across the temperature range.

1.4.1.2 Perturbation by Light Irradiation (The LIESST Effect)

The light-induced excited spin state trapping (LIESST) effect is the excitation of a spin crossover compound from the low spin to the high spin configuration with the use of light below a critical temperature (know as the LIESST temperature). In LIESST complexes, a light source is used to irradiate the complex (generally into a strong absorption band), this excites the electrons to the excited spin state generally through a cascade pathway that includes intersystem crossing (see section 1.6.2) until it reaches a metastable state. The excited state is persistent as relaxation from the excited to the ground state is only possible through forbidden transitions (due to the spin selection rule). Shown in figure 1.8 is a typical $\chi_m TvsT$ plot for a spin crossover complex exhibiting the LIESST effect.

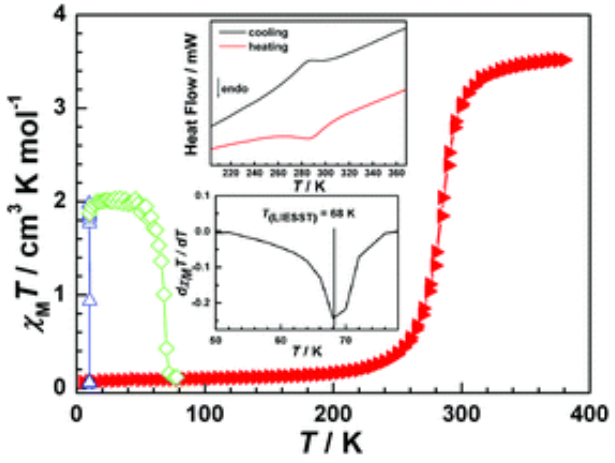

FIGURE 1.8: $\chi_m TvsT$ plot of a complex showing the LIESST effect: of an Fe(II) complex with ligand 2-hydroxy-3-methyl-N'-((pyridin-2-yl)-ethylidene)benzohydrazide. Reproduced from reference [27] with permission of the Royal Society of Chemistry

1.4.1.3 Pressure Perturbation

The application of pressure to a spin crossover compound changes the temperature at which half of the spin population is low spin, and half is high spin ($T_{\frac{1}{2}}$)[28]. This is due to compression of the crystal structure of the spin crossover molecule augmenting the intra-molecular interactions in the molecule and making the low spin state favourable at higher temperatures. At the limit of high pressure, the complex is trapped in the low spin state at all temperatures. Shown in figure 1.9 is the effect of applied pressure on the magnetism of the spin crossover complex $CrI_2(depe)_2$[28].

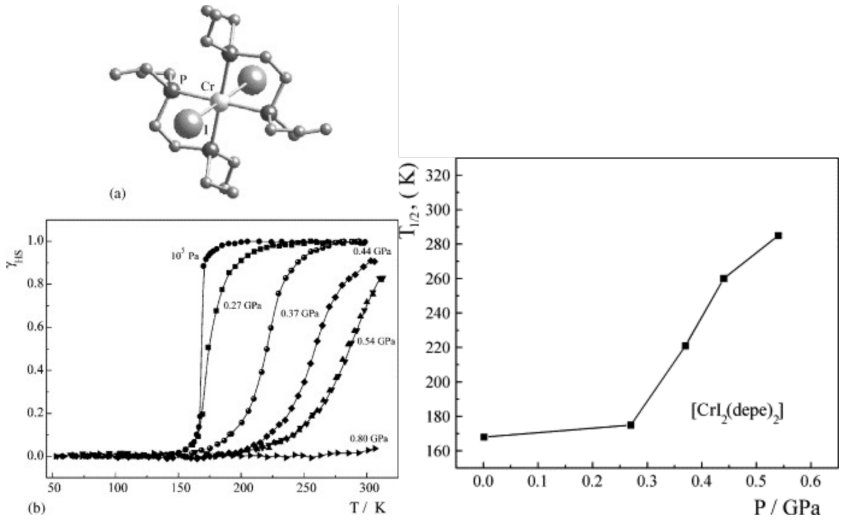

FIGURE 1.9: $\chi_m TvsT$ (left bottom) and $T_{\frac{1}{2}} vsP$ (right) plots and structure of the complex $CrI_2(depe)_2$ which shows the effect of pressure on a spin crossover compound. Adapted from reference [28] with permission

1.4.2 Valence Tautomerism

Tautomers are structural isomers that readily inter-convert with each other through a chemical process known as tautomerization. Formally it is thought of as a migration of a proton which is accompanied by the switch between a single bond and an adjacent double bond. This differs from the concept of resonance which is formally the movement of electrons. Tautomerism is an important concept as many protic ligands undergo keto-enol or amine-imine tautomerization. When tautomerization is possible, it exists in a state of chemical equilibrium, with a rapid interconversion of the tautomers occurring. Due to this rapid interconversion, the tautomers are generally considered to be two forms of the same molecule.

Valence tautomerism(VT)[29] is a specific type of tautomerism that does not involve the migration of atoms in the structure. Rather the tautomerization occurs through a rapid reorganization of bonding electrons, which results in a change of the molecular geometry of the molecule in question. In the case where the electron transfer is between a redox active ligand and a metal ion, a change in the overall spin of a molecule occurs, which can also be accompanied by a change in the spin state of the metal ion. The overall effect is a magnetic profile that appears similar to spin crossover.

The oldest family of VT materials is the cobalt-dioxolene complexes. VT in the Co-dioxolenes is accompanied by a spin transition in the cobalt ion (scheme 1.1)[29]. At low temperatures the cobalt ion has an oxidation state of +3 (low spin, $S = 0$)

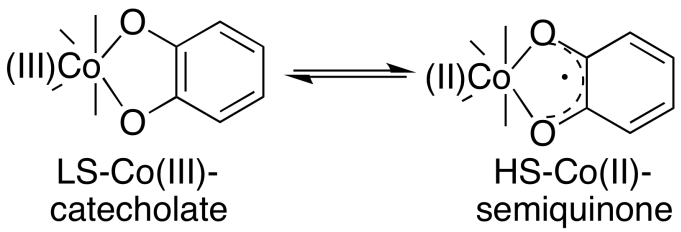

SCHEME 1.1: The redox series of the cobalt-dioxalene valence tautomers (mononuclear).

and the ligand is a diamagnetic catecholate. As high temperatures an electron is transferred from the catecholate (oxidizing to a semiquinone) to the cobalt ion (which is reduced to Co(II)). The Co(II) ion is high spin, and antiferromagnetically coupled to the unpaired electron of the semiquinone resulting in an overall spin of $S = 1$ for the molecule.

1.4.3 Single Molecule Magnetism

Single molecule magnets (SMMs) are a specific type of paramagnetic material that exhibit an energy barrier that allows a molecule to maintain its magnetic orientation after the removal of an external magnetic field, a property that looks superficially like ferromagnetism. SMMs offer the ultimate miniaturization of magnetic memory offering what is conventionally held by one magnetic domain (a bit) to be held by a single molecule.

The energy barrier which characterizes SMM behaviour has two requirements: a large magnetic anisotropy, and a high ground spin state. This energy barrier separates the two degenerate ground states and traps the molecule in one of the

two sub levels of the magnetic ground state which slowly relaxes over time at low temperatures.

$Mn_{12}O_{12}(MeCO_2)_{16}(H_2O)_4 \cdot 2MeCO_2H] \cdot 4H_2O$ was first synthesized in 1980[30]. It was the first SMM to be discovered, when further magnetic studies were performed in the 90's[31][32]. Its structure consists of an internal cubane unit $Mn(IV)_4O_4$ connected to a ring of 8 Mn(III) metal centres by bridging oxo ligands which causes the two rings to be antiferromagnetically coupled to each other. Abbreviated Mn12 this molecule is the most common representative of SMMs which are formed by clusters of metal centres. The magnetic anisotropy of this class of SMMs is difficult to predict, as in general, the magnetic anisotropy comes from the alignment of Jahn-Teller axis in the molecule, and requires a certain amount of serendipity when it comes to synthesizing new SMMs.

The next development[5] in the field of single molecule magnetism was the use of lanthanide ions as a basis for creating a high spin ground state. Lanthanides offer high spin ground states due to the presence of seven near degenerate molecular orbitals as a result of the limited splitting of the shielded d-orbitals in a ligand field. Lanthanides (with the exception of Gd) also have a high intrinsic magnetic anisotropy which meets the second requirement for the presence of SMM behaviour.

The lanthanide method of generating SMMs has its drawbacks as well. Magnetic coupling between lanthanide metal centres in a molecule with multiple lanthanide

ions is weak, due to the placement of unpaired electrons in the shielded f-orbitals. However, this can be overcome by using paramagnetic ligands[33], as the interaction between the electrons in the f-orbitals of the lanthanide ion, and the unpaired electron in the SOMO of ligand is strong enough for coupling to occur, which has effectively produced some of the SMMs with the highest anisotropic barriers to spin relaxation[34].

1.5 Magnetometry

Magnetometry can be broadly defined as the measurement of a magnetic field in both direction and magnitude. The field was pioneered by the physicist Fredrich Gauss with the first magnetometer's invention. For a materials chemist's purpose there are two types of magnetometers. The first and less sensitive method is the vibrating sample magnetometer (VSM) and the second is the superconducting quantum interference device (SQUID).

A VSM detects the magnetization of a sample by vibrating the sample inside an inductive pickup coil that is placed inside a larger superconducting interference device coil. An external field is applied which will partially align the paramagnetic centres of a molecule. The movement of the sample creates magnetic flux which generates a proportional potential in the nearby pickup coil. The induced voltage can then be measured, which with a known sample, and mass can be converted to the molar susceptibility of the sample.

SQUID magnetometers are much more sensitive than VSMs. They are based on a device known as a Josephson junction which if formed from two superconductors that are separated by a thin insulating layer. The sensitivity of SQUIDs come from the ability to measure the magnetic field associated with a single flux quanta; which is equal to $\Phi_o = \frac{2\pi\hbar}{2e} \approx 2.0678x10^{-15}Tm^2$. A constant biasing current is maintained allowing for the measured voltage to oscillate with the changes in phase at the Josephson junction, which is dependent on the magnetic flux. Knowing the number of oscillations that have occurred allows for the determination of the flux change, and therefore allows for the very precise determination of the induced magnetism in the sample.

1.6 Luminescence

When light is emitted from a substance it can be characterized by the source of the energy which fuels the emission. In the broadest sense there are two categories; incandescence and luminescence. Incandescence is the emission of light due to the heating of a substance, and as such is just the specific type of thermal radiation which pertains to the visible spectrum. In contrast, luminescence is the emission of light due to some process other than heat. These processes include but are not limited to chemical reactions, electrical energy, subatomic motion, absorption of light, and the application of stress on a crystal.

The process which supplies the energy for emission further characterizes the light from a luminescent source. For example, if light is emitted due to a chemical reaction the process is termed chemiluminescence(for example in glow sticks); if due to the application of an electric current then it is termed electroluminescence (such as in LED's); and if due to the absorption of photons, photoluminescence(as seen in black-light posters). Photoluminesence can further be sorted into two categories: fluorescence and phosphorescence.

1.6.1 Spin states in excited molecules

When an electron in a diamagnetic molecule is excited via absorption of radiation to a higher energy level, there are two possible luminescent scenarios. First, if the electron is aligned antiparallel with it's previously paired electron that remains in the ground state, the overall spin is 0 in the molecule (or in the singlet state with the spin multiplicity $2S + 1 = 2(0) + 1 = 1$). In contrast, if the excited electron is aligned parallel with the ground state electron, the overall spin of the molecule is 1 (or in the triplet state with spin multiplicity $2S + 1 = 2(1) + 1 = 3$).

The excitation to a singlet state is far more likely then the excitation to a triplet state. This is due to the preservation of the spin multiplicity during the excitation. If a change in spin state occurs during excitation, there is a change in spin multiplicity for a molecule (generally from the singlet to the triplet state). This is a forbidden transition by the spin selection rule which states that the promotion

of electrons occurs without a change in spin state. As such the promotion to a triplet state is rare. However, the triplet state is persistent as the relation pathway is also spin-forbidden.

1.6.2 Deactivation Processes and Jablonski Diagrams

A molecule that is excited to a higher energy state will eventually return back to the ground state through any number of radiative, or non-radiative processes. The route of deactivation with the highest probabilistic outcome is the one that is most rapid, with the least amount of time spent in the excited state.

Non-radiative deactivation processes include vibrational relaxation, internal conversion, external conversion, and intersystem crossing. During the excitation process several vibrational levels of the excited electronic level can be reached. The relaxation from these levels via processes of both intra- and intermolecular variety is extremely quick, with lifetimes shorter than that of the excited electronic states. This means that all other processes always originate from the lowest vibrational level of an excited state.

Internal conversion is an intermolecular process of a molecule which allows for the transition from a higher electronic state to a lower electronic state as long as the two states have the same spin multiplicity. It is most likely in systems where the two electronic levels are close enough in energy to allow for overlap of the mechanical energy levels.

External conversion is the deactivation of an excited energy state that involves the interaction between the excited state and the solvent or solute which is most common in solutions which are at high temperatures, or have a high viscosity. Under these conditions there is an increase in the number of collisions between molecules.

Intersystem crossing involves the transition to an electronic state of different spin multiplicity (i.e. either singlet to triplet or vice versa). Intersystem crossing is more probable in systems where the vibrational energy levels of the electronic energy levels in question overlap. It is most commonly seen in molecules that possess heavy ions, such as iodine, which increases the spin-orbit coupling in a molecule which makes it more likely for vibrational levels to overlap.

Radiative deactivation process include fluorescence and phosphorescence. Fluorescence occurs only as a transition between spin states of the same spin multiplicity. It is a quick process with the absorption to the excited spin state in the order of $t = 10^{-15}s$, and emission occurs on the order of $t = 10^{-9}s$. In general, there is a shift in the wavelengths of the absorbed and emitted light (generally to higher wavelength), a phenomena known as the Stokes shift. In contrast, phosphorescence is a transition between electronic states of different spin multiplicities and is usually a result of intersystem crossing. This process is much slower as only forbidden transitions are available to return the excited electron to the ground state.

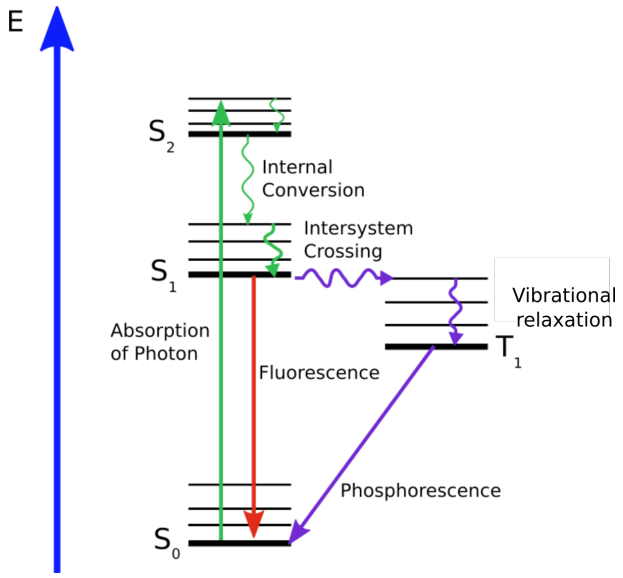

FIGURE 1.10: Jablonski Diagram showing fluorescence and phosphorescence pathways: Common pathway is in green, while fluorescence pathway is in red and phosphorescence is in purple.

A Jablonski diagram (figure 1.10) is a representation of the electronic states of a molecule and the transitions that occur between them. The energy levels of the molecule are arranged vertically by energy, and horizontally by spin multiplicity. vibrational ground state of each energy level are denoted by bold lines, while thin lines indicate the excited vibrational states. Transitions between the energy levels are indicated by arrows, with straight arrows for absorption and radiative transitions, and squiggly arrows used for non-radiative transitions.

1.7 Redox Active Ligands(RALs)

A reduction-oxidation (redox) reaction, is aptly named to describe the complimentary process of reduction (gaining of an electron, or decrease in oxidation state)

and oxidation (loss of an electron or increase in oxidation state), that occurs in any reaction which sees the oxidation state of the involved atoms change. To expand upon the idea, a redox active ligand(RAL), is a ligand which can undergo a redox reaction. As such it offers the possibility of a transfer of electrons to or from bound metal ions; a property that is of interest in many different fields of chemistry, including catalysis[35], bioinorganic[36], and materials[33][29] chemistry.

Coordination complexes with redox active ligands are used as catalysts in many reactions including cyclopropanation, CH-aminations, aziridizations, coupling reactions and water oxidation[35]. RALs can also act as electron sinks in which the ligand is in its free form in solution, binding only to bring about redox changes to the active catalyst. An example is the incorporation of quinones into the industrial Wacker process, speeding up the reaction (scheme 1.2).

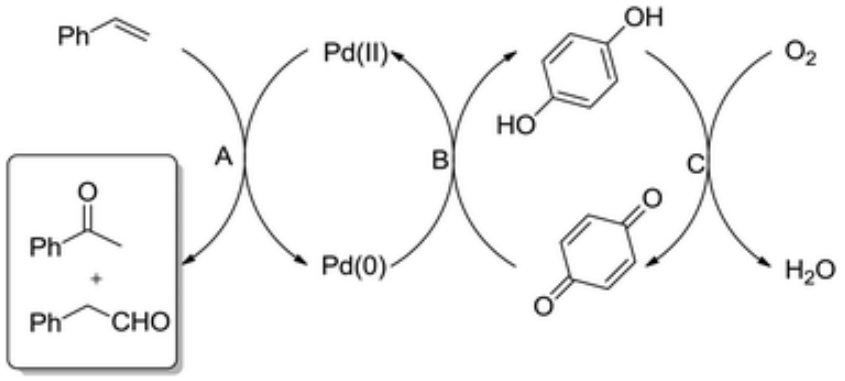

SCHEME 1.2: Quinone mediated Pd catalysis in Wacker-type chemistry. Reproduced from Ref. [35] with permission from The Royal Society of Chemistry

There are several redox active ligands in biological roles. One of the more prominent examples is galactose oxidase which oxidises alcohols into aldehydes using O_2 and releasing H_2O_2. The active site of galactose oxidase consists of a Cu(II)

ion coordinated to tyrosil. The catalytic cycle is shown in scheme 1.3. Mimicking biological systems is one focus of the field of bioinorganic chemistry[37].

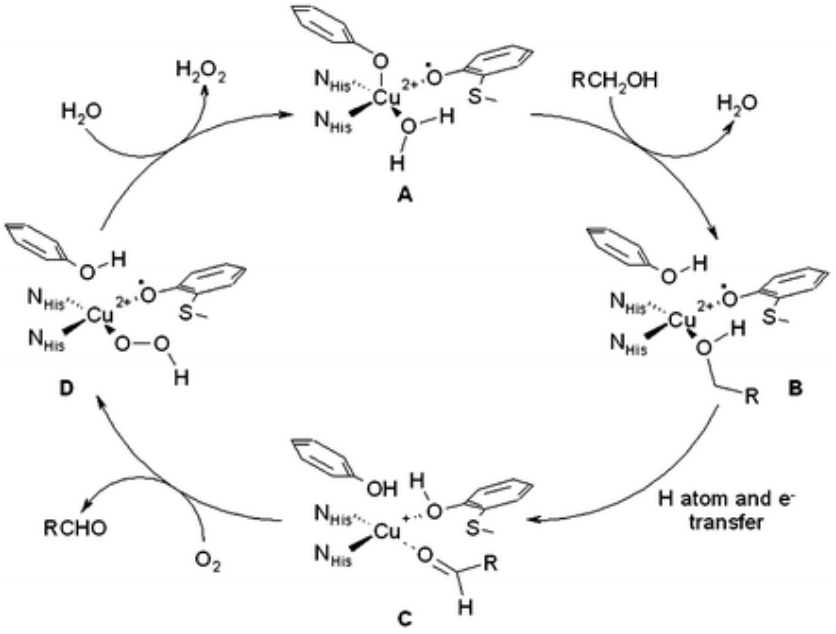

SCHEME 1.3: Catalytic cycle of galactose oxidase. Reproduced from Ref. [37] with permission from The Royal Society of Chemistry

1.7.1 Paramagnetic Ligands

If a RAL forms a stable molecule upon a single electron oxidation or reduction, then a stable paramagnetic ligand is formed (though not all paramagnetic ligands are redox active). In general, the magnetic properties and electronic properties are influenced greatly due to this new paramagnetic centre, which can couple to the coordinated metal ion through either direct exchange or super exchange mechanisms.

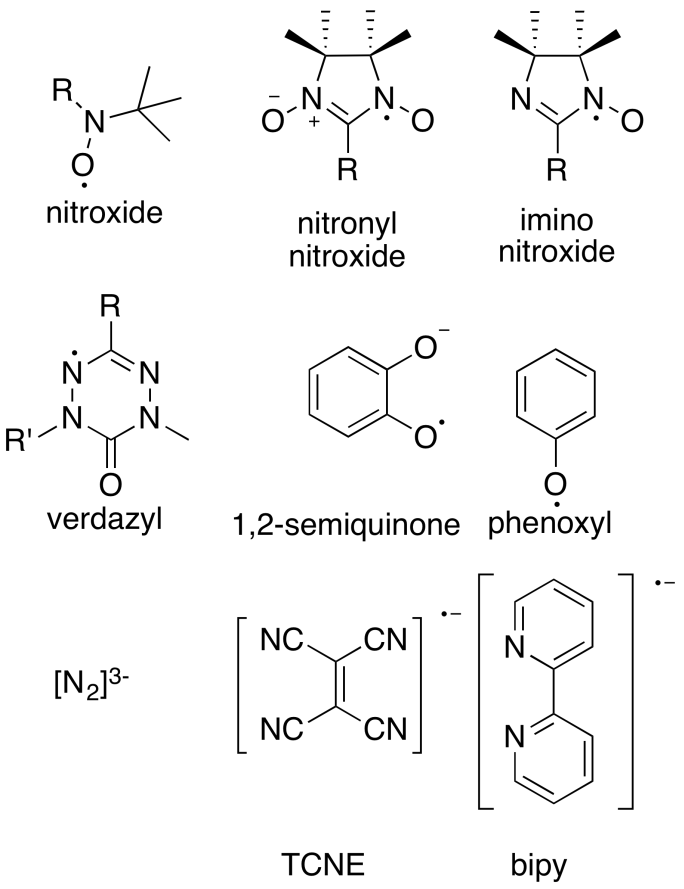

FIGURE 1.11: A selection of paramagnetic ligands

There are many types of organic molecules which are used as paramagnetic ligands (figure 1.11). Nitroxides, imino nitroxides and the bridging nitronyl nitroxides were some of the first stable organic radicals utilized in the field of coordination chemistry[38]. They offered the first step towards stronger magnetic coupling in complexes, but required particularly Lewis acidic metal centres (such as metal ions with hfac or halogens as ancillary ligands) to coordinate. Of particular interest for this class of RALs is the Cu(II) chain complexes known as breathing crystals[39], which undergo a spin crossover like transition that arises from intermolecular interactions, rather then a change in spin state of the metal ion.

Verdazyl radicals were first synthesized in 1963[40], however, the first metal complex with diamagentic metal centres was not reported until 1997[41]. The first complex with a verdazyl radical and a paramagnetic ion was published in 2000[42]. Verdazyl radicals with paramagnetic metal centres offer very strong ferromagnetic coupling between the metal centre and the verdazyl radical in nickel complexes, while antiferromagnetic exchange occurs in manganese complexes. Recently verdazyl radicals have been used in SMM complexes to promote stronger coupling between lanthanide metal centres, increasing the anisotropic barrier to relaxation in SMMs.[5]

Another important family of RALs in coordination chemistry is dioxolenes. In VT complexes (figure: 1.1) dioxolenes form a redox pair with cobalt. At low temperatures the dioxolene is a catecholate, but increasing temperature the dioxolene accepts an electron from Co(II) forming a semiquinone radical. Bipyridines are commonly used as capping ligands (which can be reduced to add a paramagnetic centre), while bipyrimidine can be used as bridging ligands in the formation of polytopic complexes. Another class of RALs, phenoxyl radicals are of biological importance[43][44], but have also found use in materials chemistry[45]. In general they form complexes with interesting photo-physical properties[45][46].

Some specific RALs are placed in figure 1.11 as well. The ligand $[N_2]^{3-}$ which is used to synthesize dinuclear complexes[34] was found to promote unprecedented coupling between lanthanide metal centres. The Tb complex exhibited SMM behaviour at record temperatures, due to the high ground spin state afforded by

strong antiferromagnetic coupling between the lanthanide ions and the ligand. Another ligand TCNE forms a complex with vanadium which exhibits ferrimagnetism at room temperatures, one of the few molecular magnets to do so[12].

1.8 Azo-aromatic ligands

Azo-aromatic (or arylazo) ligands are a specific class of RAL and is the topic of an extensive review by Goswami[47]. The redox active component of this class of ligands is the azo moiety. The oxidation series of an azo bond is shown in scheme 1.4. The azo bond can be sequentially reduced to the radical anion, next to a dianion single bond, and finally the bond will be cleaved. For arylazo RALs the LUMO is mainly located on the azo nitrogens. The LUMO which is low lying energetically has been successfully reduced in a variety of complexes in a variety of ways which include $M(0)$ complexes[48].

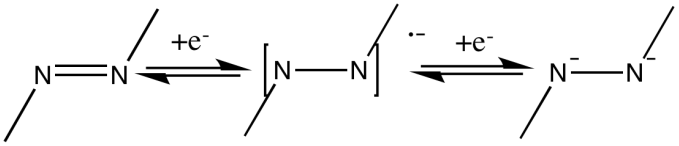

Scheme 1.4: The redox series of an azo bond.

The unreduced azo bond is an interesting functional group. Commonly found as the chromophore for coordination complexes, the azo moiety facilitates strong absorptions in the visible range. Many arylazo complexes are effective $\pi-$acceptors and have strong metal to ligand back bonding with electron rich metals, such as

iron(II), and copper(I). The metal back bonding manifests itself in shorter vibration frequencies of the N-N bond, charge-transfer spectra (which may result in valence tautomerism), proton dissociation, and bond lengths. An example system is that of the ligand 1-(2-pyridylazo)-2-naphtholate (PAN)[49]. PAN acts as a tridentate ligand with donation through N_{py}, N_{azo}, and $O^{-}_{napthol}$ atoms(figure 1.12). The complex $Ru(PAN)_2$ has intense absorptions in the visible spectrum: λ_{max} (ϵ, ($M^{-1}cm^{-1}x10^4$) 606(11240), 566(9370), 548(9240), 470(9710), 408(8040), 368(10390), 302(13020), which are of ILCT, MLCT and LMCT character. This is the spectrum typical for divalent complexes with azo-aromatic ligands.

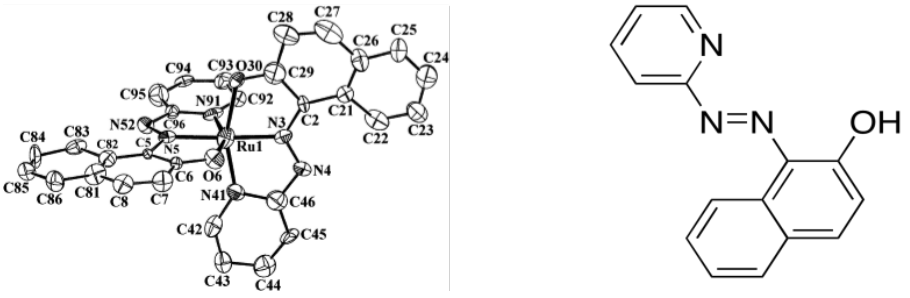

FIGURE 1.12: Left: Structure of $Ru(PAN)_2$: Select bond lengths $\mathring{A}$: Ru(1)–N(3), 1.973(10); Ru(1)–O(6), 2.053(9); Ru(1)–N(5), 1.965(10); Ru(1)–O(30), 2.105(8); Ru(1)–N(41), 1.985(11); N(3)–N(4), 1.427(13); Ru(1)–N(91), 2.068(10); N(5)–N(52), 1.349(11). Right: Chemical structure of PAN. Adapted from [49] with permission from Elsevier

Reduced complexes with arylazo ligands are present in literature, but there are very few magnetic studies performed, with the emphasis being on the photophysical properties and redox behaviour of these complexes.[50]. The few magnetic studies available[51] do show intense coupling between paramagnetic centres, making azo-aromatic ligands an interest for magneto-chemistry purposes as

well. For example, the ligand (4-chloro-2-phenylazo)pyridine (figure 1.13) undergoes a two electron reduction upon coordination with $Re_2(CO)_8$. The resulting complex posses a magnetic profile which features strong intramolecular coupling ($J = -220cm^{-1}$) between the low spin Re(II) metal centre, and the azo centered radicals without intermolecular interactions in the range of 150-300K, but strong intermolecular coupling between 2-150K ($J = -170cm^{-1}$, $\theta = -65K$).

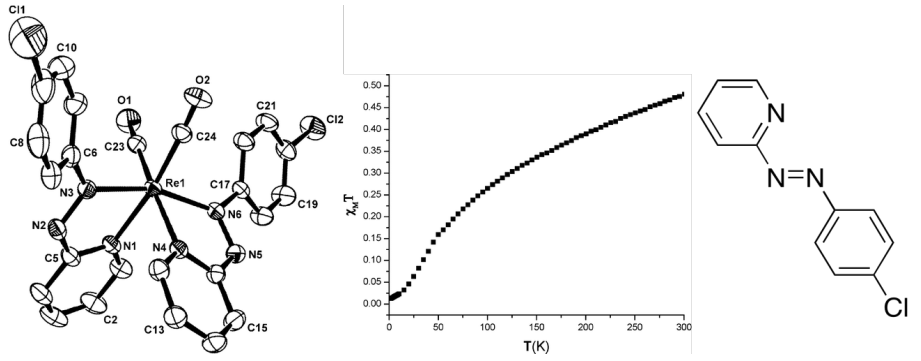

FIGURE 1.13: Overview of $Re((4-chloro-2-phenylazo)pyridine)_2(CO)_2$:Left crystal structure, Center: Magnetic Profile, Right: structure of (4-chloro-2-phenylazo)pyridine. Adapted with permission from [51]. Copyright (2010) American Chemical Society.

Another interesting arylazo system that was published by Coronodo et al.[52] is $[((SiMe_2NPh)_3 - tacn)U(\eta^2 - N_2Ph_2)]$ (figure 1.14) which exhibits a SMM behaviour; the first molecule with a U(IV) ion to do so. U(IV) is a non-Kramers ion that exhibits an orbital singlet at low temperatures, which means that it lacks the bistable ground state required for slow magnetic relaxation. However the addition of an extra unpaired electron via a radical ligand causes a switch in U(IV) from a non-Kramers ion to a Kramers ion, allowing for SMM behaviour in U(IV) complexes.

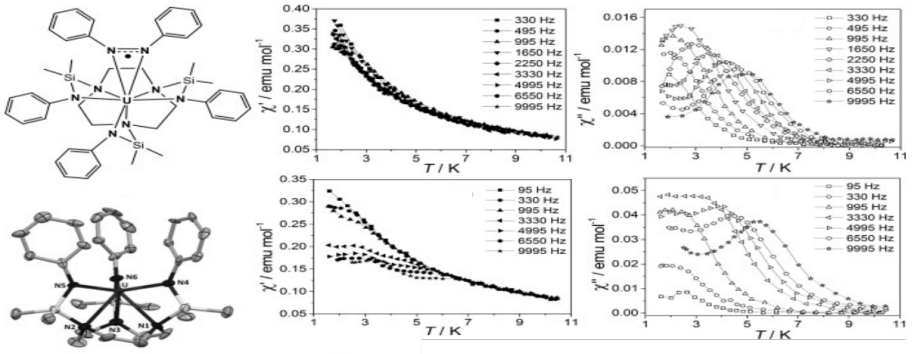

FIGURE 1.14: Left crystal structure and line drawing of $[((SiMe_2NPh)_3 - tacn)U(\eta^2 - N_2Ph_2^{\cdot})]$. Right: In-phase and out-of-phase components of the ac susceptibility at different frequencies from 1.7 to 10K at $H_{ac} = 5Oe$ and $H_{dc} = 1000Oe$ (in-phase), and $2500Oe$ (out-of-phase). Adapted with permission from reference [52].

1.9 Research Goals

1-(2-pyridylazo)-2-phenanthrol(PAPL) (figure 1.15) was first synthesized in the 1960's[53] and is a ligand with multiple useful properties. PAPL is a redox active ligand which has two possible pathways to become a paramagnetic ligand (scheme 1.5). The first is by reduction, adding an electron into the low lying LUMO which is centered on the nitrogen atoms of the azo bond. While the other is by the oxidation of the phenol group, producing a phenoxyl radical. PAPL is also a suitable model for other ligands as the precursor 9,10-phenanthrenequinone is easily substituted using simple electrophillic aromatic substitution reactions, which allows for tuning of the ligand field by the addition of electron withdrawing or electron donating groups.

Early studies of transition metal complexes of the ligand PAPL lack any structural data[54][55], generally relying solely on combustion analysis for the determination

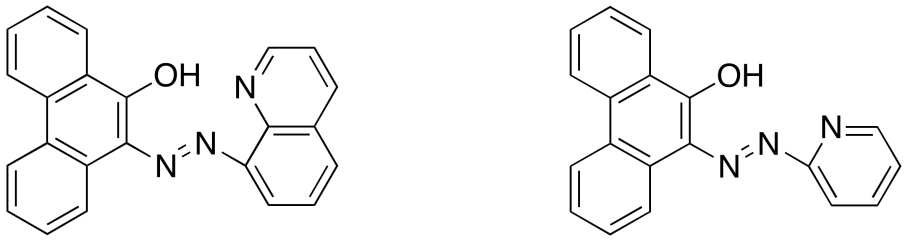

FIGURE 1.15: Left: QAPL and Right:PAPL. The ligands presented in this thesis

of the molecular formula of complexes. In the complexes of iron[56] and cobalt[57] magnetic studies were performed, using Mössbauer spectroscopy to determine the spin state in iron, finding both low spin Fe(II) and Fe(III), (which was confirmed with use of a Gouy balance). Variable temperature magnetic susceptibility studies on the cobalt complex (by Gouy balance) suggested a Co(II) spin crossover compound.

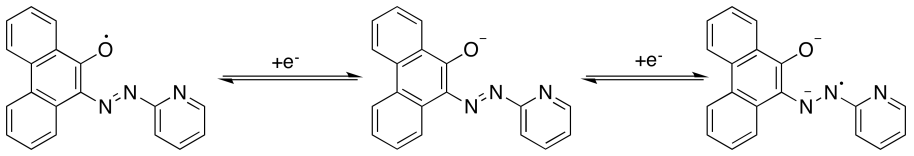

SCHEME 1.5: The redox series of PAPL.

The Lemaire research group noticing the lack of structural data performed an initial survey on the ligand with divalent complexes of zinc, manganese and nickel[58]. These complexes feature nearly identical FT-IR spectra, UV-Vis spectra and similar structural features. Of particular interest in this study is the spectroelectrochemical data on the Mn and Ni complexes which showed an effective reduction of the azo bond (figure 1.16). The second study [59] was of a Co(III) complex that was produced when attempting to replicate the spin crossover complex of

Bhoon[57]. The trivalent complex features a very different UV-Vis profile with much smaller ϵ values, and LMCT character in the UV-Vis spectrum which is not present in the previous $M(PAPL)_2$ complexes.

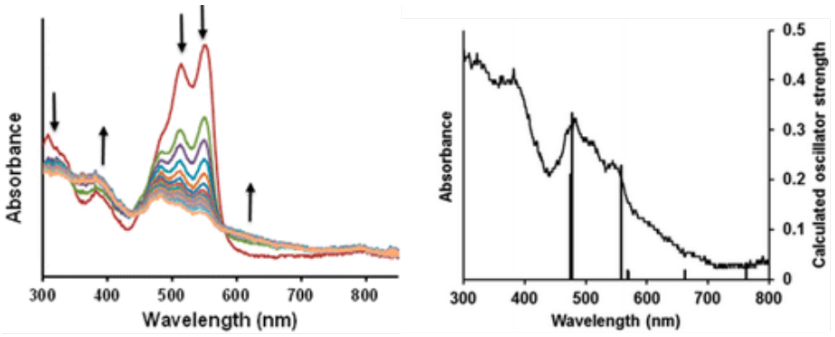

FIGURE 1.16: Left: Spectroelectrochemical spectra for $Zn(PAPL)_2$ at 1.5V. Right: Experimental (curve) and calculated (bars) electronic spectra of $Zn(PAPL)_2$. Adapted with permission from [58]. Copyright 2013 American Chemical Society

The objectives of this project are three-fold. The first goal is to complete the survey of 3d transition metal complexes with the ligand 1-(2-pyridylazo)-2-phenanthrol(PAPL) specifically focusing on the redox active metals Fe, Co, V, and Cu, as they may offer interesting electron transfer properties (such as VT or charge transfer). Also of interest is a Ru complex, as the intense absorptions of the PAPL ligand may have an antenna like effect for the emission from the ruthenium metal centre. It is also our hope to produce metal complexes with the reduced form of PAPL (by the addition of an electron into the low lying azo-centered π^* orbital) through the use of either reducing metals (such as metal carbonyls) or reducing agents (such as cobaltocene).

Lanthanide PAPL complexes are of an interest as well. There are very few studies in literature of azo-aromatic ligands coordinated with lanthanide ions[60][61]. Of particular interest is complexes of Dy and Gd, as they have been shown to be useful in generating SMM behaviour in complexes. Further it is expected that lanthanide complexes with the PAPL ligand which feature strong absorptions should offer interesting luminescent properties, as well as intense absorptions in the visible region.

The final area of interest is other azo-aromatic ligands. This chapter features the synthesis of 1-(8-quinolinazo)-2-phenanthrol(QAPL). Very similar to the ligand PAPL, it is expected to feature better $pi-$stacking in the crystal structure due to the extended π system afforded by replacing the pyridine ring with quinoline. It is also expected to have a slightly different binding motif, which we hope will result in interesting structural results for complexes of Fe and Co.

Chapter 2

Experimental

2.1 General procedures

All reagents and solvents were commercially available and used as received unless stated otherwise. Deaerated and anhydrous solvents were obtained from a Puresolve PA MD-4 solvent purification system, and all air or moisture sensitive reactions were carried out using standard Schlenk techniques. Elemental analysis were obtained from Canadian Microanalytical Services, LTD, Delta, BC, Canada and Guelph Chemical Laboratories, Guelph, ON, Canada.

2.2 Instrumentation

All instrumentation is located at the home institution (Brandon University for year 1, and Brock University for year 2) unless otherwise stated.

2.2.1 FT-IR

All spectra were recorded on a Shimadzu IRAffinity-1 spectrometer as KBr disks.

2.2.2 UV-Vis

Spectra were recorded on a Shimadzu 3600 UV-Vis-NIR spectrophotometer, or a Cary UV-Vis-NIR spectrophotometer 6000i from Agilent Technologies (located at the University of Montreal). All room temperature spectra were obtained from solutions in appropriate solvents in quartz cuvette cells.

Variable temperature UV-Vis experiments were carried out in appropriate solvent (either toluene or ethanol) using a Specac variable temperature cell and temperature controller.

2.2.3 NMR

$^{1}H/^{13}C$-NMR spectra were recorderd on a Bruker Avance III 400MHz.

2.2.4 Mass spectometry

ESI spectra were obtained using a Bruker HCT Plus Proteineer LCMS. EI spectra were obtained using a Kratos Concept 1S High Resolution E/B mass spectrometer. LC-MS experiments were recorded on an Agilent 1260 Infinity liquid chromatograph/6530 accurate mass Q-TOF in high-resolution mode with 70:30 HPLC grade acetonitrile/water using positive mode electrospray ionization.

2.2.5 Electrochemistry

Electrochemical experiments were performed with a Bioanalytical Systems Inc. Epsilon electrochemical workstation. Compounds and the supporting electrolyte (Tetra(n-butyl)ammonium hexafluorophosphate) were dissolved in anhydrous solvent (DCM, acetonitrile, or DMF) and dearrated by sparging with nitrogen gas for 20 minutes. The solution concentration were approximately $10^{-3}M$ in anylate and $0.1M$ in supporting electrolyte. A typical three-electrode set-up was used which includes a glassy carbon working electrode, a Ag/AgCl reference electrode, and a platinum wire auxiliary electrode.

2.2.6 Mössbauer Spectroscopy

Analysis was performed using a constant-acceleration spectrometer (Wissil GMBH, Germany) in a horizontal transition mode using a $50mCi^{57}Co$ source. For variable temperature experiments a Janis SHI-850-1 closed cycle helium refrigerator cryo-stat was used(Located at the University of Western Washington).

2.2.7 EPR

EPR spectra were recorded using a Bruker Elexsys E580 pulse spectrometer operating in CW mode (Located in the van der Est lab Brock University).

2.2.8 Luminescence

Luminescence spectra were obtained using a Perkin Elmer LS55 Luminescence Spectrometer (University of Montreal) equipped with a Low Temperature Accessory. The luminescent properties described here in are all performed on DCM solutions, and wavelengths have an accuracy of $\pm 1.0nm$.

2.2.9 Single crystal X-ray structure determination

Crystals of X-ray quality were mounted on a glass fiber and data was collected on a Bruker Kappa APEX-DUO diffractometer (University of Toronto) using

monochromated Mo Kα radiation. Data was processed using APEX II or SAINT. Absorption corrections were performed by SADABS, while structure refinement was carried out using SHELXTL.

2.2.10 pXRD

X-ray powder diffraction data was obtained using either a Siemens D5000 diffractometer (University of Winnipeg) and a Huber G670 diffractometer (University of Winnipeg).

2.2.11 Variable Temperature Magnetic Susceptibility Measurements

Variable temperature magnetic susceptibility measurements were carried out on multiple machines. 1)9T DynaCool Physical Property Measurement System (Quantum Design) using the vibrating sample magnetometer option (University of Winnipeg). All samples were individually pelleted, weighed, tightly packed into plastic capsules and loaded into brass holders. The signal from an empty capsule and the brass holder were measured prior to filling and were found to be at least three orders of magnitude lower than the signal from the samples. 2)A superconducting quantum interference device (SQUID) magnetometer (Quantum Design MPMS)

with a 5.5T magnet (temperature range 1.8–400K). Samples measured were carefully weighed into a gelatin capsule, loaded into a plastic straw and attached to the sample transport rod.

2.2.12 Computational Chemistry

Geometry optimizations and frequency calculations were carried out using the suite of programs included in the Turbomole 6.5 package[62][63] at the def2-SVP level[64][65] of theory using the BP86 functional[66][67][68] with the Resolution-of-the-Identity (RI) approximation [69][70][71][72][73] switched on. The calculated geometry was checked to ensure that it was a minimum on the potential energy surface (no negative frequencies). Single point energy and time-dependent density functional theory (TD-DFT) calculations were performed on the optimized geometries using the B3LYP[74][75] hybrid functional and the def2-TZVP[65] basis set on all atoms in chloroform for $Fe(PAPL)_2$ and $[Fe(PAPL)_2]$ using the PCM solvation feature in the Gaussian09 (Revision D.01)[76] package. The first 40 excited states were calculated in the TD-DFT[77] calculations. Tight SCF convergence criteria were used for all calculations. The program Chemissian[78] was used for the preparation of molecular orbital and spin density distribution figures and to carry out the Mulliken population analysis. The program QMForge[79] was used for analyses of the TD-DFT calculations. All computation was performed by Dr. Martin Lemaire.

2.3 Synthesis

2.3.1 Synthesis for Chapter 3

1-(2-pyridylazo)-2-phenanthrol(3.1) was synthesized using a previously reported procedure. 9,10-phenanthrequinone (0.281g, 1.35mmol) and 10mL glacial acetic acid were combined and heated to 70^oC creating an orange solution to which a slurry of 2-hydrazinopyridine (0.512g, 4.75mmol) in 3mL glacial acetic acid was added. The solution was heated to approximately 100^oC and allowed to react for 3 hours producing a red solution. The reaction mixture was then poured on ice, and the acid neutralized with potassium carbonate producing an orange precipitate which was collected by vacuum filtration and found suitable for coordination(0.316g, 79%). HR-MS (EI): Calculated for (found) $C_{19}H_{13}ON_3$ 299.1053 (299.1058). UV-Vis (CH_2Cl_2): λ_{max} (ϵ, $M^{-1}cm^{-1}x10^4$): 470nm (2).

$Co(PAPL)_2 \cdot CH_2Cl_2$(3.2) Compound 3.1(0.058g, 0.19mmol) was dissolved in anhydrous acetonitrile(15 mL) under N_2 in a dry Schlenk flask cooled in ice water. Five drops of triethylamine was added and the mixture stirred for several minutes followed by the addition of $Co_2(CO)_8$(0.022 g, 0.064 mmol). The ice bath was removed and the solution was stirred for five hours at room temperature. The reaction mixture was filtered and the precipitate washed with DCM(10mL) redissolving any precipitated product into the reaction liquor. Anhydrous diethyl

ether(10mL) was layered on the solution producing a purple microcrystalline powder over three days that was isolated by vacuum filtration and washed with diethyl ether. Yield (0.043g, 68%). The remaining reaction liquor was allowed to slowly evaporate producing single crystals that were structurally the same as the previous precipitated microcrystalline powder. FT-IR (KBr, cm^{-1}): 3059(w), 1601(w), 1580(w), 1557(w), 1441(w), 1373(m), 1343(m),1323(m), 1256(s), 1248(s), 1231(s), 1182(m), 1101(w), 1046(w),1005(w), 928(w) 754(m), 721(w), 660(w). Analysis calculated for (found, %) $CoC_{38}H_{24}N_6O_2 \cdot CH_2Cl2$: C, 63.26 (63.00); H, 3.54 (3.63); N, 11.35 (11.17), UV-Vis (CH_2Cl_2): λ_{max} (ϵ, $M^{-1}cm^{-1}x10^4$) 532nm (3), 682nm (0.5).

Fe(PAPL)$_2 \cdot$ CH$_2$Cl$_2$(3.3): Compound 3.1 (0.0500g, 0.167mmol) was dissolved in dry DCM (25mL) under a N_2 atmosphere in a dry Schlenk flask that was placed in a ice bath to which 5 drops of triethylamine and $Fe(CO)_5$ (0.0218g, 0.111mmol) was added. The ice bath was removed and the reaction was allowed to proceed for eight hours. Diethyl ether (20mL) was layered on the reaction mixture, and crystals suitable for X-ray diffraction grew out of solution concomitant with the precipitation of an intractable brown solid. Yield (0.0323, 59.1%). FT-IR (KBr, cm^{-1}): 3065(w), 1599(m), 1576(w), 1491(m), 1458(m), 1441(m), 1393(m), 1341(m), 1317(s), 1223(s), 1175(m), 1163(s), 1144(s) 1103(w), 1018(w), 903(m), 866(w), 754(m), 723(m), 685(w), 608(w), 478(w). Analysis calculated for (found, %) $C_{38}H_{24}FeN_6O_2 \cdot CH_2Cl_2$: C, 62.52 (66.47); H, 3.55 (3.52); N, 11.4 (11.95).

Fe(PAPL)$_2 \cdot$ 0.6THF(3.4) Compound 3.1 (0.0905g, 0.303mmol) was dissolved

in chloroform (5mL) and 5 drops of triethylamine were added. $Fe(NO_3)_3 \cdot 9H_2O$ was dissolved in methanol (5mL) and then added drop wise to the solution which was allowed to stir for one hour. A black precipitate was produced, collected by vacuum filtration, washed with water and methanol, and then dried. Yield (0.0669g, 69.3%). Crystals suitable for X-ray diffraction were grown by diffusion of *n*-pentane into a THF solution of 3.4. FT-IR (KBr, $cm^{-}1$): 3062(w), 1600(m), 1576(w), 1557(w), 1491(m), 1462(m), 1441(m), 1395(m), 1341(m), 1319(s), 1258(s), 1225(s), 1177(m), 1163(m), 1144(m), 1105(w), 1078(w), 1003(w), 926(m), 905(m), 756(m), 685(w), 664(w), 532(w), 475(w), Analysis calculated for (found, %) $C_{38}H_{24}FeN_6O_2 \cdot 0.6THF$: C, 69.74 (69.63); H, 4.17 (4.11); N, 12.08 (12.16). HR-MS (ESI+): Calculated for (found) $C_{38}H_{24}FeN_6O_2$: m/z 652.1310 (652.1333). UV-Vis ($CHCl_3$): λ_{max} (ϵ, $M^{-1}cm^{-1}x10^4$): 507nm (3), 770nm (1).

Ru(PAPL)$_2 \cdot$ 2.68CH$_3$OH(3.5) Compound 3.1 (0.101g, 0.337mmol) was dissolved in methanol(20mL). Five drops of triethylamine and $RuCl_3 \cdot xH_2O$ (0.0333g, 0.160mmol) were added to the solution which was refluxed for 12 hours. The solution produced a brownish-black precipitate that was collected by vacuum filtration, washed with water and methanol, and then dried. Yield (0.0854g, 76%). Crystals suitable for X-ray diffraction were grown by diffusion of *n*-pentane into a THF solution of 3.5. FT-IR (KBr, cm^{-1}): 3067(w), 2965(w), 1618(m), 1597(m), 1570(m), 1499(s), 1437(s), 1397(m), 1279(m), 1204(s), 1101(w), 1061(w), 1024(m), 512(w), 785(m), 752(m), 669(w). Analysis calculated for (found, %) $C_{38}H_{24}RuN_6O_2 \cdot 2.68CH_3OH$: 61.17 C, (60.95); H, 4.95 (3.93); N, 10.22 (9.26) .

UV-Vis ($CHCl_3$): λ_{max} (ϵ, $M^{-1}cm^{-1}x10^4$): 408nm (2), 470nm (2), 543nm (0.8), 614nm (0.6).

Cu(PAPL)$_2 \cdot$ 0.3CH$_2$Cl$_2$(3.6) Compound 3.1 (0.103g, 0.343mmol) was dissolved in dry DCM(30mL) under N_2 in a dry Schlenk flask that was cooled in a ice bath. Several drops of triethylamine and $[Cu(CH_3CN]PF_6$ (0.0670g, 0.180mmol) was added, and the reaction was then stirred for three hours at room temperature. The reaction mixture was then diluted with 15mL of DCM, and 25ml of diethyl ether was layered on the solution. Green crystals suitable for X-ray diffraction grew directly out of solution over two days. The crystals were collected by vacuum filtration, washed with methanol, and then dried. Yield (0.0620g, 51%). FT-IR (KBr, cm^{-1}): 3063(w), 1599(w), 1521(w), 1462(w), 1437(w), 1371(m), 1344(m), 1323(m), 1273(m), 1249(s), 1223(s), 1141.86(m), 1028(w), 1001(w), 928(m), 756(m) 669(m), 658(w), 421(w). Analysis calculated for (found, %) $CuC_{38}H_{24}N_60O_2 \cdot 0.3CH_2Cl_2$: C, 67.09 (67.23); H,3.62 (3.62); N, 12.26 (12.30). UV-Vis (DCM): λ_{max}= (ϵ, $M^{-1}cm^{-1}x10^{-4}$): 311nm (3), 517nm (4), 546nm (5).

Fe(PAPL)$_2$I$_3 \cdot$ 1.55CH$_2$Cl$_2$(3.7) $Fe(PAPL)_2$ (54.3mg, 0.0815mmol) of 3.4 was dissolved in DCM (25mL) and I_2 (100mg, 0.395mmol) was added. The solution was stirred for 12 hours resulting in a black microcrystalline precipitate that was collected by vacuum filtration, and washed with *n*-pentane, hexanes, water, and DCM. Yield (60.03mg, 70%). FT-IR (KBr, cm^{-1}): 1493(s), 1449(s), 1398(s), 1350(vs), 1280(s), 1215(vs), 1148(s),1016(m), 928(m), 756(s), 721(m). Analysis calculated for (found%) $C_{38}H_{24}N_6O_2FeI_3 \cdot 1.55CH_2Cl_2$: C, 40.78 (40.22); H, 2.34

(1.76); N, 7.21 (6.93). MS (ESI+ and -): m/z 652.1 (100%) $[M - I_3]^+$, 380.5 (100%) $[I_3]^-$. UV-Vis ($(CH_3)_2NC(O)H$): λ_{max} (ϵ, $M^{-1}cm^{-1}x10^4$): 365 nm (4), 505nm (3), 768nm (1).

$[\mathbf{(PAPL)VO}]_\mathbf{2}\mu - \mathbf{O_2}(\mathbf{3.8})$ 3.1 (0.0690g, 0.231mmol) was dissolved in chloroform (5mL) and 5 drops of triethylamine were added. VCl_3 was dissolved in methanol (5mL) which was then added drop wise and the solution was stirred for 15 hours. A green precipitate was produced, collected by vacuum filtration, washed with water, methanol, and diethyl ether and then dried. Yield (59.3mg, 93%). Single crystals suitable for X-ray diffraction were grown by diffusion of diethyl ether into a chloroform solution of 3.8. FT-IR (KBr, cm^{-1}): 1604(s), 1560(m), 1588(m), 1497(s), 1468(s), 1445(m), 1362(vs), 1329(s), 1285(s), 1273(m), 1246(s), 1227(vs), 1192(s), 1166(m), 1145(s), 1101(m), 1085(w), 1024(w), 930(s), 850(s), 758(s), 725(m), 659(m). Analysis calculated (found, %) for $C_{38}H_{24}N_6O_6V_2$: C, 59.86 (63.86); H, 3.17 (3.71); N, 11.02 (12.09).UV-Vis (DMF): λ_{max} (ϵ, $M^{-1}cm^{-1}x10^4$): 356nm (1), 776nm (0.7), 572nm (3), 613nm (3).

2.3.2 Synthesis for Chapter 4

$\mathbf{Gd(PAPL)_3}(\mathbf{4.1})$ Compound 3.1 (0.1169g, 0.3908mmol) was dissolved in chloroform (5mL) and 5 drops of triethylamine were added. $Gd(NO_3)_3 \cdot 6H_20$ was dissolved in methanol(5mL) and was added dropwise to the ligand solution which

was then stirred for 2 hours. A purple precipitate was produced, collected by vacuum filtration, washed with water and methanol and then dried. Yield (0.0884g, 62.2%). FT-IR (KBr, cm^{-1}): 3063(w), 1597(m), 1584(m), 1559(m) 1510(s) 1493(s), 1437(m), 1389(w), 1319(s), 1291(m), 1275(s), 1225(s), 1208(m), 1177(m), 1161(m), 1140(s), 1101(m), 1034(m), 999(m), 928(w), 754(m), 725(m), 637(w), 517(w). Analysis calculated for (found, %) $C_{57}H_{36}N_9O_3Gd$: C, 65.06 (65.34); H, 3.45 (3.39); N, 11.98 (11.87), MS (ESI+): 1053.2 (MH^+). UV-Vis (CH_2Cl_2): λ_{max} (ϵ, ($M^{-1}cm^{-1}x10^4$): 380nm (2), 525nm (6) 560nm (6).

Tb(PAPL)$_3 \cdot$ 0.4CHCl$_3$(4.2) Compound 3.1(0.0995g, 0.333mmol) was dissolved in chloroform (5mL) and 5 drops of triethylamine were added. $Tb(NO3)_3 \cdot 5H_2O$ was dissolved in methanol (5mL) and added dropwise to the stirred solution which was allowed to stir for a further 2 hours. A purple precipitate was produced, collected by vacuum filtration, washed with water and methanol, and then dried. Yield (0.0741g, 61.6%). FT-IR (KBr, cm^{-1}): 3065(w), 1597(m), 1584(m), 1559(m), 1510(m), 1491(m), 1437(m), 1387(w), 1341(m), 1319(s), 1292(m), 1277(s), 1227(s), 1207(m), 1179(m), 1161(m), 1140(s), 1101(m), 1034(w), 999(m), 871(w), 756(m), 725(m). Analysis calculated (found, %) for(%) $C_{57}H_{36}N_9O_3Tb{\cdot}0.4CHCl_3$: C, 62.58 (62.60); H, 3.33 (3.21); N, 11.44 (11.50). MS(ESI+)= 1054.2(MH^+). UV-Vis (CH_2Cl_2) λ_{max} (ϵ, ($M^{-1}cm^{-1}x10^4$): 380nm (2), 525nm (6) 560nm (6).

Dy(PAPL)$_3$(4.3) Compound 3.1 (0.1217g, 0.407mmol) was dissolved in chloroform (5mL) and 5 drops of triethylamine were added. $Dy(NO_3)_3 \cdot xH_2O$ was dissolved in methanol (5mL) and was added dropwise to the solution which was

allowed to stir for 2 hours. A purple precipitate was produced, collected by vacuum filtration, washed with water and methanol, and then dried. Yield (0.0863g, 58.7%). FT-IR (KBr): 3062(w), 1597(m), 1584(m), 1559(m), 1512(s), 1493(s), 1437(m), 1389(w), 1341(m), 1319(s), 1294(m), 1277(s), 1227(s), 1207(m), 1179(s), 1161(m), 1140(s), 1126(m), 1101(m), 1034(m) 999(m), 928(w), 872(w), 754(m), 725(m), 654(w). Analysis calculated (found, %) for $C_{57}H_{36}N_9O_3Dy$: C, 64.74 (65.19); H, 3.43 (3.25); N, 11.92 (12.00). MS(ESI+) =1059.2 (MH^+). UV-Vis (CH_2Cl_2) λ_{max} (ϵ, ($M^{-1}cm^{-1}x10^4$): 380nm (2), 525nm (6) 560nm (6).

2.3.3 Synthesis for Chapter 5

8-hydrazinoquinoline(5.1) Hydrazine hydrate (30ml) was purged with N_2 and 8-hydroxyquinoline (3.00g, 20.7mmol) was added to the reaction flask. The contents were heated to 120^oC and allowed to stir for 48 hours. The reaction mixture was cooled to room temperature with 5.1 crystallizing as yellow needle shaped crystals. As 5.1 is air sensitive recrystallization can be preformed by dissolving in a 1:1 mixture of hexane to ethanol, and then allowing for slow recrystallization at -5^oC. Yield (2.53g, 77%). ^1H NMR (400MHz, $CDCl_3$): 8.73ppm (1H, dd, J=4.2, 1.6Hz), 8.09ppm (1H, dd, J=8.4Hz, 1.6Hz), 7.47ppm (1H, dd, J=7.9Hz), 7.39ppm (1H, dd, J=8.3Hz, 4.2Hz), 7.28ppm (1H, bs), 7.17ppm (1H, dd, J=8.20Hz, 1.2Hz), 7.09ppm (1H, dd, J=7.6Hz, 1.0Hz), 3.70ppm (2H, bs). ^{13}C NMR (100MHz, $CDCl_3$, ppm): 147.4, 147.2, 137.7, 135.9, 121.6, 116.0, 105.8.

1-(8-quinolynazo)-2-phenanthrol(QAPL)(5.2) 9,10-phenanthrenequinone (289mg, 1.39mmol) was dissolved in 15ml of glacial acetic acid and heated to 70^oC. 5.1 (0.600g, 3.77mmol) was then added and the reaction was heated to reflux and allowed to react for 12 hours producing a a crude dark red reaction mixture. The crude product was purified on silica using a mixture of 1:1 hexanes/DCM. Yield (53mg, 11%). HR-MS (EI): Calculated for (found) $C_{23}H_{15}ON_3$ 349.1210 (349.1208). ^1H NMR (400MHz, $CDCl_3$): 9.10ppm (1H, d, J=4.4Hz), 8.67ppm-8.62ppm (2H, m), 8.32ppm (2H, dd, J=8.8Hz), 8.23ppm (2H, dd, J=9.7Hz), 7.75ppm (1H, dd, J=7.0Hz), 7.71-7.61ppm (2H, m), 7.58-7,46 (4H, m). ^{13}C NMR (100MHz, $CDCl_3$, ppm): 206.9, 179.5, 149.7, 138.9, 136.2, 135.9, 133.4, 132.6, 121.2, 130.2, 128.6, 128.4, 128.4, 127.5, 127.5, 127.2, 127.1, 123.2, 123.1, 122.9, 122.0, 112.7. FT-IR (KBr, cm^{-1}): 2957cm(s), 1595(m), 1506(s), 1477(s), 1281(s), 1211(s), 1018(m), 787(m), 748(m), 725(m). UV-Vis (CH_2Cl_2) λ_{max} (ϵ, ($M^{-1}cm^{-1}x10^4$): 500nm (3).

$\mathbf{[Co(QAPL)_2]Cl \cdot 1.5CH_3CN \cdot H_2O(5.3)}$ Compound 5.2 (52mg, 0.15mmol) was dissolved in a mixture of dry acetonitrile and DCM under N_2, and 5 drops of triethylamine were added. $CoCl_2 \cdot 6H_2O$ (20.8, 0.088mmol) was then added and stirred for 12 hours which produced a clear purple solution. Dry diethyl ether was layered on the solution which was allowed to evaporate for 7 days which produced 5.3 as purple square crystals suitable for X-ray diffraction. Yield (35mg, 55%). FT-IR(KBr, cm^{-1}): 1605(w) 1582(w), 1505(m), 1489(m), 1445(m), 1352(s), 1313(s), 1242(m), 133(m), 1242(m), 1233(m), 1161(m), 1132(w), 1109(m),

1038(m), 976(m), 831(m), 754(m), 721(m). Analysis calculated $CoC_{46}H_{28}N_6O_2 \cdot 1.5CH_3CN \cdot H_2O$ (found, %): C, 67.59 (67.87); H, 3.99 (4.19); N, 12.06 (11.78) . UV-Vis (CH_2Cl_2) λ_{max} (ϵ, ($M^{-1}cm^{-1}x10^4$): 400nm (0.9) 600nm (2).

Fe(QAPL)$_2$(5.4) Compound 5.2 (50mg, 0.14 mmol) was dissolved in a mixture of chloroform(5mL) and methanol(5mL) and 5 drops of triethylamine was added. $Fe(NO_3)_3 \cdot 9H_2O$ (31mg, 0.08mmol) was added and the mixture allowed to stir for 5 hours producing a clear black solution. The reaction mixture was diluted with 15mL of methanol, and allowed to slowly evaporate over 10 days producing black plate crystals suitable for X-ray diffraction. Yield (38mg, 71%). FT-IR(KBr,cm^{-1}):1595(m), 1506(s), 1477(s), 1446(m), 1342(m), 1283(s), 1215(s) 1159(w), 1101(w), 1080(w), 1028(m), 819(w), 787(w), 758(s), 723(s). Analysis calculated $FeC_{46}H_{28}N_6O_2$ (found, %): C, 73.81 (73.18); H, 3.23 (3.55); N, 11.23 (10.90). UV-Vis (CH_2Cl_2): λ_{max} (ϵ, ($M^{-1}cm^{-1}x10^2$): 500nm (300), 800nm (6), 1050nm (7).

Chapter 3

Transition Metal Complexes with 1-(2-pyridylazo)-2-phenanthrol (M=V(V),Fe(II), Fe(III), Co(II), Cu(II), and Ru(II))

3.1 Introduction

1-(2-pyridylazo)-2-phenanthrol (PAPL) complexes of first row transition metals Cu(II), Co(II), Fe(II), Fe(III) and V(V) were synthesized, as well as a complex of a second row transition metal complex Ru(II). Reduction attempts were also

made on both the complexes, and the ligand itself with the goal of synthesizing metal complexes with paramagnetic ligands.

3.2 1-(2-pyridylazo)-2-phenanthrol(PAPL) (3.1)

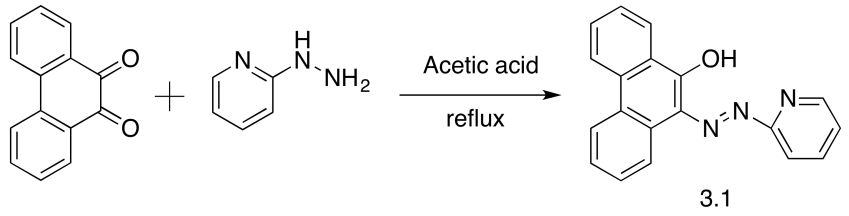

3.1

SCHEME 3.1: Synthesis of 3.1 (PAPL)

Compound 3.1 is obtained as an orange powder that is of sufficient purity for coordination after precipitation from the reaction mixture by neutralizing the acidic solution. In the uncoordinated state, 3.1 is soluble in many solvents including chloroform, DCM, acetonitrile, THF, methanol, ethanol, toluene, and hexanes. This allows for the ligand to be coordinated in a variety of reaction conditions.

In its free form, 3.1 exists as a mixture of tautomers (scheme 3.2). Upon binding to a metal ion, the ligand has been shown to bind exclusively in the enolate state in a tridentate[58][59] fashion with a coordination pocket that generally includes N_{py}, N_{azo}, and $O^{-}_{phenanthrol}$ donor atoms. As the enol tautomer contains the azo moiety, coordination of a metal ion to the PAPL ligand forms complexes having strong visible absorption bands, and therefore significant dye-like properties.

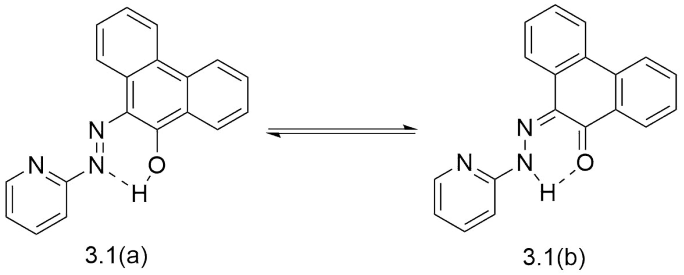

SCHEME 3.2: The keto/enol tautomerization of 3.1: The keto tautomer on the right, enol tautomer on the left.

3.3 $Co(PAPL)_2 \cdot CH_2Cl_2$(3.2)

3.3.1 Structural Characterization

Attempts were made previously to synthesize a divalent cobalt PAPL complex using a cobalt(II) metal source. An early paper by Bhoon and co-workers presented a Co(II) complex[57] whose variable temperature magnetic susceptibility experiments suggested exhibited spin crossover, though it was lacking structural verification. Early attempts to replicate this result, however, generated a trivalent salt[59]. With enough persistence 3.2 was successfully prepared as a blue microcrystalline powder, by direct precipitation from acetonitrile under N_2 using a Co(0) source. The powder was collected by vacuum filtration and then redissolved into the reaction mixture using DCM to remove any remaining dicobalt octacarbonyl, or cobalt oxide that are generated from the carbonyl source, from the powder. The reaction mixture was then layered with diethyl ether which was then allowed to diffuse into the reaction mixture to cause 3.2 to precipitate in a microanalytically pure form with the addition of $1mol$ of DCM. The FT-IR spectrum is typical of

$M(PAPL)_2$ complexes. After separation of the powder by vacuum filtration, the reaction mixture was allowed to slowly evaporate which produced dark blue plate crystals of 3.2. The previously precipitated powder is shown to have the same structure as the single crystals, which was determined by comparison of experimental pXRD on the powder (figure A.1), and simulated pXRD from the single crystal structure (figure A.2). This allowed for the characterization of 3.2 to be performed on the powder sample, with assurance that the single crystal properties were the same.

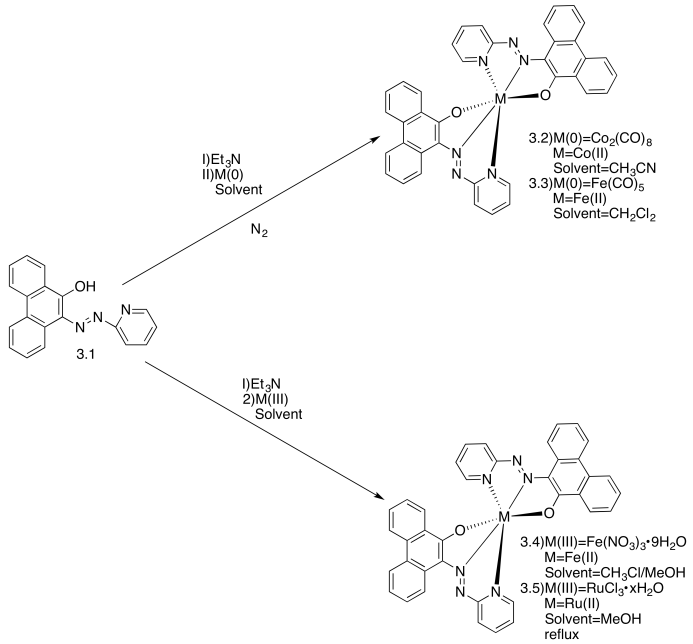

Scheme 3.3: Synthetic scheme of compounds 3.2, 3.3, 3.4, and 3.5

Single crystal X-ray diffraction was carried out at two temperatures [147(2)K and 325(2)K] on the same single crystal to confirm the spin switching nature of this molecule (see section 3.3.2). The crystal structures are shown in figures 3.1 and 3.2, respectively.

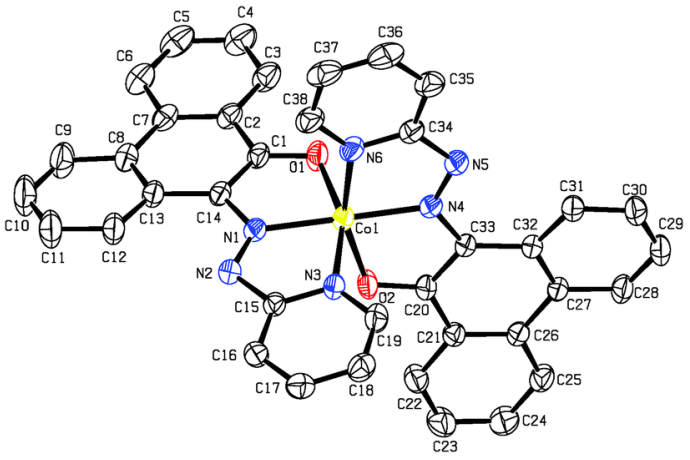

FIGURE 3.1: Displacement ellipsoid plot of 3.2 at 147K: H atoms are omitted for clarity. Select bond distances ($\mathring{A}$) and angles (^{o}) with uncertainties in brackets: Co(1)–N(1), 1.9221(18); Co(1)–N(4), 1.9091(18); Co(1)–N(3), 2.042(2); Co(1)–N(6), 2.011(2); Co(1)–O(1), 2.0786(17); Co(1)–O(2), 2.0416(16); N(1)–N(2), 1.303(3); N(4)–N(5), 1.312(3); C(1)–O(1), 1.273(3); C(20)–O(2), 1.270(2); C(14)–N(1), 1.367(3); C(33)–N(4), 1.362(3). N(4)–Co(1)–N(1), 179.75(10); N(4)–Co(1)–N(6), 79.24(8); N(1)–Co(1)–N(6), 100.51(7); N(4)–Co(1)–O(2), 80.45(7); N(1)–Co(1)–O(2), 99.79(7); N(6)–Co(1)–O(2), 159.69(7); N(4)–Co(1)–N(3), 101.43(8); N(1)–Co(1)–N(3), 78.60(8); N(6)–Co(1)–N(3), 95.38(8); O(2)–Co(1)–N(3), 88.72(7); N(4)–Co(1)–O(1), 100.19(7); N(1)–Co(1)–O(1), 79.80(7); N(6)–Co(1)–O(1), 90.81(8); O(2)–Co(1)–O(1), 92.67(7); N(3)–Co(1)–O(1), 158.27(7).

At both temperatures the molecule is neutral, and features a six coordinate cobalt ion. Two equivalents of the anionic PAPL ligand are bound along meridional coordination sites with N_{py}, N_{azo} and O^- donor atoms. In the low temperature structure the coordinate bond distances are quite different than previously reported for structurally characterized PAPL complexes[58][59]. Attention should be drawn to the $Co - N_{azo}$ bonds Co1-N1 and Co1-N4, which are shorter than what is seen in previous complexes. This is attributed to metal to ligand back bonding in the low temperature, low spin isomer in addition to a tetragonal compression due to Jahn-Teller distortion. The shorter of the two bonds, Co1-N4,

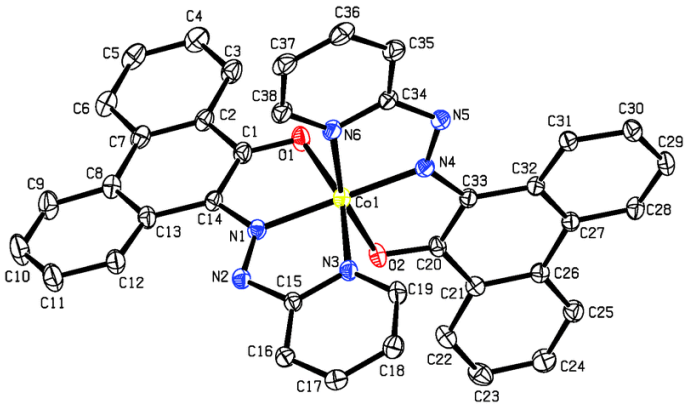

FIGURE 3.2: Displacement ellipsoid plot of 3.2 at 325K: H atoms are omitted for clarity. Select bond distances ($\mathring{A}$) and angles (^{o}) with uncertainties in brackets: Co(1)–N(1), 1.9127(17); Co(1)–N(4), 1.8651(17); Co(1)–N(3), 2.0479(18); Co(1)–N(6), 1.9685(18); Co(1)–O(1), 2.1224(16); Co(1)–O(2), 1.9982(15); N(1)–N(2), 1.307(2); N(4)–N(5), 1.314(2); C(1)–O(1), 1.271(3); C(20)–O(2), 1.279(2); C(14)–N(1), 1.367(3); C(33)–N(4), 1.367(3). N(4)–Co(1)–N(1), 179.14(8); N(4)–Co(1)–N(6), 80.46(7); N(1)–Co(1)–N(6), 99.33(7); N(4)–Co(1)–O(2), 82.31(7); N(1)–Co(1)–O(2), 97.93(6); N(6)–Co(1)–O(2), 162.64(7); N(4)–Co(1)–N(3), 100.07(7); N(1)–Co(1)–N(3), 79.11(7); N(6)–Co(1)–N(3), 95.63(7); O(2)–Co(1)–N(3), 89.39(7); N(4)–Co(1)–O(1), 101.40(7); N(1)–Co(1)–O(1), 79.43(7); N(6)–Co(1)–O(1), 90.37(7); O(2)–Co(1)–O(1), 91.02(6); N(3)–Co(1)–O(1), 158.38(6).

is significantly shorter at 1.8651(17)$\mathring{A}$ and is accompanied by an enlargement of the azo bond (N4-N5) as compared to the previously reported PAPL complexes to a bond distance of 1.314(2)$\mathring{A}$. This indicates cobalt back donation to the azo centered LUMO, though not enough to fully reduce the bond (and oxidize the metal).

A comparison of the coordinate bonds at 147K and 325K is shown in figure 3.3 as evidence for the spin crossover that occurs in this molecule. At low temperature the average coordinate bond length is shorter. However, as the temperature is increased, four of the six coordinate bonds in the molecule lengthen due to the

increase in the antibonding nature of the molecular orbitals. This increased anti-bonding nature is due to the movement of electrons from the non-bonding (t_{2g}) to the anti-bonding (e_g^*) orbitals while the bonds of the Jahn-Teller axis shorten due to the weakening of the Jahn-Teller effect in the high spin state.

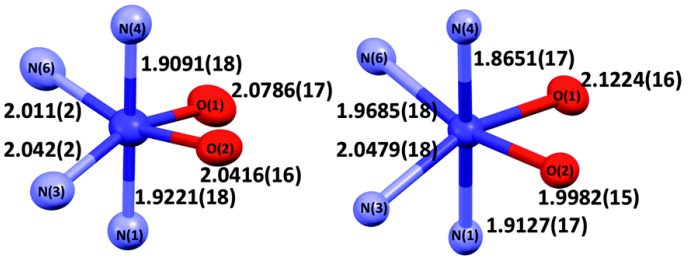

FIGURE 3.3: Coordinate bond lengths of 3.2 in both the high spin state(left) and low spin state(right): Bond lengths in $\mathring{A}$

3.3.2 Magnetic properties

The solid state variable temperature magnetic susceptibility data was collected by SQUID magnetometry over a range of 2 to 300K at a field of $2000Oe$. The data is shown as a plot of $\chi_m T$vs$T$ in figure 3.4. At 300K $\chi_m T \approx 2.4 cm^3 K mol^{-1}$, which is significantly larger than the spin only value for the quartet ($S = 3/2$) state of high spin Co(II). This result is expected as many high spin Co(II) complexes have unquenched orbital angular momentum in the ground state, and therefore have higher than spin only values for $\chi_m T$. As the temperature is decreased there is steady gradual decrease in $\chi_m T$ that occurs over the entire temperature range until $\approx 5K$ where $\chi_m T$ reaches a value of approximately $0.80 cm^3 K mol^{-1}$, which is near the expected spin only value for the doublet ($S = 1/2$) state of low spin

Co(II). Between 5K and 2K there is a steady drop in the value for $\chi_m T$ which is attributed to intermolecular antiferromagnetic exchange interactions. Finally the data points collected upon warming fall almost exactly on top of the data points upon cooling, indicating an absence of thermal hysteresis in the spin crossover.

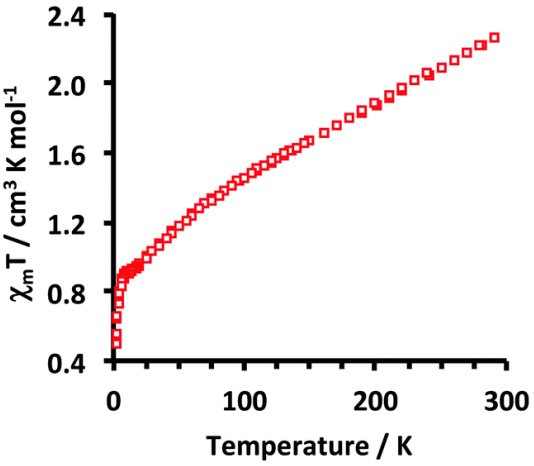

FIGURE 3.4: Magnetic susceptibility profile for 3.2 over a temperature range of 2K to 300K (field: 2000Oe)

In order to support the claim of spin crossover in this system, powder EPR was performed at two temperatures. At 100K an isotropic spectrum (figure 3.5) indicative of low spin cobalt(II) was observed, while at room temperature, no EPR spectrum was observed. This is common for high spin cobalt(II) complexes[80]. This result confirms the presence of spin crossover in 3.2.

3.3.3 Electronic Properties

The electronic spectrum of 3.2 was measured at room temperature in chloroform (figure 3.6). It consists of several bands. The most intense band has a maximum at

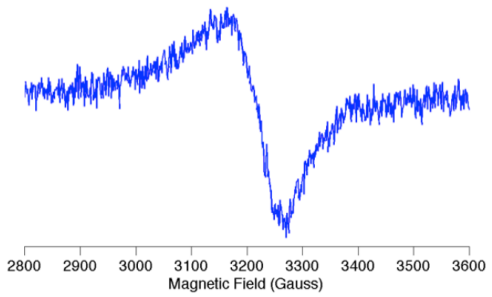

FIGURE 3.5: Powder EPR spectrum for 3.2 at 100K.

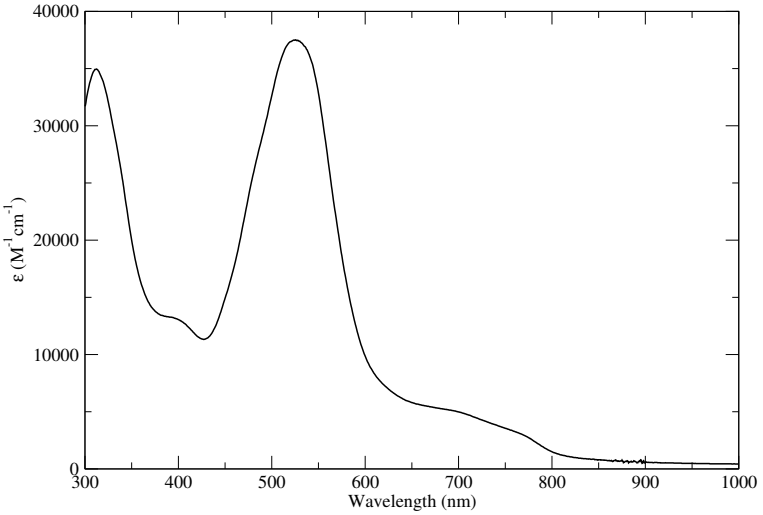

FIGURE 3.6: UV-Visible spectrum of 3.2: performed in chloroform

Complex	$E_{1/2}$ anodic (V vs Ag/AgCl)	$E_{1/2}$ cathodic (V vs Ag/AgCl)
3.2	1.6(qr)	-0.1(qr), -0.9(qr), -1.5(qr)
3.3	0.4(qr), 1(irr), 1.6(qr)	-1.1(irr), -1.6(qr)
3.4	0.4(qr), 1.5(qr)	-1.5(qr), -1.1(qr), -0.8(qr)
3.5	0.2(qr), 0.8(qr)	-0.5(qr), -0.8(qr) -1.5(qr)
3.6	0.2(irr), 0.8(irr), 1.3(irr)	-1.0(irr), -1.2(irr), -1.4(qr), -1.7(qr)
3.8	-	-0.3(irr), -0.5(irr), -0.9(irr), -1.4(irr)

TABLE 3.1: Electrochemical data for transition metal PAPL complexes

532nm, that is approximately half as intense as the previously reported structurally analogous nickel and zinc PAPL complexes[58]. There is a low energy shoulder which is not present in other PAPL complexes[58]. The high energy absorption bands are assigned as ligand centered transitions from time-dependent density functional theory(TD-DFT) calculations, while the lower energy bands are likely of metal-to-ligand charge transfer (MLCT) character.

As 3.2 possesses a temperature dependent spin crossover, variable temperature UV-Vis was used to determine whether spin crossover was present in solution. However, the spectrum (in toluene) is constant down to 183K.

It is important to note that while the complex is stable to oxidation in air when dissolved in non-polar aprotic solvents (DCM, chloroform, toluene, and acetonitrile), when dissolved in alcoholic solvents (ethanol, methanol, and isopropanol) there is an immediate colour change in solution, and the electronic spectrum measured is that of the previously reported cobalt(III) complex[59]. A DCM solution, which is diluted with ethanol, and then allowed to run consecutively over an hour is shown in figure 3.7, which shows the oxidation of Co(II) to Co(III) in solution.

The electrochemical data are summarized in table 3.1, the cyclic voltammogram (CV) is figure 3.8, and the differential pulse voltammograms (DPV(s)) are figure 3.9. At cathodic potentials there are three quasi-reversible waves at -0.1V, -0.9V, and -1.5V. The wave at -0.1V is assigned as the $Co^{3+/2+}$ couple while the waves at -0.9V and -1.5V are azo centered reductions of the ligand. At anodic potentials

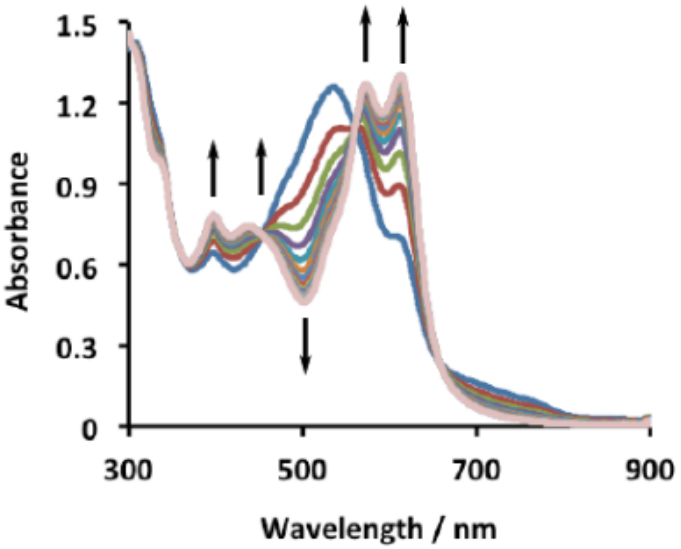

FIGURE 3.7: UV-Visible spectra of 3.2 in DCM titrated with EtOH: The final spectrum is the peach trace.

there is a broad quasi-reversible wave centered at 1.5V which is assigned as a ligand based oxidation.

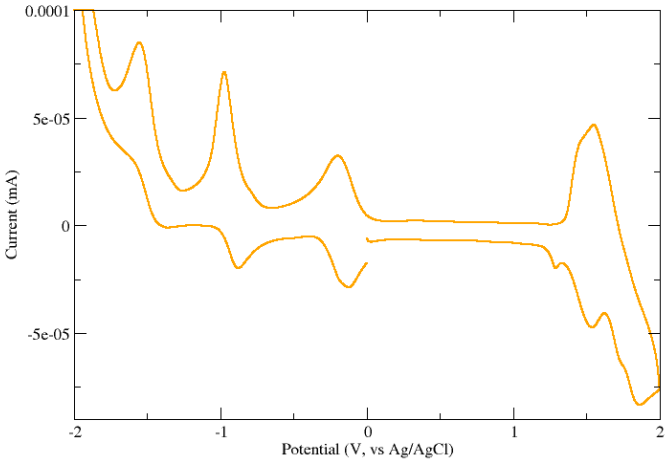

FIGURE 3.8: CV of 3.2 in acetonitrile over the range of -2V to 2V at a scan rate of 100mV/s

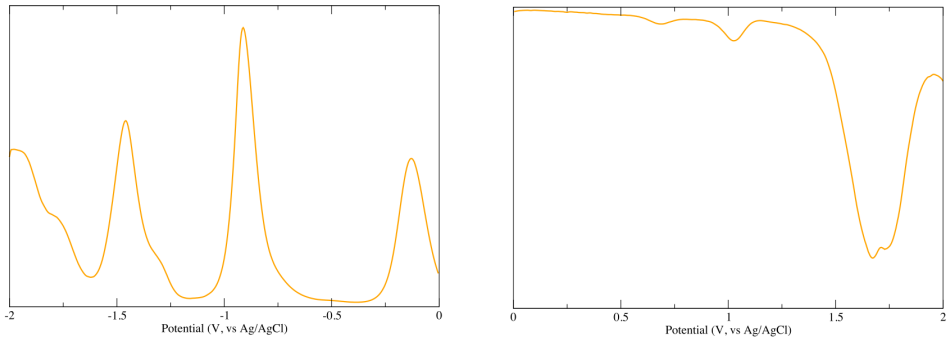

FIGURE 3.9: Left: Cathodic DPV of 3.7, over the range of -2.0V to 0V Right: Anodic DPV of 3.7, over the range of 0V to 2V. In both cases performed in acetonitrile, y-axis is μA.

3.4 $Fe(PAPL)_2$(3.3 – 3.4)

3.4.1 Structural Characterization

A divalent iron species was successfully synthesized from two different reactions. One starting from an Fe(0) source (iron pentacarbonyl(3.3)), and a second from a Fe(III) source (iron nitrate(3.4)). In the first case 3.3 is obtained as large green needle crystals by diffusion of diethyl ether into the DCM reaction mixture under N_2. The crystals were coated with a brown powder that proved impossible to completely remove. In the second case 3.4 is obtained as a black microcrystalline powder, that precipitated directly out of solution. Green plate like crystals of 3.4 were grown by diffusion of *n*-pentane into a THF solution of 3.4.

The FT-IR spectra of 3.3 and 3.4 are identical (figure 3.10), and free of any NH/OH stretches that would indicate uncoordinated 3.1. The microanalytical

analysis of 3.3 indicates the presence of 1 equivalent of DCM in the lattice, while microanalytical analysis indicates 0.6 equivalents of THF in the lattice of 3.4.

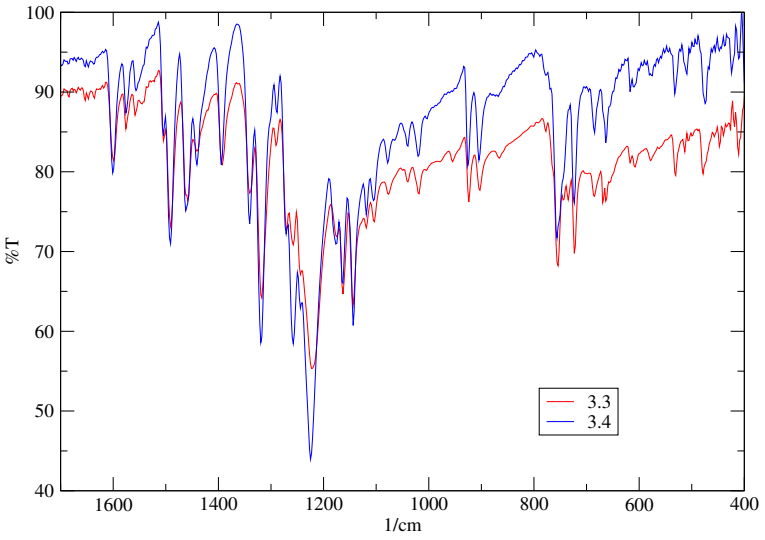

FIGURE 3.10: FT-IR spectra of 3.3 and 3.4

The molecular structures of 3.3 at 120K and 250K are shown in figure 3.11. Compound 3.3 exhibits a structural phase transition at temperatures below 140K. The bond angles and lengths for the molecule at different temperatures are only slightly different, and in both cases suggestive of low spin Fe(II). The azo bonds in this molecule are of a length between 1.312(7) and 1.314(2)$\mathring{A}$, which is slightly longer than in other reported complexes of 3.1[58], and is likely due to Fe(II) back-bonding to the azo-centred LUMO.

The packing diagram for 3.3 in the *bc* plane at both temperatures (figure 3.12) illustrates the structural phase transition. The phase transition is accompanied by a change in the crystal system from monoclinic to triclinic with decreasing temperature.

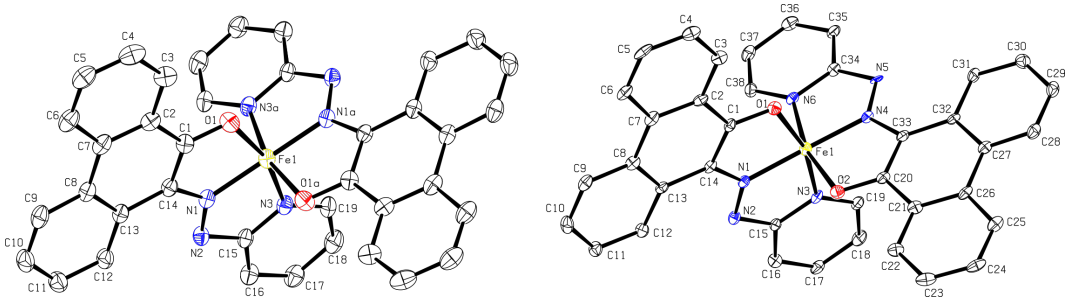

FIGURE 3.11: Displacement ellipsoid plot of 3.3 at 250(2)K(left) and 120(2)K(right: H atoms and DCM omitted for clarity. Bond lengths in $\mathring{A}$, and bond angles in ^{o}: For left structure:Fe1-O1, 1.9547(16); Fe1-O1a, 1.9547(16); Fe1-N1, 1.8627(19); Fe1-N1a, 1.8626(19); Fe1-N3, 1.932(2); Fe1-N3a, 1.932(2); N1-N2, 1.314(3); C1-O1, 1.296(3); C14-N1, 1.375(3); C1-C14, 1.407(3). N1a-Fe1-N1, 179.66(12); N1a-Fe1-N3a, 80.66(8); N1-Fe1-N3a, 99.58(8); N1a-Fe1-O1a, 82.82(7); N1-Fe1-O1a, 96.94(7); N3a-Fe1-O1a, 163.41(7); N1a-Fe1-N3, 99.58(8); N1-Fe1-N3, 80.66(8); N3a-Fe1-N3, 89.35(11); O1a-Fe1-N3, 91.94(7); N1a-Fe1-O1, 96.94(7); N1-Fe1-O1, 82.82(7); N3a-Fe1-O1, 91.94(7); O1a-Fe1-O1, 91.52(10); N3-Fe1-O1, 163.41(7). For right structure: Fe1-O1, 1.960(4); Fe1-O2, 1.944(4); Fe1-N1, 1.862(5); Fe1-N3, 1.939(5); Fe1-N4, 1.859(5); Fe1-N6, 1.923(5); N1-N2, 1.313(7); N4-N5, 1.312(7); C1-O1, 1.298(7); C20-O2, 1.295(7); C14-N1, 1.382(8); C33-N4, 1.375(8); C1-C14, 1.401(8); C20-C33, 1.401(8). N4-Fe1-N1, 179.2(2); N4-Fe1-N6, 80.6(2); N1-Fe1-N6, 100.1(2); N4-Fe1-O2, 83.3(2); N1-Fe1-O2, 96.0(2); N6-Fe1-O2, 163.80(19); N4-Fe1-N3, 99.1(2); N1-Fe1-N3, 80.6(2); N6-Fe1-N3, 88.88(16); O2-Fe1-N3, 92.4(2); N4-Fe1-O1, 97.3(2); N1-Fe1-O1, 83.1(2); N6-Fe1-O1, 92.0(2); O2-Fe1-O1, 91.41(15); N3-Fe1-O1, 163.52(19).

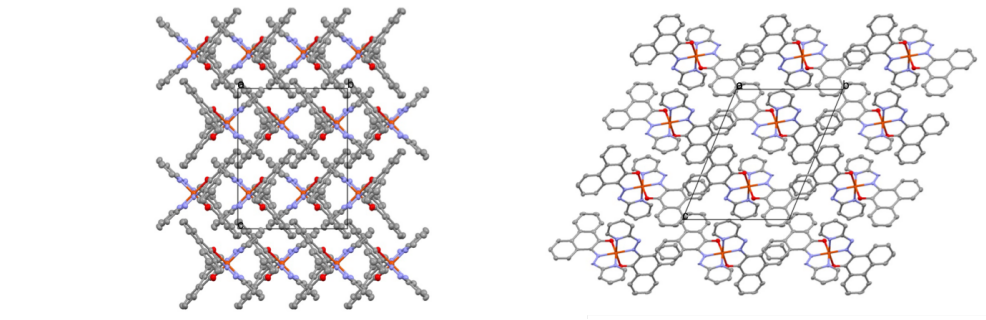

FIGURE 3.12: Packing diagram of 3.3 in the bc plane at 120(2)k (left) and 250(2)K (right), DCM and hydrogen atoms excluded for clarity

The molecular structure of 3.4 is shown in figure 3.13 with selected bond distances and angles in the caption. Though Fe(III) was used in the coordination reaction, the metal ion was reduced during the reaction to producing another polymorph of $Fe(PAPL)_2$. The crystal structure belongs to the orthorhombic crystal group, and contains two different structural configurations in the asymmetric unit. The coordinate bonds of the first molecule are of lengths typical for low-spin Fe(II). The azo bond distances (1.310(6)$\mathring{A}$ and 1.291(6)$\mathring{A}$) are typical for N=N double bonds. In the second molecule, the N=N bond lengths of 1.330(6)$\mathring{A}$ and 1.319$\mathring{A}$ are slightly longer than the typical N-N double bonds seen for $M(PAPL)_2$ complexes, however, these bonds are still of azo character. The larger azo bond lengths are likely due to back-bonding from the Fe(II) ion.

The packing diagram of 3.4 in the *bc* plane (figure 3.14) reveals that molecule 3.4 forms chains along the *c*-axis with short intermolecular π contacts with length of approximately 3.529$\mathring{A}$ and 3.799$\mathring{A}$. The shorter contact is between the centroids of the central ring of the phenanthrol fragment on one molecule with an outer ring of the phenanthrol group from an adjacent molecule, while the longer contact occurs between pyridine ring and outer ring phenanthrol centroids.

3.4.2 Magnetic Properties

The variable temperature magnetic properties of 3.3 and 3.4 were investigated. SQUID magnetometry was performed on 3.4 in the solid state over a temperature

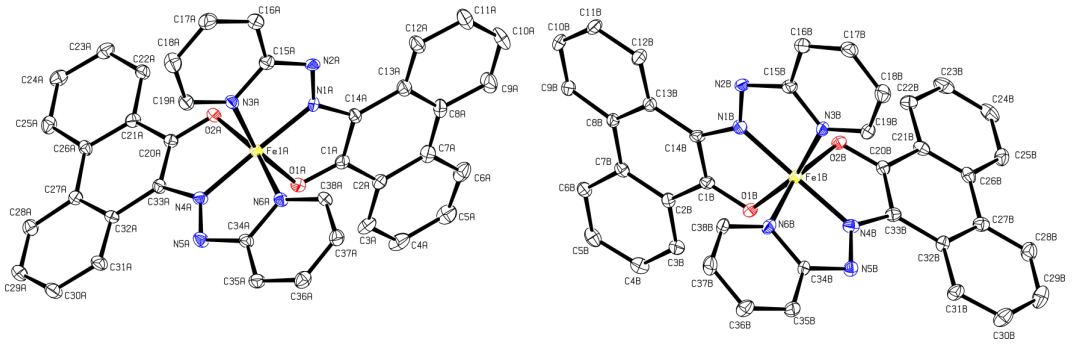

FIGURE 3.13: Displacement ellipsoid plot of 3.4: H atoms omitted for clarity. Bond lengths in $\AA$, and bond angles in ^{o}: Fe(1B)-N(4B), 1.864(5); Fe(1B)-N(1B), 1.870(4); Fe(1B)-N(6B), 1.940(5); Fe(1B)-N(3B), 1.940(5); Fe(1B)-O(2B), 1.944(4); Fe(1B)-O(1B), 1.961(4); O(1B)-C(1B), 1.293(6);O(2B)-C(20B), 1.286(7); N(1B)-N(2B), 1.319(6); N(4B)-N(5B), 1.330(6); Fe(1A)-N(4A), 1.873(4); Fe(1A)-N(1A), 1.877(4); Fe(1A)-N(6A), 1.922(5); Fe(1A)-N(3A), 1.924(5); Fe(1A)-O(2A), 1.966(4); Fe(1A)-O(1A), 1.969(4); O(1A)-C(1A), 1.277(6); O(2A)-C(20A), 1.291(6); N(1A)-N(2A), 1.291(6); N(4A)-N(5A), 1.310(6). N(4B)-Fe(1B)-N(1B), 178.0(2); N(4B)-Fe(1B)-N(6B), 80.2(2); N(1B)-Fe(1B)-N(6B), 98.99(19); N(4B)-Fe(1B)-N(3B), 98.00(18); N(1B)-Fe(1B)-N(3B), 80.23(18); N(6B)-Fe(1B)-N(3B), 92.0(2); N(4B)-Fe(1B)-O(2B), 82.71(18); N(1B)-Fe(1B)-O(2B), 98.15(17); N(6B)-Fe(1B)-O(2B), 162.86(17); N(3B)-Fe(1B)-O(2B), 91.10(18); N(4B)-Fe(1B)-O(1B), 99.02(17); N(1B)-Fe(1B)-O(1B), 82.75(17); N(6B)-Fe(1B)-O(1B), 90.70(17); N(3B)-Fe(1B)-O(1B), 162.98(16); O(2B)-Fe(1B)-O(1B), 91.21(16); N(4A)-Fe(1A)-N(1A), 178.39(19); N(4A)-Fe(1A)-N(6A), 80.39(18); N(1A)-Fe(1A)-N(6A), 98.04(18); N(4A)-Fe(1A)-N(3A), 99.96(19); N(1A)-Fe(1A)-N(3A), 80.42(19); N(6A)-Fe(1A)-N(3A), 92.54(19); N(4A)-Fe(1A)-O(2A), 82.74(17); N(1A)-Fe(1A)-O(2A), 98.84(17); N(6A)-Fe(1A)-O(2A), 163.12(16); N(3A)-Fe(1A)-O(2A), 90.59(17); N(4A)-Fe(1A)-O(1A), 96.96(17); N(1A)-Fe(1A)-O(1A), 82.71(17); N(6A)-Fe(1A)-O(1A), 91.65(17); N(3A)-Fe(1A)-O(1A, 163.02(17); O(2A)-Fe(1A)-O(1A), 90.16(16).

range of 2K to 300K (figure B.2). The data indicates that complex 3.4 is diamagnetic. The SQUID data from samples of 3.3 indicates paramagnetism (figure B.1), however, the data from 3.3 is sample dependent with a wide variation in $\chi_m T$, which is certainly due to either a non-iron magnetic impurity, or an iron containing impurity that was in a low enough concentration to go undetected by Mössbauer spectroscopy.

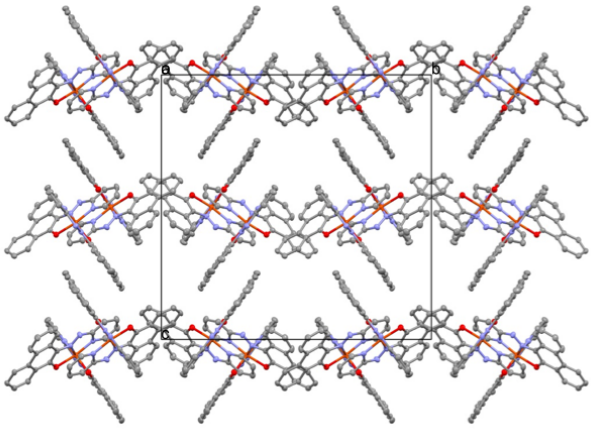

FIGURE 3.14: Packing diagram of 3.4 in the *bc* plane, Hydrogen atoms excluded for clarity

Temperature	δ (mm/s)	ΔE_Q (mm/s)	Γ (mm/s)
6K	0.212(2)	0.509(3)	0.317(3)
150K	0.191(2)	0.498(3)	0.255(4)
293K	0.140(2)	0.523(4)	0.243(4)

TABLE 3.2: Mössbauer data for 3.3

Variable temperature Mössbauer spectroscopy was performed on both 3.3 and 3.4, which produced nearly identical spectra at all temperatures (figure 3.15, and tables 3.2 and 3.3). The data agrees with an early study by Singh and co-workers[56]. The small quadrupole splitting in the spectra of 3.3-3.4 is indicative of low spin Fe(II), while the isomer shift values are in-line with Fe(II) complexes[81]. This data along with similar structural data obtained for 3.3 and 3.4 supports the assertion that 3.3 is diamagnetic.

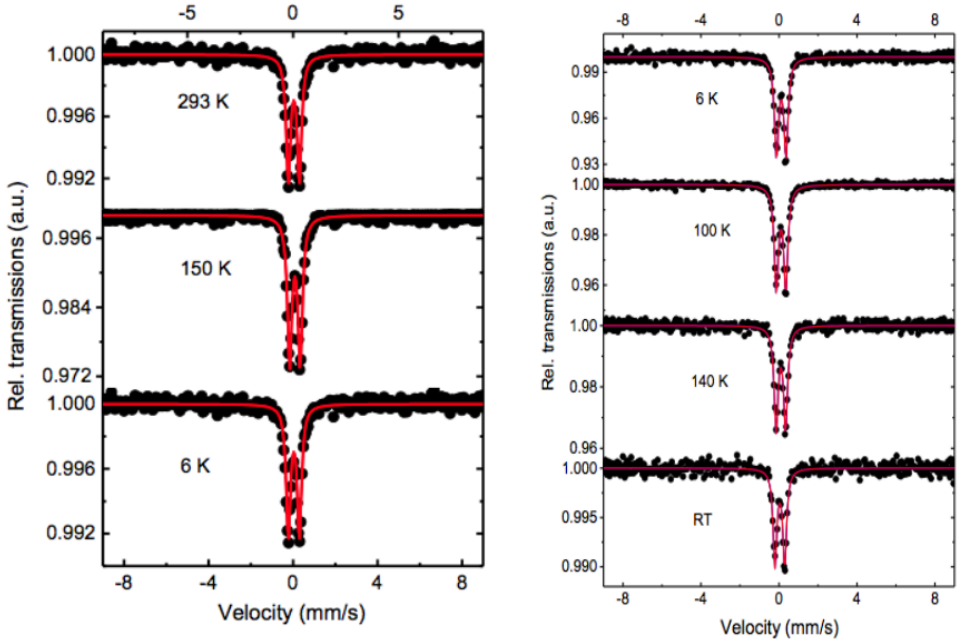

FIGURE 3.15: Variable temperature Mössbauer spectra performed on single crystals of 3.3 (left) and 3.4 (right) (zero field)

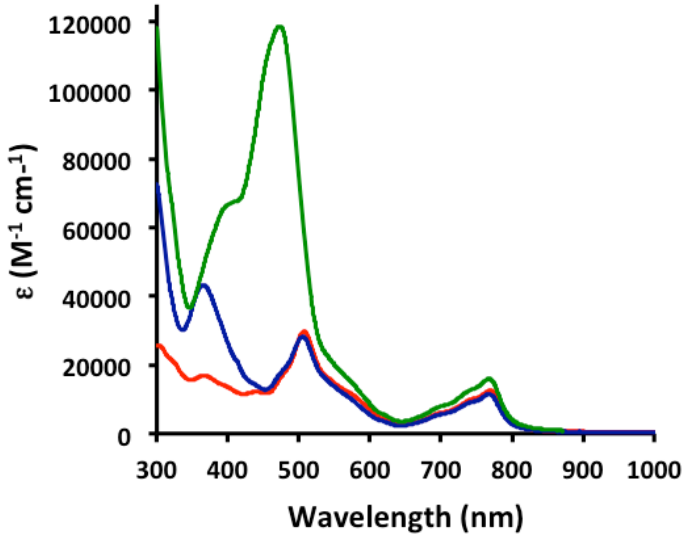

FIGURE 3.16: UV-Visible spectra of 3.3(green, with unknown impurity), 3.4 (red), and 3.7(blue). Performed in DCM for 3.3-3.4 and DMF for 3.7.

Temperature	δ (mm/s)	ΔE_Q (mm/s)	Γ (mm/s)
6K	0.218(2)	0.487(4)	0.256(5)
100K	0.209(1)	0.485(2)	0.255(3)
140K	0.197(2)	0.485(2)	0.246(6)
294K	0.145(4)	0.498(6)	0.235(7)

TABLE 3.3: Mössbauer data for 3.4

3.4.3 Electronic Properties

The UV-Visible spectra of 3.3 (green trace) and 3.4 (red trace) in DCM are plotted in figure 3.16. The spectra exhibit similar λ_{max} values. Of note is the low energy band at 767nm, which is not observed for other divalent PAPL complexes [58][59][82][83]. However, an older paper which describes 3.1 coordinated with a Pd(II) ion possesses this band [55]. Based on results from TD-DFT on complex 3.4 (*vide infra*), this absorption is assigned to be predominately of MLCT character. The significantly greater intensity in the spectrum of 3.3 is likely due to an undetermined paramagnetic impurity, which may be an uncoordinated radical anion of 3.1 as the band in the UV-Visible spectrum is at a similar wavelength to uncoordinated 3.1. The higher energy bands are typical of divalent complexes of 3.1, and are assigned as intra-ligand charge transfer (ILCT) bands.

The CV (figure 3.17) of 3.4 shows the usual quasi-reversible waves at cathodic potentials that are characteristic of 3.1 when bound to a divalent metal, and are assigned as the reduction of the azo moiety of each ligand. The Fe(3+/2+) couple is assigned to the wave at 0.5V, and at higher anodic potentials are likely irreversible ligand centered processes.

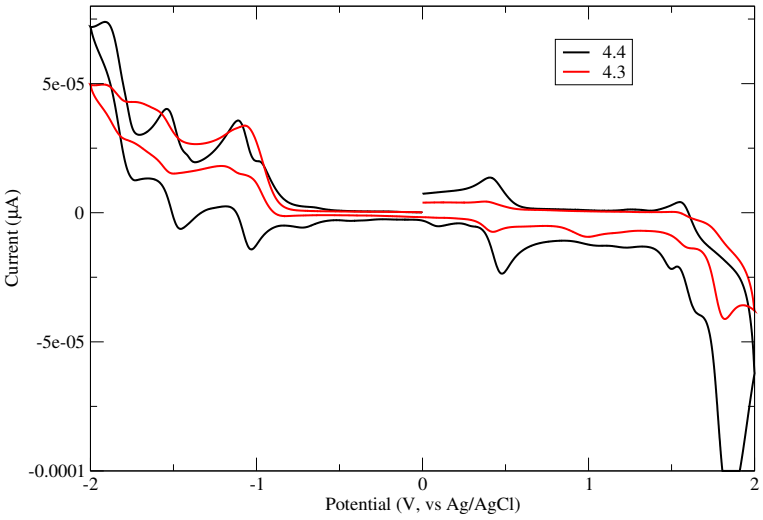

FIGURE 3.17: CV of 3.3 and 3.4 in DCM over the range of -2V to 2V at a scan rate of 100mV/s

3.4.4 Computational Chemistry

DFT calculations were performed on $Fe(PAPL)_2$ in the singlet state. The geometry of the complex was optimized using the atomic coordinates obtained from the structure of 3.4. The optimization of this complex agrees very well with the bond distances obtained from the X-ray determined structure (table 3.4). The composition of the HOMO and LUMO orbitals for the singlet state of $Fe(PAPL)_2$ are presented in figure 3.18. A Mulliken population analysis indicates that there is a large contribution from the iron centre (35%) in the HOMO of the ligand, which is significantly higher than other divalent complexes with 3.1[58], for which there is a much smaller metal contribution to the frontier molecular orbitals. The LUMO is largely ligand centered with components from the azo moiety, phenanthrol ring, and pyridine ring, with only a very small percentage on the Fe(II) ion.

Bond	Experimental length($\mathring{A}$)	Calculated length($\mathring{A}$)
$Fe-O$	1.944	1.951
$Fe-N_{pyr}$	1.932	1.933
$Fe-N_{azo}$	1.871	1.878
$N=N$	1.313	1.319
$C-O$	1.287	1.289

TABLE 3.4: Select experimental and computational bond lengths for $Fe(PAPL)_2$

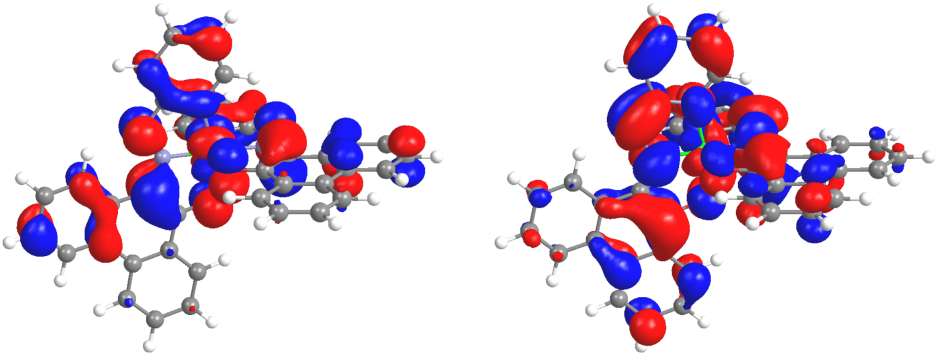

FIGURE 3.18: HOMO (left, 36% Fe) and LUMO (right, 9% Fe) for an $Fe(PAPL)_2$ in the singlet state calculated at the B3LYP/def2-TZVP level of theory (isovalue 0.02).

The UV-Visible spectrum of $Fe(PAPL)_2$ in chloroform was calculated using TD-DFT and the results are plotted in figure 3.19. The transitions at 835 and 826nm are much weaker then the experimentally observed transition at 760nm. These transitions are mainly of MLCT character, as there is a large Fe contribution in the HOMO. The intense higher energy transitions, which are predicted at 579 and 547nm, are generally of mixed ILCT and MLCT character.

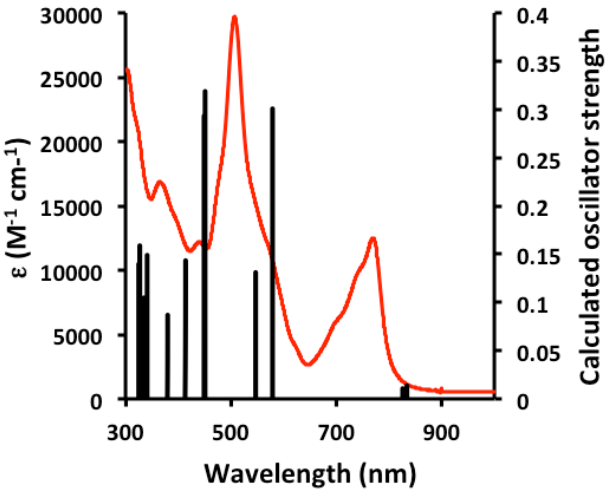

FIGURE 3.19: UV-visible spectrum of 3.4(red trace) in chloroform and calculated transitions for $Fe(PAPL)_2$ at the B3LYP/def2-TZVP level of theory in chloroform.

3.5 $Ru(PAPL)_2 \cdot 3.9CH_3OH(3.5)$

3.5.1 Structural Characterization

Complex 3.5 was prepared by refluxing $RuCl_3 \cdot xH_2O$ with 3.1 in methanol. Complex 3.5 is obtained as a black powder that precipitates out of the reaction solution upon cooling. Crystals were obtained by diffusion of *n*-pentane into a THF solution of 3.5 which produced black pentagon plate crystals.

Further attempts at crystal growth of 3.5 were unsuccessful, so characterization of the complex was performed on the precipitated powder, which was washed with water, methanol, and hexanes. Though the powder appears to be fully coordinated as evidenced by the FT-IR spectrum, which had no stretches $> 3000cm^{-1}$

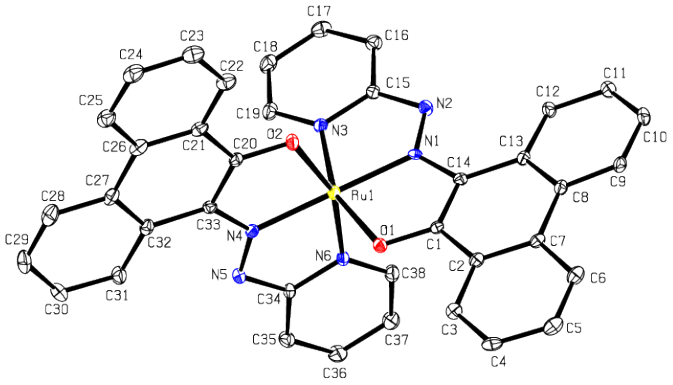

FIGURE 3.20: Displacement ellipsoid plot of 3.5: H atoms and THF molecules omitted for clarity. Select bond lengths ($\mathring{A}$) and bond angles (^{o}) with standard uncertainties in brackets:Ru(1)-N(1), 1.963(4); Ru(1)-N(4), 1.971(4); Ru(1)-N(6), 2.021(4); Ru(1)-N(3), 2.024(4); Ru(1)-O(2), 2.074(3); Ru(1)-O(1), 2.075(3); O(1)-C(1), 1.305(5); O(2)-C(20), 1.292(5); N(1)-N(2), 1.308(5); N(4)-N(5), 1.312(5). N(1)-Ru(1)-N(4), 177.66(14); N(1)-Ru(1)-N(6), 100.26(14); N(4)-Ru(1)-N(6), 78.02(14); N(1)-Ru(1)-N(3), 77.86(14); N(4)-Ru(1)-N(3), 100.59(14); N(6)-Ru(1)-N(3), 92.95(14); N(1)-Ru(1)-O(2), 101.88(13); N(4)-Ru(1)-O(2), 79.88(13); N(6)-Ru(1)-O(2), 157.83(13); N(3)-Ru(1)-O(2), 92.78(13); N(1)-Ru(1)-O(1), 80.11(13); N(4)-Ru(1)-O(1), 101.46(13); N(6)-Ru(1)-O(1), 91.88(13); N(3)-Ru(1)-O(1), 157.95(13); O(2)-Ru(1)-O(1), 90.80(12); C(1)-O(1)-Ru(1), 110.1(3); C(20)-O(2)-Ru(1), 110.6(3); N(2)-N(1)-C(14), 122.2(3); N(2)-N(1)-Ru(1), 121.1(3); C(14)-N(1)-Ru(1), 116.7(3); N(1)-N(2)-C(15), 110.4(3); C(19)-N(3)-C(15), 119.1(4); C(19)-N(3)-Ru(1), 129.5(3); C(15)-N(3)-Ru(1), 111.5(3); N(5)-N(4)-C(33), 123.2(4); N(5)-N(4)-Ru(1), 120.4(3); C(33)-N(4)-Ru(1), 116.4(3); N(4)-N(5)-C(34), 110.9(3); C(38)-N(6)-C(34), 118.5(4); C(38)-N(6)-Ru(1), 129.7(3); C(34)-N(6)-Ru(1), 111.7(3).

(and therefore no NH or OH stretches), it is important to note that to fit the microanalytical data, nearly four equivalents of methanol were required.

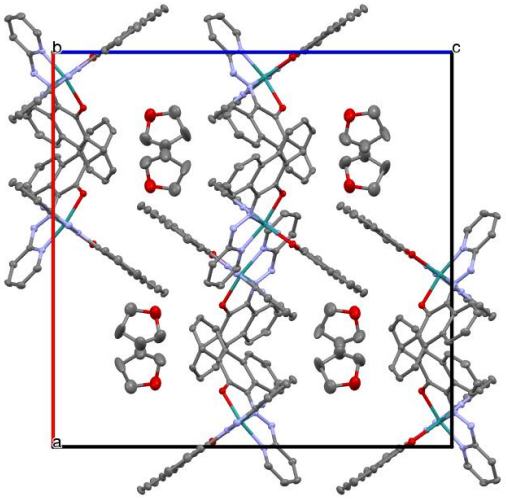

FIGURE 3.21: Packing diagram of 3.5 in the *bc* plane, hydrogen atoms excluded for clarity

A single crystal X-ray experiment(figure 3.20) revealed the structure of 3.5 to consist of a divalent ruthenium ion bound in the typical fashion for divalent complexes of 3.1 (through N_{pyr}, N_{azo}, and $O^{-}_{phenanthrol}$). This coordination motif allows 3.5 to possess a distorted octahedral geometry about the Ru(II) ion, and the coordinate bond length suggests that the Ru(II) ion is low spin and therefore complex 3.5 is diamagnetic. The bond lengths N(1)-N(2) and N(4)-N(5) are 1.308(5)$\mathring{A}$ and 1.312(5)$\mathring{A}$, are well within the expected length for an N=N double bond, and the O(1)-C(1) and O(2)-C(20) bonds at 1.305(5)$\mathring{A}$ and 1.292(5)$\mathring{A}$, are typical of a single C-O bonds. The packing diagram in the *bc* plane (figure 3.21) reveals significant pi interactions between phenanthrol rings in the crystal structure.

3.5.2 Electronic Properties

The room temperature UV-Visible spectrum of 3.5 in DMF is shown in figure 3.22. The spectrum features a maximum at 470nm ($\epsilon = 2x10^4 M^{-1}cm^{-1}$) which is typical of all complexes with ligand 3.1; this peak is attributed to $n-\pi^*$ transitions into the azo centered LUMO of the ligand[58]. The lower energy peaks at 560nm and 600nm, as well as the broad shoulder that extends to very low energy, likely contain MLCT, as well as ligand-to-metal charge transfer (LMCT) character. The ϵ values for 3.5 are the lowest recorded for complexes of ligand 3.1.

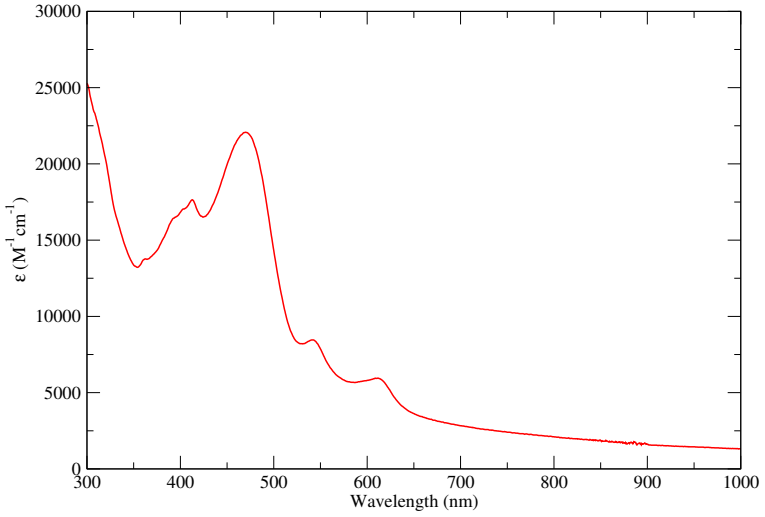

FIGURE 3.22: UV-Visible spectrum of 3.5: determined in DMF

The electrochemical data for 3.5 is placed in Appendix C (Figures C.1 and C.2 for CV and DPV respectively). The anodic voltammogram possesses the usual quasi reversible waves typical of divalent complexes with 3.1 at potentials of -0.5V, and -0.8V, which have been previously assigned [58] as reductions of the azo-moiety.

The quasi-reversible wave at 0.5V is assigned to the Ru(2+/3+) couple. Other higher potential cathodic waves likely belong to ligand centered oxidations.

3.6 $Cu(PAPL)_2 \cdot 0.3CH_2Cl_2$(3.6)

3.6.1 Structural Characterization

Coordination of 3.1 with $[Cu(CH_3CN]PF_6$ in DCM (scheme 3.4) produced a dark green solution. Complex 3.6 was obtained as green needle crystals by diffusion of diethyl ether into the reaction mixture.

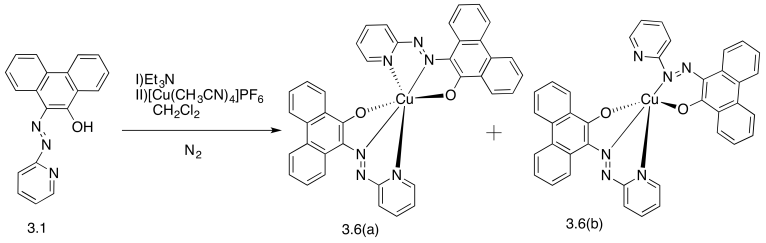

SCHEME 3.4: Synthesis of complex 3.6

The FT-IR spectrum obtained from 3.6 is typical of divalent complexes of 3.1, with no NH or OH absorptions, indicating that 3.1 is coordinated to the copper ion. The FT-IR spectrum also lacks any bands that could be associated with a PF_6 counter-anion, which offers further evidence of 3.6 being a typical divalent PAPL complex. Microanalytical data indicates that 3.6 is analytically pure with the addition of 0.3 equivalents of DCM.

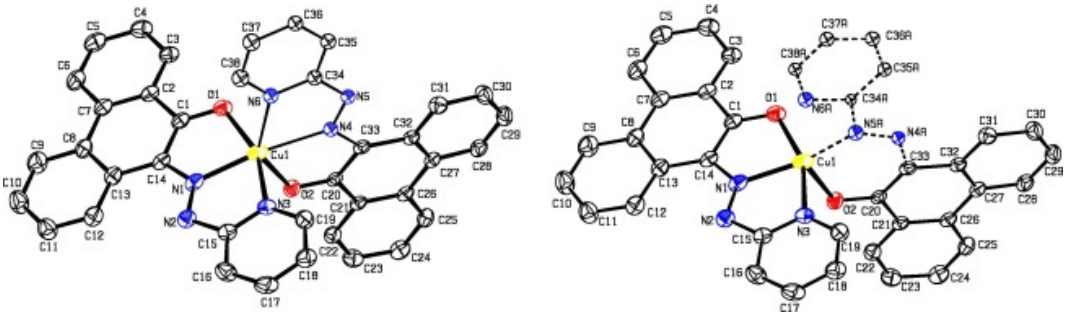

FIGURE 3.23: Displacement ellipsoid plot of 3.6: H atoms and solvent molecules omitted for clarity. Select bond lengths ($\AA$) and bond angles (^{o}) with standard uncertainties in brackets: Cu(1)–N(5A), 1.780(5); Cu(1)–N(1), 1.971(3); Cu(1)–O(1), 2.034(2); Cu(1)–N(3), 2.042(3); Cu(1)–O(2), 2.169(2); Cu(1)–N(4), 2.202(6); Cu(1)–N(6), 2.261(5); O(1)–C(1), 1.271(4); O(2)–C(20), 1.271(3); N(1)–N(2), 1.293(3); N(4)–N(5), 1.309(8); N(4A)–N(5A), 1.291(8); N(1)–C(14), 1.356(4); N(2)–C(15), 1.403(4); N(3)–C(19), 1.320(4); N(3)–C(15), 1.339(4); C(1)–C(14), 1.435(4); C(1)–C(2), 1.467(4). N(5A)–Cu(1)–N(1), 162.62(19); N(5A)–Cu(1)–O(1), 100.17(17); N(1)–Cu(1)–O(1), 80.34(9); N(5A)–Cu(1)–N(3), 99.46(17); N(1)–Cu(1)–N(3), 78.28(10); O(1)–Cu(1)–N(3), 158.46(10); N(5A)–Cu(1)–O(2), 94.64(18); N(1)–Cu(1)–O(2), 102.71(9); O(1)–Cu(1)–O(2), 92.29(8); N(3)–Cu(1)–O(2), 94.88(9); N(1)–Cu(1)–N(4), 171.58(16); O(1)–Cu(1)–N(4), 102.30(13); N(3)–Cu(1)–N(4), 99.23(14); O(2)–Cu(1)–N(4), 69.34(15); N(1)–Cu(1)–N(6), 116.7(2); O(1)–Cu(1)–N(6), 92.78(14); N(3)–Cu(1)–N(6), 94.47(15); O(2)–Cu(1)–N(6), 140.6(2); N(4)–Cu(1)–N(6), 71.4(2).

The divalent nature of complex 3.6 was supported by X-ray diffraction, with the structure shown shown in figure 3.23. Complex 3.6 has a unique structure with regard to complexes of ligand 3.1, as it has an interesting binding motif. There are two complexes in the crystal structure in a disorder ratio of 53:47 ratio (figure 3.23). Both complexes are neutral with Cu(II) ions bound to two 3.1 anions. The larger proportion is a typical six coordinate complex that features pseudo octahedral geometry around the copper ion. The minor component is of particular interest, as it is five coordinate around the Cu(II) ion in a distorted square pyramidal geometry. In the minor component the coordination sphere consists of

one equivalent of 3.1 with donor atoms N_{azo}, N_{pyr}, and $O^{-}_{phenanthrol}$, which is the general binding motif. The other equivalent of 3.1 is bound in a bidentate fashion through $O^{-}_{phenanthrol}$, and the non-typical N_{azo} atom. The pyridine ring in this complex is located farther away from the copper ion and is likely non-coordinating. This is the first example of PAPL binding in a bidentate fashion. The coordinate bond from the N_{azo} atom in the bidentate minor component is extremely short at 1.780(5)$\mathring{A}$. In both complexes the N=N bond distances are in the typical range of 1.291(8)-1.309(8)$\mathring{A}$. The molecular packing diagram in the *ab* plane (figure 3.24) shows the close $\pi - \pi$ contacts in 3.6.

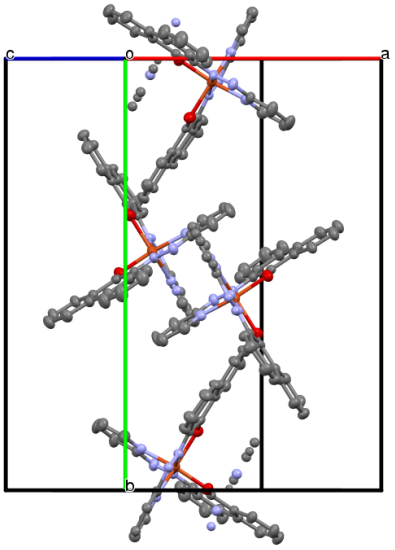

FIGURE 3.24: Packing diagram of 3.6 in the *ab* plane, hydrogen atoms excluded for clarity.

3.6.2 Magnetic Properties

The solid state magnetic susceptibility for 3.6 was probed over a temperature range of 2-300K using a SQUID magnetometer. The results are shown as a $\chi_m T vs T$ plot in figure 3.25. At 300K the value for $\chi_m T$ is $0.42 cm^3 K mol^{-1}$, and is similar to the spin only predicted value ($g = 2$) for a $S = 1/2$ molecule ($\chi_m T = 0.375 cm^3 K mol^{-1}$). The magnetic profile has a slight temperature dependence, with $\chi_m T$ increasing with decreasing temperature, which is likely due to spin-orbit coupling. The hump in the data between 40K and 50K is likely due to paramagnetic oxygen being trapped in the sample capsule.

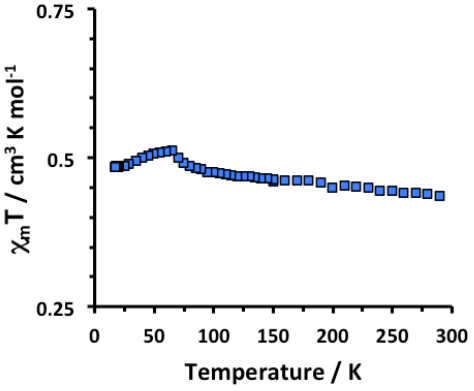

FIGURE 3.25: Magnetic susceptibility profile for 3.6 over a temperature range of 2K to 300K (field: $2000 Oe$).

Though structural studies indicate that there are close $\pi - \pi$ contacts in the molecular packing of 3.6, the SQUID data indicates that no low temperature intermolecular interactions are present. This lack of deviation is attributed to the absence of spin density de-localization from the copper atoms to coordinated 3.1.

EPR was also performed on a crystal sample of 3.6, as well as in a frozen DCM solution (both at 100K). The crystal spectrum is axial(figure 3.26), while the frozen solution (figure 3.27) shows broad shoulders; these features are likely due to poorly resolved copper hyperfine coupling.

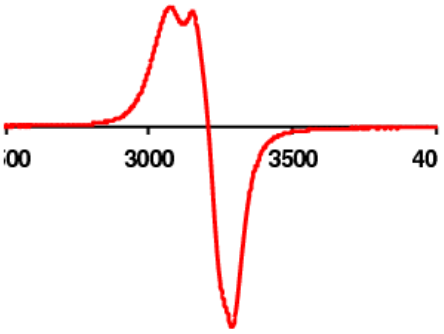

FIGURE 3.26: EPR of a powder sample of 3.6 at 100K.

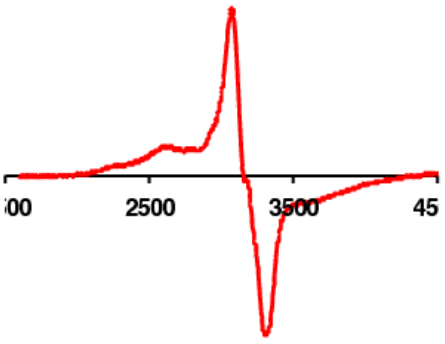

FIGURE 3.27: EPR of a frozen DCM solution of 3.6 at 100K.

3.6.3 Electronic Properties

The UV-Visible spectrum of 3.6 in DCM is shown in figure 3.28. There is a very intense absorption which has a maximum molar extinction value of approximately $5x10^4 M^{-1}cm^{-1}$ over the range of 500-600nm. TD-DFT calculations allow for the assignment of these absorptions as a mixture of ILCT, MLCT, and LMCT bands between the frontier molecular orbitals of 3.6.

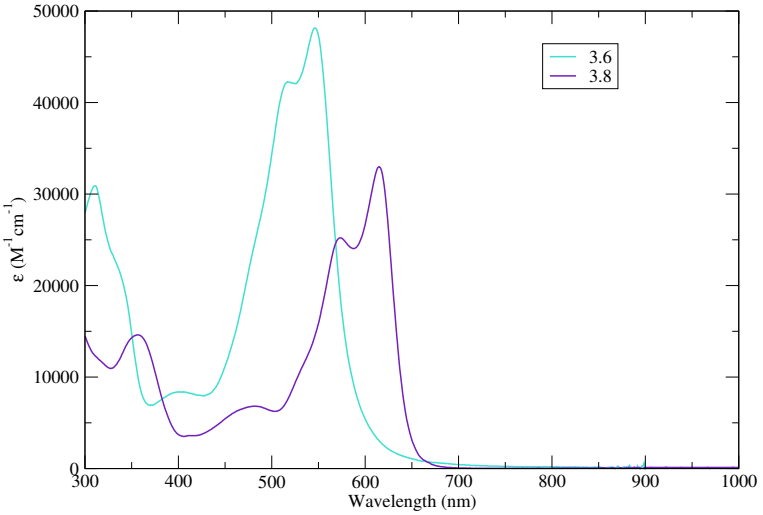

FIGURE 3.28: UV-Visible spectrum of 3.6 and 3.8: 3.6 performed in DCM and 3.8 performed in chloroform

The electrochemical data is summarized in table 3.1 while the CV and DPVs are placed in Appendix C (C.7 and C.8). The spectrum, though very busy (due to decomposition in the sample), has several peaks that can be assigned. On the anodic side the waves at 0.8V, and 1.3V, are assigned as oxidation of the PAPL ligand, and the wave at 0.2V, which is only detectable by DPV is unassigned. On the cathodic side the wave at -0.6V is assigned to the $Cu^{2+/+}$ couple while the

irreversible high potential waves at -1.4V and -1.7V, are assigned as the reduction of the azo moiety in the ligand.

3.7 $[Fe(PAPL)_2]I_3 \cdot 1.55CH_2Cl_2$(3.7)

3.7.1 Structural Characterization

Complex 3.7 is obtained as a black microcrystalline powder that precipitates out of the DCM reaction mixture (scheme 3.5). Powder 3.7 is analytically pure after fitting the microanalytical data with $1.5 mols$ of DCM. However, crystal growth attempts of 3.7 were all ineffective, as the complex decomposes back to $Fe(PAPL)_2$ in solution, as well as slowly over time in the solid state, which is supported by UV-Vis (see section 3.7.3) and X-ray diffraction. Other spectroscopic methods were used to structurally characterize 3.7.

The FT-IR spectrum of 3.7 is typical of complexes of 3.1. There are no peaks beyond the fingerprint region indicating that 3.1 is coordinated to the metal ion in the complex (no NH or OH stretches).

ESI mass spectrometry was performed in both positive ion (figure 3.29) and negative ion mode (figure 3.29), to determine the cation, and anion of this salt. In positive ion mode a peak at $652.1 m/z$ is indicative of a $Fe(PAPL)_2^+$ cation. In negative ion mode there is a dominant peak in the spectrum at $380.5 m/z$ that corresponds to the I_3^- anion.

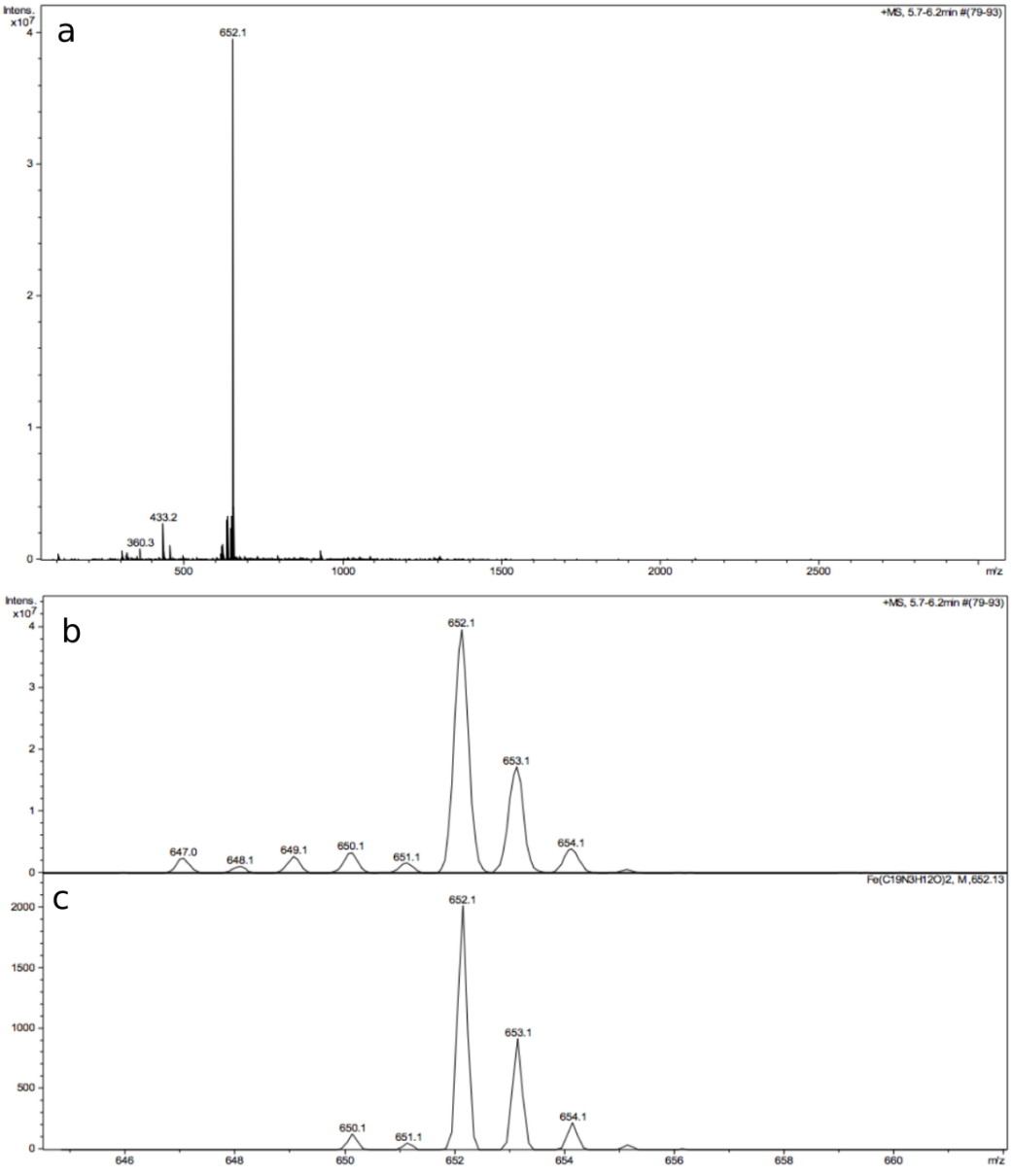

FIGURE 3.29: a:ESI^+ mass spectrum for 3.7 b: Observed isotope pattern c: simulated isotope pattern for 3.7 corresponding to a $[Fe(PAPL)_2]^+$ cation

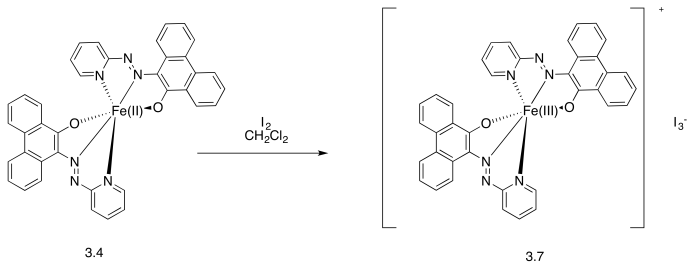

SCHEME 3.5: Synthesis of complex 3.7

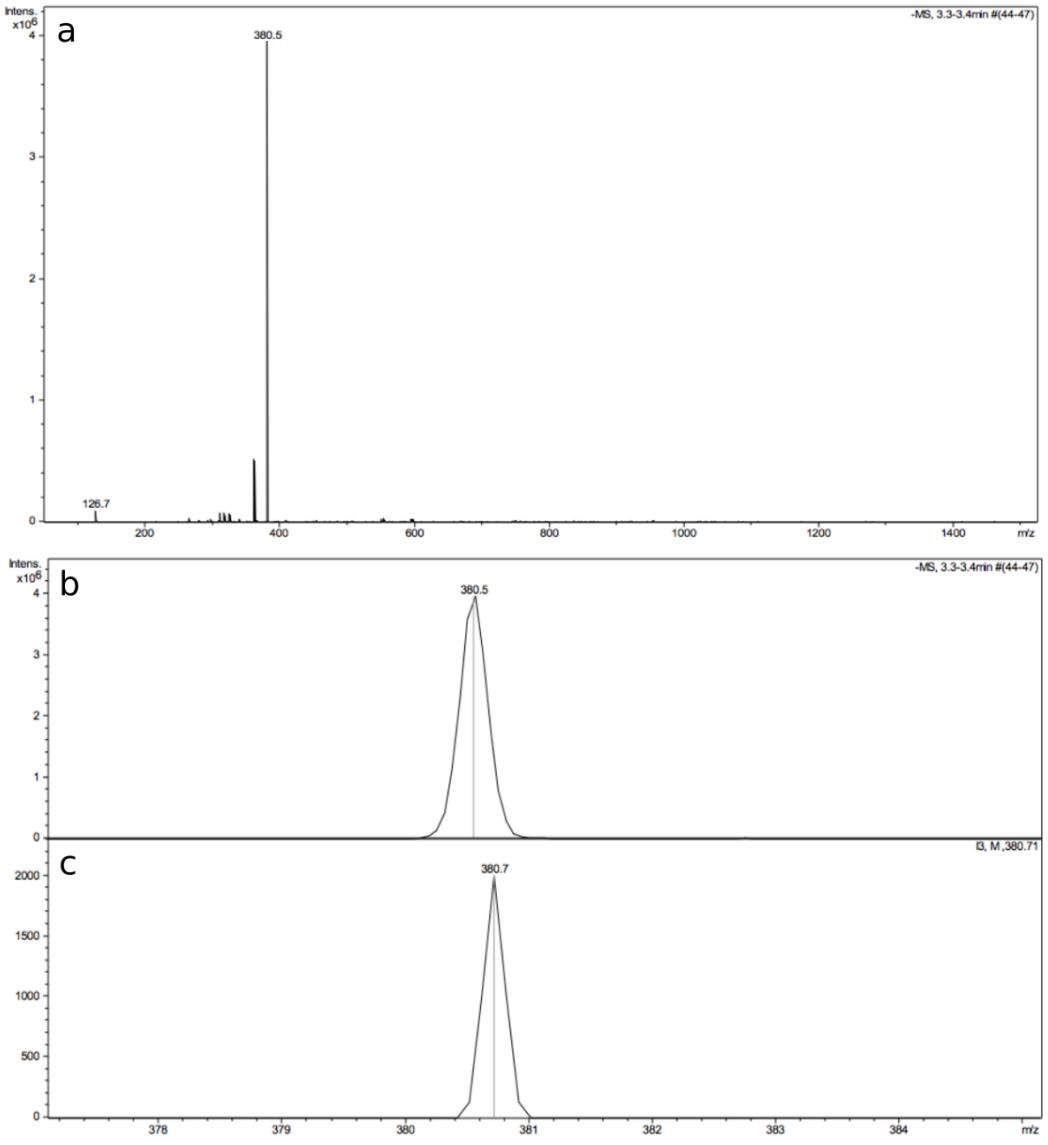

FIGURE 3.30: a:ESI^- mass spectrum for 3.7 b: Observed isotope pattern c: simulated isotope pattern(bottom) for 3.7 corresponding to a I_3^- anion

Single crystals produced by diffusion of water into a DMF solution of 3.7 produced an additional polymorph of the divalent $Fe(PAPL)_2$ complex (figure A.3).

3.7.2 Magnetic Properties

The magnetic properties of the 3.7 were investigated by SQUID magnetometry (figure 3.31). Over the temperature range (5-325K) 3.7 is weakly paramagnetic, with only a slight temperature dependence on $\chi_m T$. At 325K $\chi_m T$ is $0.33 cm^3 K mol^{-1}$, a value which is slightly less then the expected value for one unpaired electron. As 3.7 is produced by the oxidation of 3.4 there are two interpretations for this behaviour. The first is a metal centered oxidation, producing a low spin ($S = 1/2$) Fe(III) complex. Alternatively the oxidation reaction was ligand centered, in which one of the PAPL ligands is oxidized, producing a neutral phenoxyl radical, and the Fe(II) ion remains low spin.

EPR spectroscopy was carried out in the solid state at 80K (figure 3.32) and 300K. At both temperatures a rhombic spectrum is observed, which is expected for a low spin Fe(III) molecule in a low symmetry environment[84], which confirms that the oxidation was metal centered, producing low spin Fe(III).

Variable temperature Mössbauer spectroscopy was also performed on complex 3.7 (figure 3.33 and table 3.5). The isomer shift observed for the sample was smaller than those observed for 3.3 and 3.4, which is indicative of a higher oxidation state for the iron ion in 3.7. The large quadrupole splitting supports the low

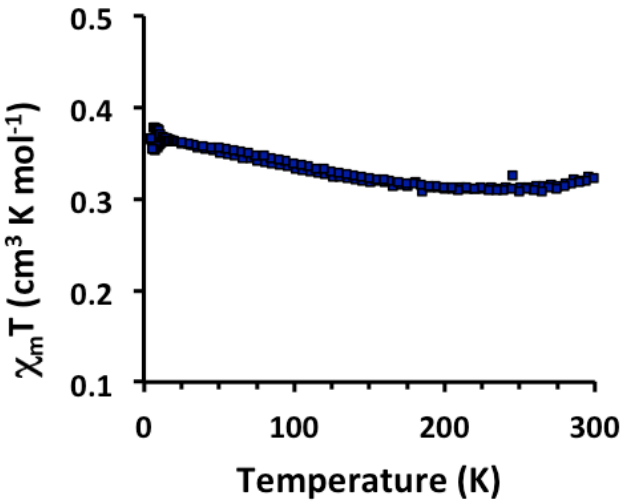

FIGURE 3.31: $\chi_m TvsT$ plot for 3.7 at a external field of $5000Oe$.

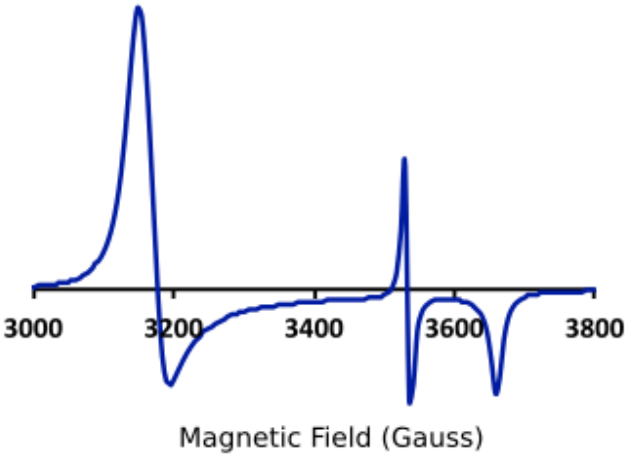

FIGURE 3.32: Solid state EPR for 3.7 at 80K.

Temperature	δ (mm/s)	ΔE_Q (mm/s)	Γ (mm/s)
6K	0.102(2)	3.087(4)	0.372(6)
150K	0.080(4)	3.071(8)	0.38(1)
294K	0.027(7)	3.21(1)	0.42(2)

TABLE 3.5: Mössbauer data for 3.7

spin ($S = 1/2$) nature of the Fe(III) ion[85], which was observed by EPR and magnetometry.

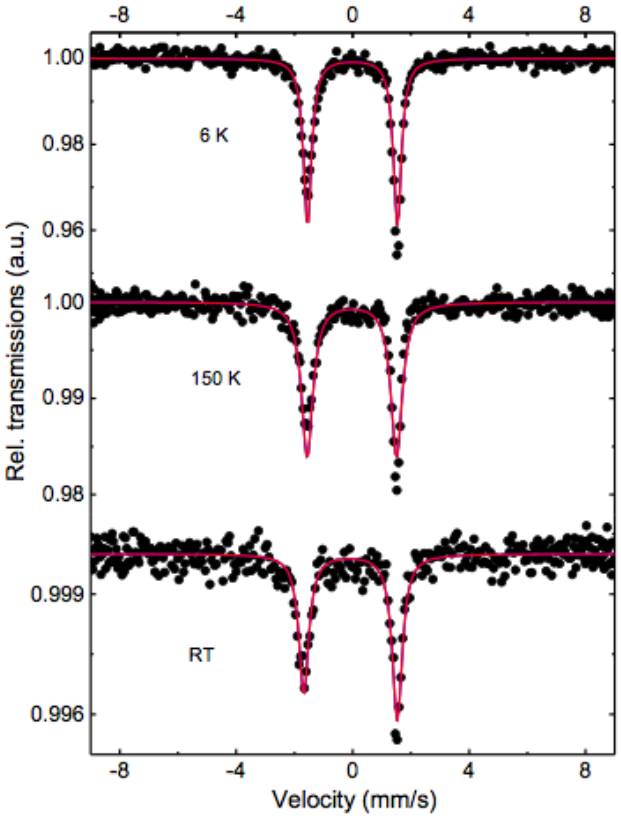

FIGURE 3.33: Variable temperature Mössbauer spectra performed on microcrystalline powder of 3.7 (zero field).

3.7.3 Electronic Properties

The UV-Visible spectrum of 3.7 in DMF (3.16) is very similar to 3.4 but it contains an extra, intense absorption band at 365nm. This additional band is found commonly in I_3^- salts, and disappears over time as 3.7 decomposes to $Fe(PAPL)_2$.

The poor solubility of 3.7 inhibited the collection of adequate electrochemical data, with the spectra obtained placed in the appendices (Figures C.3, and C.4.).

3.7.4 Computational Chemistry

DFT calculations were carried out on $[Fe(PAPL)_2]^+$ in the doublet ($S = 1/2$) state. The geometry was optimized starting from the atomic coordinates generated from X-ray diffraction on 3.4. The coordinate bond distances were calculated to be similar to that of the 3.4, with the exception of the Fe-O bond, which is shorter in the calculated structure; a property anticipated for the ferric cation. The calculated azo bond distance is shorter than the same bond (both experimentally and computationally) in 3.4, which supports the reduction in π donation from the metal to the ligand upon oxidation. The spin-density distribution (figure 3.35) for $[Fe(PAPL)_2]^+$ is mostly confined to the metal, which supports the experimental result from EPR spectroscopy on 3.7. The composition of the HOMO and LUMO orbitals for 3.7 is presented in figure 3.34.

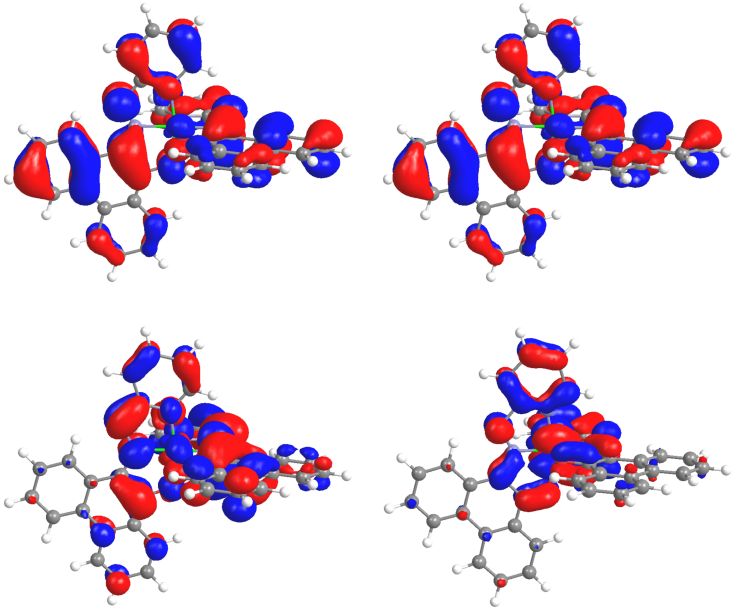

FIGURE 3.34: $\alpha-$HOMO, $\beta-$HOMO, $\alpha-$LUMO and $\beta-$LUMO calculated for $[Fe(PAPL)_2]^+$ in the doublet state calculated at the B3LYP/def2-TZVP level of theory (isovalue 0.02).

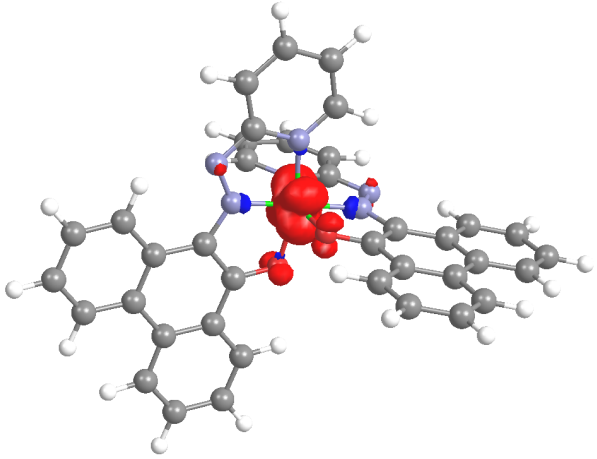

FIGURE 3.35: Calculated spin density distribution for doublet $[Fe(PAPL)_2]^+$ calculated at the B3LYP/def2-TZVP level of theory (isovalue 0.004).

The absorbance spectrum of the doublet $[Fe(PAPL)_2]^+$ in chloroform was calculated using TD-DFT (figure 3.36). In general, this spectrum is similar to the electronic spectrum of $Fe(PAPL)_2$, which agrees with the experimental observation. There is a lower energy peak calculated at 806nm with is predominantly of LMCT character, while peaks at 547 and 551nm are ligand centered transitions.

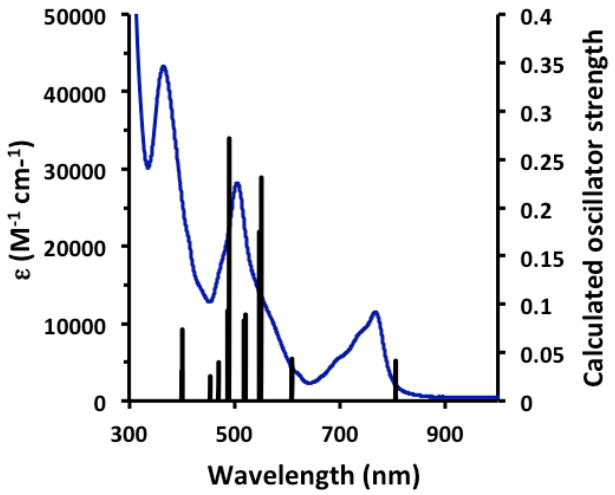

FIGURE 3.36: UV-visible spectrum of 3.4(blue trace) in chloroform and calculated transitions for $[Fe(PAPL)_2]^+$ at the B3LYP/def2-TZVP level of theory in chloroform.

3.8 $[(\mathbf{PAPL})\mathbf{VO}]_2\mu - \mathbf{O_2} \cdot \mathbf{0.75CH_2Cl_2}(\mathbf{3.8})$

3.8.1 Structural Characterization

Complex 3.8 was obtained as a green powder, as a precipitate directly from the chloroform/methanol reaction solution, as according to scheme 3.6. Complex 3.8

was purified by crystallization, producing small green plate single crystals by diffusion of diethyl ether into a THF solution of 3.8.

The FT-IR spectrum lacks any absorptions to indicate the presence of a counter-ion. There are also no OH or NH stretches that would be representative of the free ligand. The crystals are impure by analytical analysis, and could not be fit with solvent.

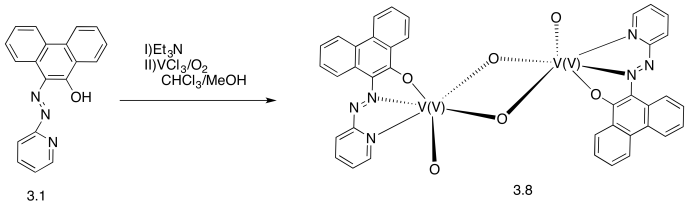

SCHEME 3.6: Synthesis of compound 3.8

Single crystal X-ray diffraction reveals 3.8 to be a di-oxo bridged dimer with two vanadium(V) ions. Each V(V) ion is coordinated to an anion of 3.1 in the typical binding fashion (through the $O^-_{phenanthrol}$, $N_{pyridine}$ and and N_{azo} atoms). The other 3 coordination sites are occupied by O, two of which bridge the vanadium ions, and one which is terminal. The azo bond of the ligand is of typical length (1.289(3)$\mathring{A}$) for a N=N double bond. In addition the $O_{phenanthrol}$ bond length (1.294(3)$\mathring{A}$) is typical for a C-O single bond. Charge balance conclusively determines the oxidation state of the vanadium ions at +5 so 3.8 is expected to be diamagnetic.

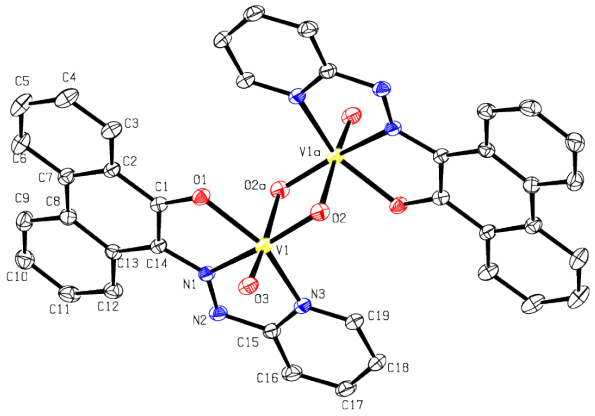

FIGURE 3.37: Displacement ellipsoid plot of 3.8: H atoms omitted for clarity. Select bond lengths ($\AA$) and bond angles (^{o}) with standard uncertainties in brackets:V(1)-O(3), 1.6033(18); V(1)-O(2), 1.6759(18); V(1)-O(1), 1.9689(18); V(1)-N(3), 2.100(2); V(1)-N(1), 2.170(2); V(1)-O(2a), 2.2884(18); V(1)-V(1a), 3.1060(9); O(1)-C(1), 1.294(3); O(2)-V(1a), 2.2884(18);N(1)-N(2), 1.289(3). O(3)-V(1)-O(2), 106.35(9); O(3)-V(1)-O(1), 96.41(9); O(2)-V(1)-O(1), 108.02(8); O(3)-V(1)-N(3), 95.42(9); O(2)-V(1)-N(3), 97.96(9); O(1)-V(1)-N(3), 146.98(8); O(3)-V(1)-N(1), 100.00(9); O(2)-V(1)-N(1), 152.60(8); O(1)-V(1)-N(1), 75.80(7); N(3)-V(1)-N(1), 71.83(8); O(3)-V(1)-O(2a),175.59(9); O(2)-V(1)-O(2a), 77.94(8); O(1)-V(1)-O(2a), 81.09(7); N(3)-V(1)-O(2a), 84.90(7); N(1)-V(1)-O(2a), 75.89(7); O(3)-V(1)-V(1a), 152.43(8); O(2)-V(1)-V(1a), 46.10(6); O(1)-V(1)-V(1a), 93.02(6); N(3)-V(1)-V(1a), 90.52(6); N(1)-V(1)-V(1a), 107.42(6); O(2a)-V(1)-V(1a), 31.85(4); C(1)-O(1)-V(1), 118.53(15); V(1)-O(2)-V(1a), 102.06(8)

3.8.2 Electronic Properties

The UV-Visible spectrum of 3.8 (figure 3.28) is very similar to that observed for the divalent copper complex 3.6, except that it is red shifted by $\approx 200nm$. The maximum absorption of $3x10^4 M^{-1}cm^{-1}$ occurs at 640nm overlapping with the absorption band at 580nm ($\epsilon \approx 2x10^4 M^{-1}cm^{-1}$), this band is likely mainly of ILCT character with a small contribution of LMCT.

The electrochemical data of 3.8 (Figures C.5 and C.6) consists of five cathodic irreversible waves at -0.3V, -0.4V, -0.9V, -1.4V. The high intensity wave at -0.9V is likely that of the reduction of the V(5+/4+) couple.

3.9 Reduction attempts

Several attempts were made to reduce either free 3.1 or the divalent transition metal complexes of 3.1. With regards to the free ligand sodium reduction was attempted with both sodium napthalenide or sodium 18-crown-6 in THF. The sodium 18-crown-6 reduction was successful in generating a certain amount of reduced 3.1. The EPR spectrum of this product is shown in figure 3.38. The spectrum shows a 3-peak hyperfine coupling with superhyperfine coupling further splitting each peak. is intact as the hyperfine splitting for a radical centred over an N-N bond is $2NI + 1 = 2(2)1 + 1 = 5$ this is curious as the hyperfine coupling suggests most of the SOMO is located over one of the azo nitrogens with superhyperfine coupling from the other nitrogen. There is further coupling with neighbouring atoms causing further splitting in the spectrum. However, simulations were not performed to confirm this observation. The reduced product was insoluble, red in colour, and decomposed rapidly in both air and solution.

M(0) sources were shown in literature [50] to produce complexes with reduced azo-aromatic ligands. Attempts were made with $Ni(COD)_2$, $Fe(CO)_5$, $Co_2(CO)_8$, $W(CO)_6$, and $Cr(CO)_6$, as well as reducing copper metal $[Cu(CH_3CN)_4]PF_6$.

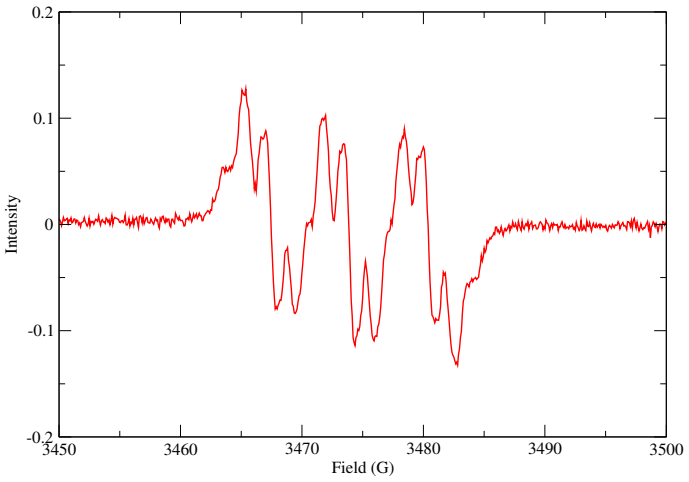

FIGURE 3.38: EPR spectrum of 3.1 in toluene reduced by sodium 18-c-6

The results of the the M(O) coordination either produced a divalent metal complex (Ni, Fe, Cu, Co and Zn) or produced a mixture that could not be purified (Cr, and W) with no evidence of reduction occurring.

Finally, reduction attempts were made on the previously synthesized divalent complexes. Reduction was attempted with cobaltocene, bis(pentametylcyclopentadienyl)cobalt(II), sodium napthalenide, and sodium 18-c-6. However no conclusive data was collected to show reduction of the divalent complexes.

Chapter 4

Lanthanide ion complexes of 1-(2-pyridylazo)-2-phenanthrol (Ln(III)=Gd, Tb, and Dy)

4.1 Introduction

Three complexes were synthesized by coordination of 3.1 to lanthanide ions. Lanthanide complexes with ligand 3.1 were synthesized with an interest of determining the interplay between the redox active behaviour, and dye like properties of azo-aromatic ligands, with the luminescent properties that are typical in lanthanide complexes. The combination of which is scarce in literature precedent[60].

4.2 Structural Characterization of 4.1-4.3

Complexes 4.1 to 4.3 are easily prepared as pure microcrystalline precipitates that are a royal purple colour, by combining a chloroform solution of 3.1 with a methanol solution of the appropriate lanthanide nitrate salt(scheme 4.1). Many attempts to obtain X-ray quality single crystals from the microcrystalline powder of these complexes (including attempts at slow evaporation, layering, and vapour diffusion) were unsuccessful, often producing either microcrystalline clusters, or microspherical particles. Using other characterization methods has allowed for an informed discussion on the general structural features of these molecules.

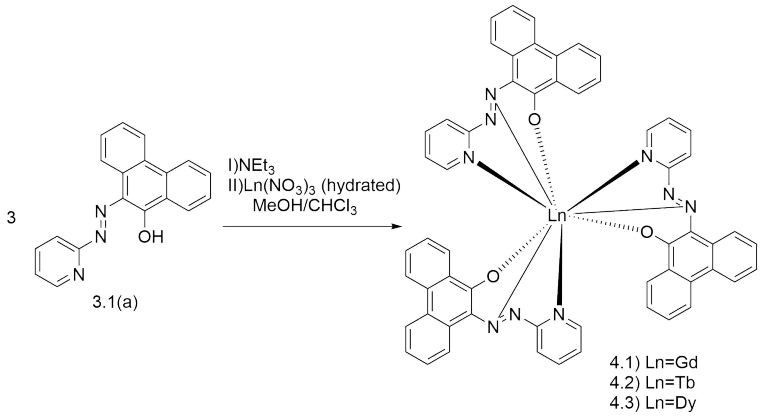

SCHEME 4.1: Synthesis of lanthanide PAPL complexes.

The ESI^+ mass spectrometry data in all cases show that the lanthanide complexes have the formula $Ln(PAPL)_3$ (figures 4.1, A.4, A.5), with dominant peaks in all cases that correspond to $Ln(PAPL)_3H^+$ with isotope patterns that match the theoretical patterns generated. In support of the structural assignment, the

combustion analysis performed on the samples for complexes 4.1 and 4.3 are analytically pure without the addition of solvent for this formulation, and in the case of 4.2 requires only 0.4 equivalents of chloroform to fit.

The FT-IR spectra shown in figure 4.2 for complexes 4.1-4.3 are nearly identical. The spectra lacks any stretches that would belong to nitrate which suggests 4.1-4.3 are neutral complexes. Compound 3.1 appears coordinated to the metal ion as there are no OH or NH stretches in the spectra to indicate the free ligand. The UV-Visible spectra (Figure 4.4) for complexes 4.1-4.3 are also nearly identical with only minor differences in intensities throughout the spectra, a property which allows for the conclusion that complexes 4.1-4.3 are iso-structural. It is likely that all three of the complexes posses a coordination sphere containing nine coordinate bonds from three anions of 3.1. As the lanthanide ion for each complex is trivalent the resulting complexes are neutral by charge balance. Coordination of this type would likely be through the N_{py}, N_{azo}, and $O^{-}_{phenanthrol}$ donor sites, similar to that of the majority of PAPL transition metal complexes[58][59][82]. In this proposed coordination motif, complexes 4.1-4.3 likely feature a tricapped trigonal prismatic geometry, which is observed for other lanthanide complexes with NNO ligands[86].

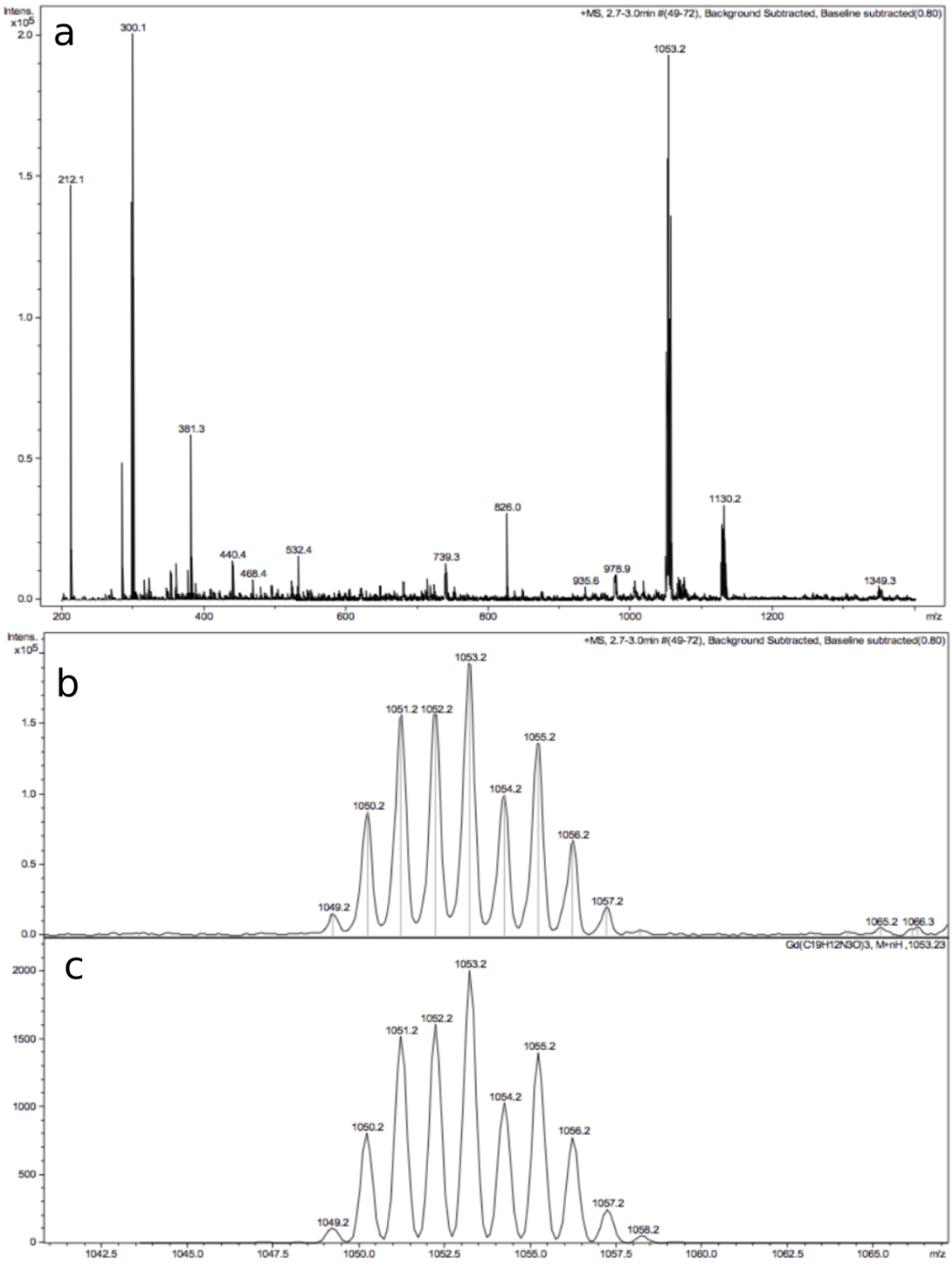

FIGURE 4.1: a: Mass spectra for 4.1 b: Observed isotope pattern for 4.1 c: Simulated isotope pattern for 4.1

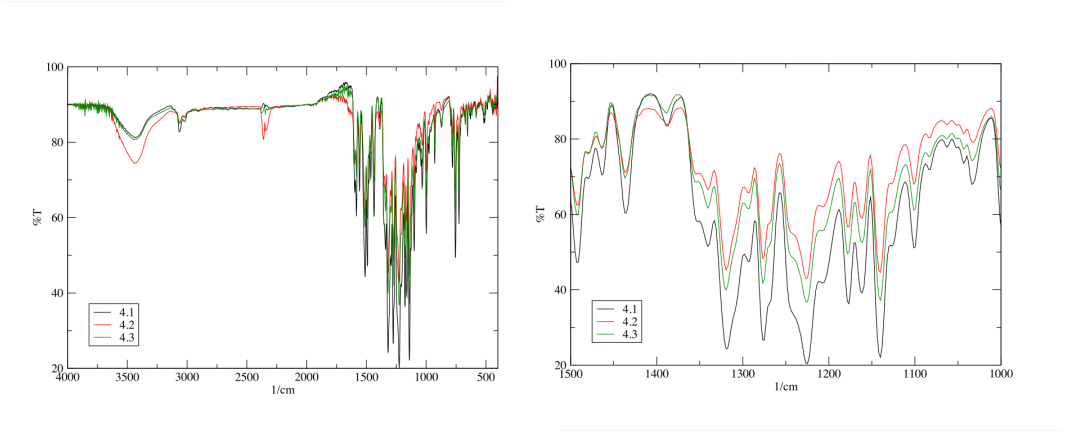

FIGURE 4.2: FT-IR spectra of 4.1-4.3: Left: FT-IR spectra over the range of 400 to 4000cm^{-1} Right: FT-IR spectra in the region of 500 to 1000cm^{-1} to highlight the iso-structural nature of the spectra for 4.1-4.3.

4.3 Variable Temperature Magnetic Properties of 4.1-4.3

Solid state variable temperature DC magnetic susceptibility measurements were performed on complexes 4.1, 4.2, and 4.3, and the data is shown as a $\chi_m T vs T$ plot in figure 4.3. The data was taken over a range of 2-300K at an external field of 0.2T on a Quantum Design Vibrating Sample Magnetometer(VSM). The data collected is consistent in each case with single-ion type magnetism for Gd(III), Dy(III), and Tb(III) free ions, with term symbols $^8S_{7/2}$, $^6H_{15/2}$, and $^7F_6$, respectively. At 300K, $\chi_m T$ is the typical value for single ion lanthanide systems with values of 7.67, 14.0, and 11.0$cm^3 K mol^{-1}$ for each respective molecule, while at low temperatures there is a slight deviation in the $\chi_m T$ values for 4.2, and 4.3. This deviation is attributed to the thermal depopulation of the Stark sublevels in this temperature range. Also

of note is a variance in $\chi_m T$ values for 4.2, and 4.3 between cooling and warming. As magnetic cooperation is not expected for complexes 4.1-4.3, it is likely due to the sample shifting inside the gel caps.

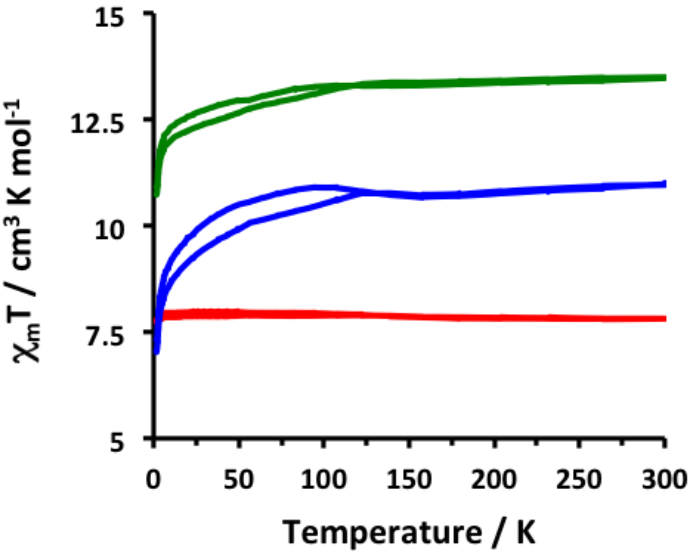

FIGURE 4.3: $\chi TvsT$ plots for 4.1(red trace), 4.2(blue trace), and 4.3(green trace) in an external field of 0.2T

Preliminary AC magnetic susceptibility measurements were performed on complexes 4.2 and 4.3 to investigate the dynamic magnetic properties typical of lanthanide single ion magnets containing either Tb[87] or Dy[88]. However, the preliminary experiments taken at zero external field, or in an external magnetic field showed no peaks in the out of phase magnetic susceptibility, and therefore these complexes are not single ion magnets.

4.4 Electronic Properties

The UV-Visible profile of 4.1-4.3 as well as uncoordinated 3.1 are shown in figure 4.4. For the ligand the absorptions between 225nm and 350nm in the near IR region are assigned as $\pi - \pi^*$ transitions. This peak is observed in conjunction with another absorption peak in the visible region in the range of 350-525nm with a high energy shoulder in the visible region that is assigned as $n - \pi^*$ transitions belonging to the azo moiety.

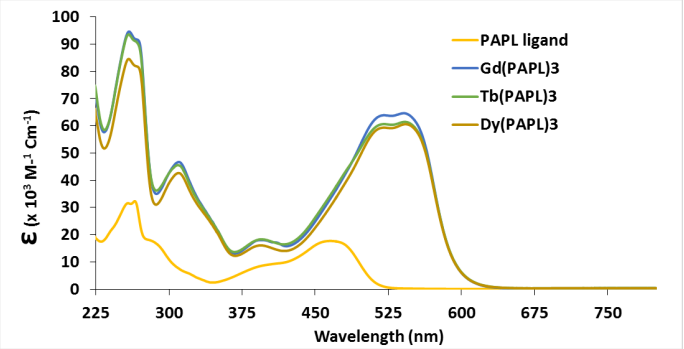

FIGURE 4.4: UV-Visible spectra of 3.1, 4.1, 4.2, and 4.3: Performed in DCM at room temperature over an extended range.

The lanthanide complexes all feature nearly the same UV-Visible spectra, with only minor differences in the intensities observed over the investigated range. Similar to uncoordinated 3.1, there are $\pi - \pi^*$ transitions in the 225-350nm region. In addition there are two overlapping broad bands with shoulders in the 375-600nm region that are assigned as ILCT bands. The ILCT bands are red-shifted when compared to the free ligand, which is in agreement with the literature precedent for other lanthanide complexes with an azo moiety[60], as well as in the transition

metal complexes with the PAPL ligand[58][59][82][83]. This red-shift is generated during coordination with the lanthanide ions, and occurs due to coordination with PAPL in the enolate form. The enolate form of PAPL is the only tautomer to contain the azo moiety, which exists with extended conjugation from the aromatic rings. This gives rise to a low lying azo centred π^* orbital in these complexes, and results in the intense colours seen during coordination.

The electrochemical properties of the lanthanide complexes were investigated by CV and DPV, and the data collected is summarized in table 4.1. Complexes 4.1, 4.2 and 4.3 all share a very similar electrochemical profile, therefore complex 4.1(Gd) (Figures 4.5, and 4.6) has been chosen to highlight the various electrochemical properties (while the electrochemical data for 4.2 and 4.3 has been placed in Appendix C: figures C.9 and C.10). Over the anodic range there are two irreversible waves detected at 0.9V and 1.2V(with reference to Ag/AgCl), which are assigned as ligand oxidations similar to what is seen in the $M(PAPL)_2$ complexes[58][59][82]. At cathodic potentials there are two quasi-reversible waves at -1.2V and -1.5V, which are assigned as ligand centred reductions of the azo moiety, and a irreversible wave at -1.8V remains unassigned, though it is likely either the reduction of the final ligand, further reduction of the ligand, or the reduction of the lanthanide ions.

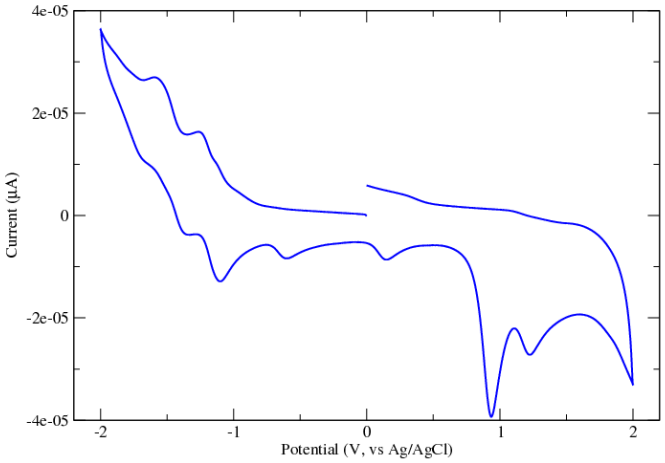

FIGURE 4.5: CV of 4.1 in DCM over the range of -2V to 2V at a scan rate of 200mV/s

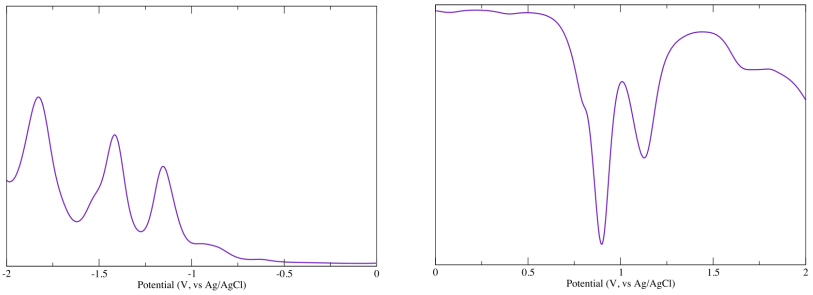

FIGURE 4.6: Left: Cathodic DPV of 4.1. Right: Anodic DPV of 4.1. Performed in DCM at a scan rate of 25mV/s

Complex	$E_{1/2}$ anodic (V vs Ag/AgCl)	$E_{1/2}$ cathodic (V vs Ag/AgCl)
4.1	0.9(irr), 1.2(irr)	-1.2(qr), -1.5(qr), -1.8(irr)
4.2	1.0(irr) 1.2(irr)	-1.2(qr), -1.5(qr), -1.9(irr)
4.3	0.9(irr), 1.2(irr)	-1.2(qr), -1.4(qr)

TABLE 4.1: Electrochemical data for 4.1-4.3

4.5 Emissive Properties

The emissive properties of 3.1 and 4.1-4.3 were investigated and interpreted by the group of Professor Garry Hannon at the University of Montreal. The emission spectrum of 3.1 in DCM was obtained while screening multiple wavelengths (figures D.1, D.2, D.3) and the maximum excitation wavelength of 257nm was found; the spectrum is shown in figure 4.7. The free ligand is not excitable by irradiation into the lowest energy absorption band which is similar to previously described azo-aromatic ligands[89], and it was suggested that this is due to the generation of a very polar excited state which relaxes in a non-radiative fashion, and is associated with photochemical isomerization. Radiative excitation does occur at room temperatures with multiple excitations at lower wavelengths (figures 4.7, and D.1-D.3). This emission profile has a higher energy band (in 325nm to 425nm range) with vibronic structure of similar energy (λ_{max}=365, 384, 419, and 442 nm) and a lower energy band (in the range 425-600nm) which also features vibronic structure of similar energy (λ_{max}=490, 517, and 560nm). At 77K the spectrum consists of a broad band without vibronic structure and has a maximum at λ_{max}=645nm. The

complexity of this interesting emission profile is due to a combination of multiple functionalities in the structure (of both tautomeric forms) including azoaryl, phenanthrol, and pyridyl moieties, which each can display a specific characteristic behaviour upon excitation. Comparison to similar systems allows for the conclusion that the high energy band is a locally excited state in addition to radiative relaxation of higher S and T, while the lower energy band is assigned as intermolecular charge transfer states. The emission profile is that of radiation from a triplet state, which is verified by the following Gd complex.

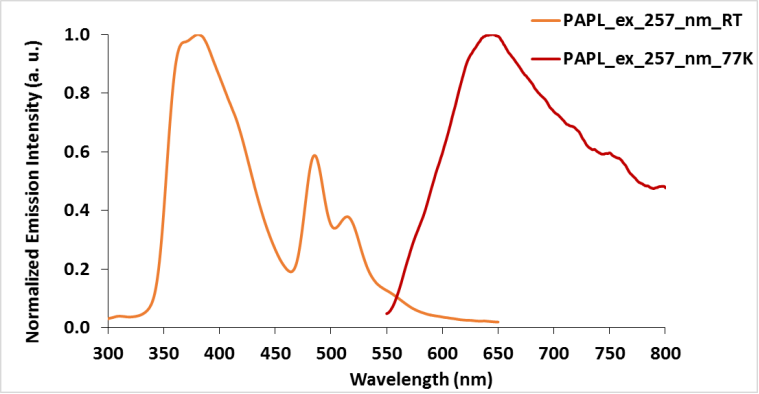

FIGURE 4.7: Emission profile of PAPL: Performed in DCM at room temperature (yellow trace λ_{max} = 365(sh), 384, 419(sh), 490(sh), 517, 544, and 560(sh)nm); and at 77K (red trace, λ_{max} = 645 nm) (λ_{exc}= 257 nm; concentration $1x10^{-5}M$)

The emission spectra of 4.1 at both room temperature and 77K is shown in figure 4.8, while the screening runs are shown in figure D.4 and the emission excitation profile in D.5. In Gd(III) complexes, the excited energy level of the Gd(III) ion has high enough energy as to inhibit transfer of energy from the triplet state of the ligand, to the metal state; and the heavy ion effect generally promotes the phosphorescence of the ligand. This makes Gd complexes ideal for estimating the energy

of the triplet states of ligands[90], and as such for PAPL ligand the value of the triplet energy was determined using the 77K spectrum to be $17000cm^{-1}/590nm$.

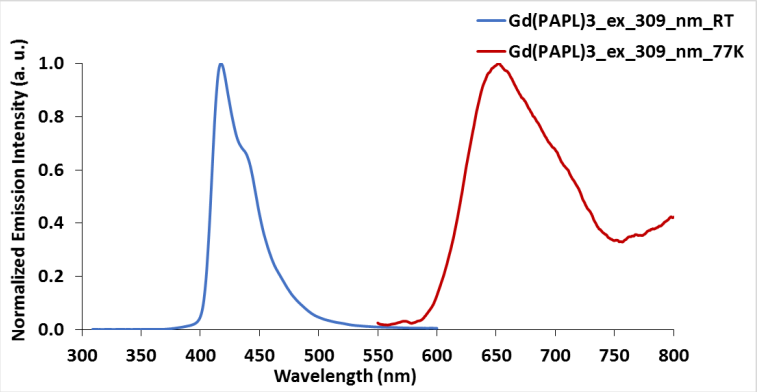

FIGURE 4.8: Emission profile of complex 4.1: Performed in DCM at room temperature (blue trace, λ_{max} = 419nm) and at 77K (red trace, λ_{max}=652nm) (λ_{exc} = 309 nm) (concentration $4x10^{-5}M$)

Similar to the free ligand case irradiation into the lowest energy band does not result in emission in the lanthanide PAPL complexes. For complex 4.1 irradiation into the high energy band at room temperature (figure 4.8) causes it to exhibit ligand based luminescence. The energy state the molecule is excited to has an estimated energy of $24200cm^{-1}$, and there are several possible explanations. The first is that this state is a higher energy triplet level of the ligand, the second is that this is a mixing between a higher singlet and a higher triplet energy level (such as incomplete intersystem crossing at room temperature), or third this is another type of excited state such as intramolecular charge transfer, which is capable of relaxing in a radiative fashion.

The emission profile for complexes 4.2 and 4.3 are shown in figure 4.9 and screening runs shown in figures D.6 and D.7. Complexes 4.2 and 4.3 exhibit very weak ligand

based emission. For these complexes the high energy band shrinks to the point the low energy band is the main emissive feature for these complexes. In both complex 4.2 and 4.3 there is quenching of what is likely a ligand charge transfer state, which is likely due to relaxation from the excited state through non-radiative pathways, and is likely caused by a large numbers of intermediates of Tb(III) and Dy(III) ions. The more efficient quenching occurs in complex 4.3, and it is likely due to the smaller energy gap between the lowest emissive state of the metal ion, and the highest energy sublevel of the ground state multiplets. For Dy(III) this is the energy gap between $^4F_9 \rightarrow^6 F_{3/2}$ which has an energy of $7850cm^{-1}$, and for Tb(III)[91] this corresponds to the energy gap between $^5D_4 \rightarrow^7 F_0$ which has a value of $14800cm^{-1}$. As the energy gap becomes smaller, it becomes more likely that the relaxation from the excited state becomes non-radiative. Gd(III) has a large energy gap between the excited state ($^6P_{7/2}$) and it's ground state ($^8S_{7/2}$), which has a value of $32000cm^{-1}$. This energy gap is of higher energy then the radiative state at room temperature ($24200cm^{-1}$), and as such radiative emission occurs. As the concentration increases for solutions of 4.2 and 4.3 a large emission band centred at 600-650nm appears(figures D.12 and D.13 respectively). This band is due to an aggregation phenomena which is responsible for generating the respective emissive state.

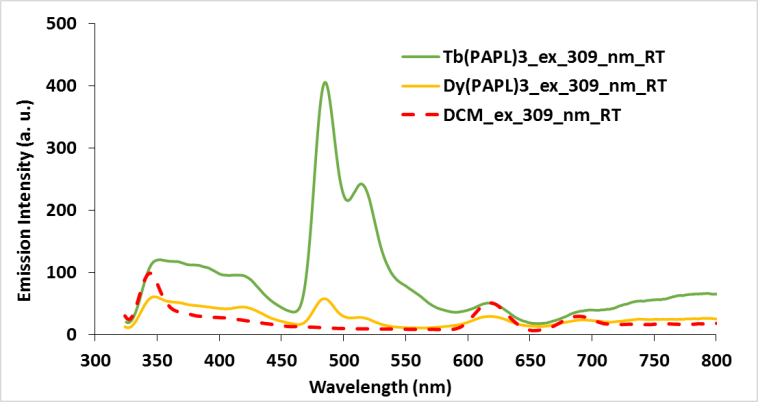

FIGURE 4.9: Emission profile of complexes 4.2 (green trace) and 4.3 (yellow trace): Performed in DCM at room temperature.

Chapter 5

Synthesis and Coordination Chemistry(M=Co(III), Fe(II)) of 1-(8-quinolinazo)-2-phenanthrol

5.1 Introduction

This chapter is focused on the new ligand 1-(8-quinolinazo)-2-phenanthrol (QAPL), which was synthesized with the goal of tuning the ligand field of 3.1 in order to generate spin crossover, or valence tautomerism in multifunctional complexes (by combining magnetic properties with dye like-properties or conductivity) of iron or cobalt.

5.2 QAPL and precursors(5.1-5.2)

5.2.1 Structural Characterization

The synthesis of ligand 5.2 is shown in scheme 5.1. Compound 5.1 though not new, is poorly documented in literature, so it has been fully characterized.

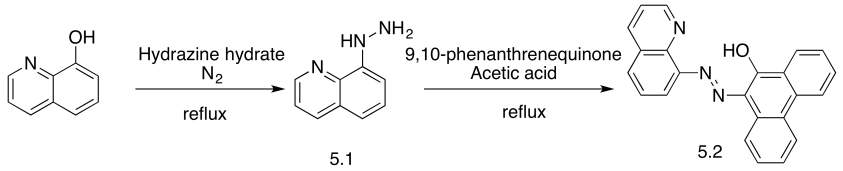

SCHEME 5.1: Synthesis of 5.1 and 5.2

Compound 5.1 is obtained as a yellow needle like crystal when prepared under a nitrogen atmosphere. The yellow crystals appear upon cooling to room temperature, and are soluble in a variety of solvents including glacial acetic acid, ethanol, DCM, and chloroform. In air a brown decomposition product is produced over the course of the reaction, and the yield is significantly decreased. Purification of reaction mixtures with the decomposed product can successfully be achieved via recrystallization of the crude product in a 1:1 hexanes/ethanol solution, which is then cooled to -8^oC. ^1H and ^{13}C NMR spectra are shown in figures 5.1 and 5.2.

Compound 5.2 is synthesized by the reaction of 5.1 with 9,10-phenanthrenequinone in glacial acetic acid. Neutralization of the acidic reaction mixture produces a crude mixture, which varies in colour from burgundy to black, with the general trend being that the lighter the colour of the reaction mixture, the larger the

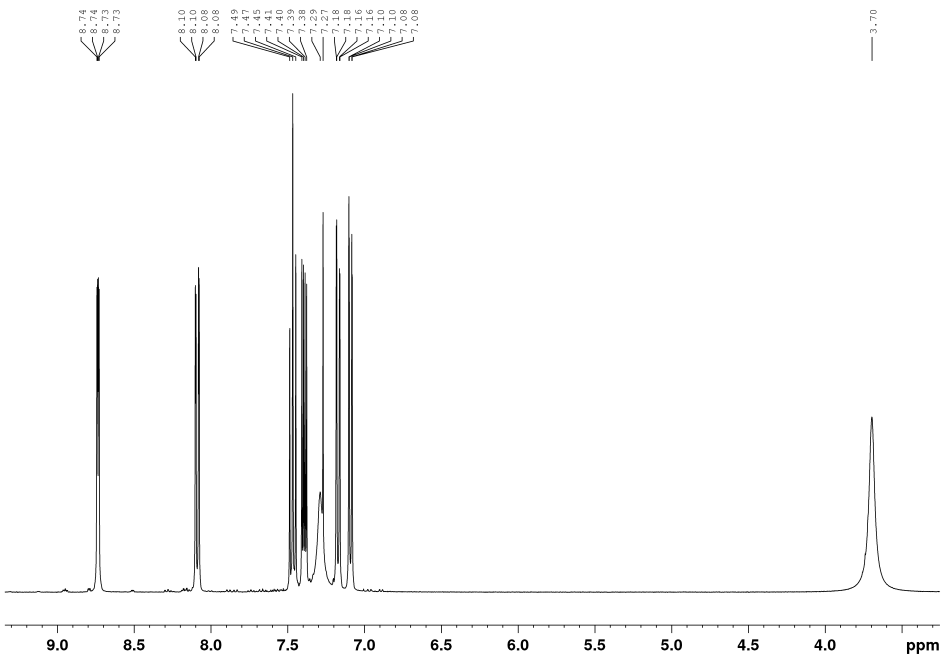

FIGURE 5.1: ^{13}H NMR spectrum of 5.1, performed in $CDCl_3$.

amount of compound 5.2 present. Compound 5.2 is obtained as a bright red powder by purification of the crude precipitate by column chromatography using DCM/hexanes as eluant. Compound 5.2 was expected to be obtained as keto-enol tautomers similar to 3.1 but the purified product is shown to be entirely the iminoquinone tautomer (the presence of only 1 tautomer in the ^{13}C NMR (figure 5.4) with a peak at 207ppm that can only correspond to C=O carbon, and only one tautomer in the ^{1}H NMR(figure 5.3)). Compound 5.2 is less soluble than 3.1, but it is fully soluble in DCM and chloroform, while slightly soluble in acetonitrile and methanol, allowing for the use of a variety of metal salts in coordination.

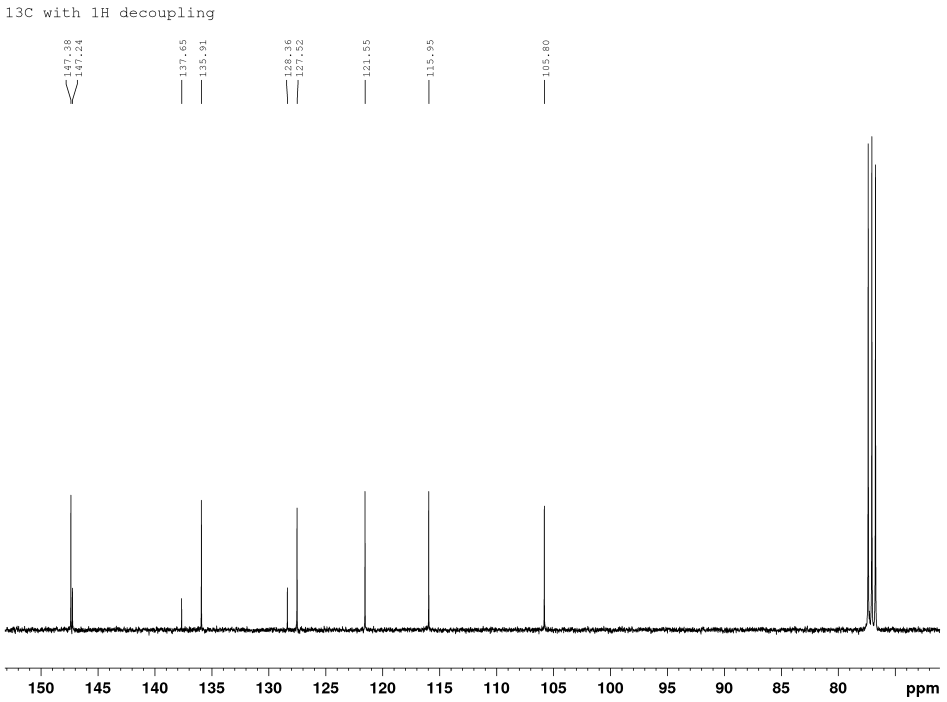

FIGURE 5.2: ^{13}C NMR spectrum of 5.1, performed in $CDCl_3$.

The FT-IR spectrum of 3.2 confirms the presence of only the iminoquinone tautomer in the solid state. This is due to the lack of a broad peak at high energy indicating that a phenol hydrogen is not present, a peak at $1600cm^{-1}$ which likely belongs to the C=O stretch of the iminoquinone, and a high energy absorption at $2957cm^{-1}$ which may belong to the N-H band of the iminoquinone tautomer, which is red-shifted.

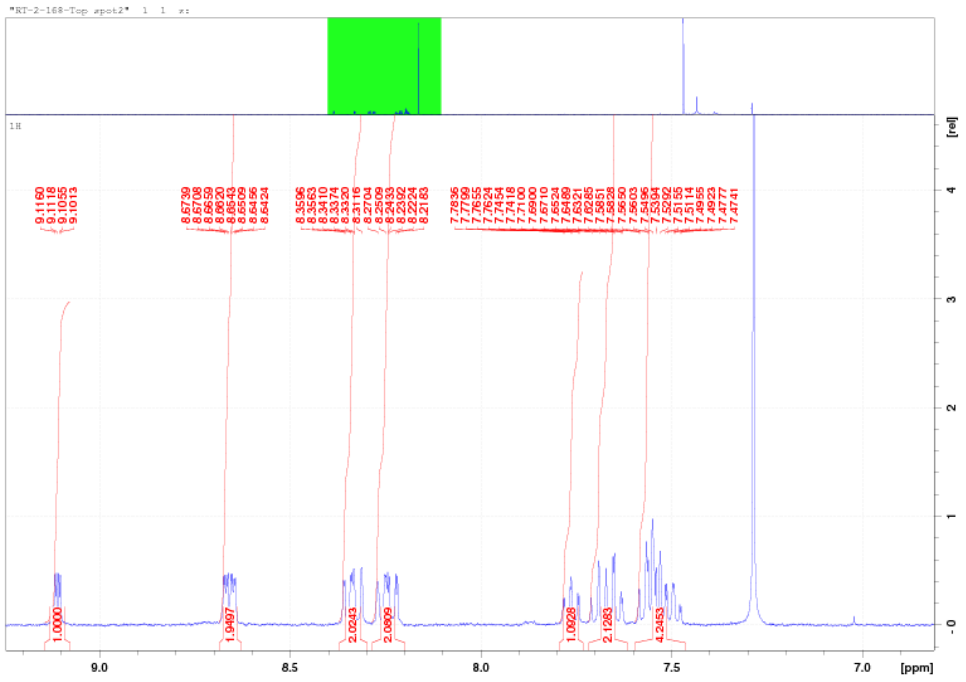

FIGURE 5.3: ^1H NMR spectrum of 5.2, performed in $CDCl_3$.

5.2.2 Electronic Properties

The electronic spectrum of 5.2 was measured in DCM (figure 5.5) and is very similar to compound 3.1 (figure 4.4). The spectrum features an intense absorption band centered at 500nm ($\epsilon = 3x10^4 M^{-1}cm^{-1}$) which is much more intense than the similar peak seen in uncoordinated 3.1, and is likely the result of $n-\pi^*$ transitions into an azo-type LUMO. Observed in conjunction with the peak centered at 500nm is a peak at higher energy which has a shoulder that extends to 350nm. This higher energy band is likely the result of $\pi-\pi^*$ transitions, however TD-DFT calculations are needed to confirm the assignments.

The redox activity of compound 5.2 was probed by CV (figure 5.6) and DPV (figure

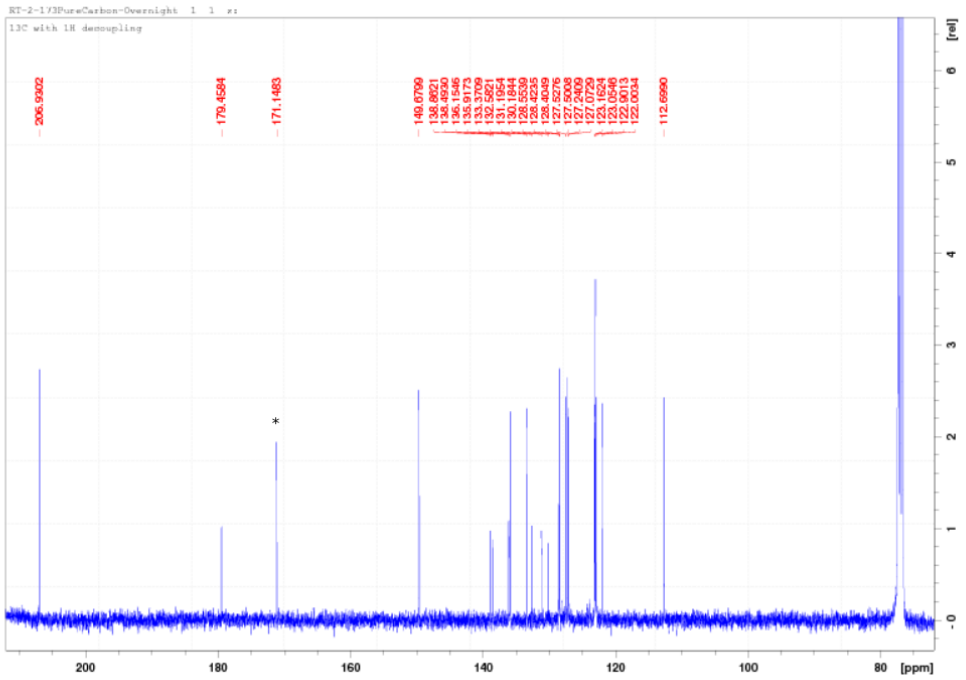

FIGURE 5.4: ^{13}C NMR spectrum of 5.2, performed in $CDCl_3$. Starred peak at 171ppm is ethyl acetate

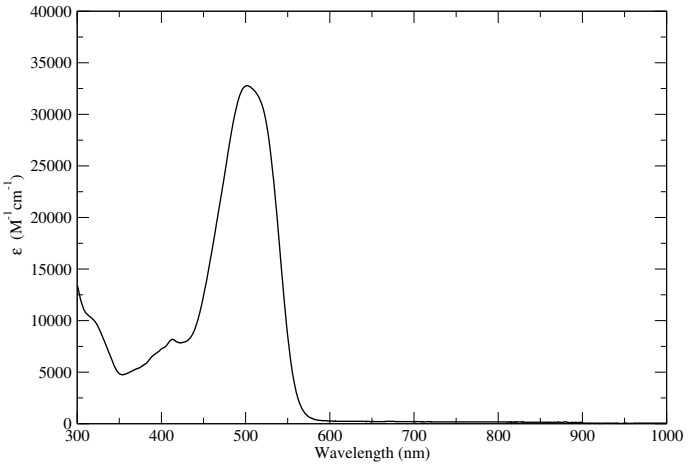

FIGURE 5.5: UV-Visible spectrum of 5.2: Performed in DCM at room temperature.

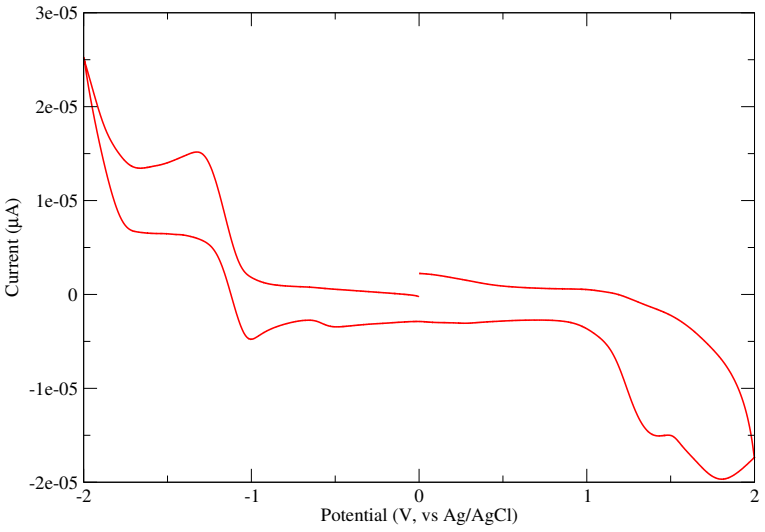

FIGURE 5.6: CV of 5.2 in DCM over the range of -2V to 2V at a scan rate of 200mV/s

Compound	$E_{1/2}$ anodic (V vs Ag/AgCl)	$E_{1/2}$ cathodic (V vs Ag/AgCl)
5.2	1.4(irr), 1.8(irr)	-1.2(qr)
5.3	1.2(qr), 1.3(irr)	-0.4(qr), -1.2(qr), -1.5(qr)
5.4	0.1(qr), 1.3(qr), 1.8(irr)	-0.8(qr), -1.3(qr), -1.7(qr)

TABLE 5.1: Electrochemical data for 5.2-5.4

5.7), with half wave potentials for 5.2 and corresponding complexes placed in table 5.1. At cathodic potentials (with reference to Ag/AgCl) there is a single quasi-reversible wave at -1.2V, which is assigned as the reduction of 5.2, by the addition of an electron to the azo-centred LUMO. This wave is at a lower potential than the similar peak observed in uncoordinated 3.1. The electrochemical behaviour suggests that 5.2 is likely to have a more stable radical anion than the one-electron reduction product of 3.1. At anodic potentials there are two irreversible waves centered at 1.3 and 1.6V. The lower potential wave is assigned as the one electron oxidation of the C-O bond.

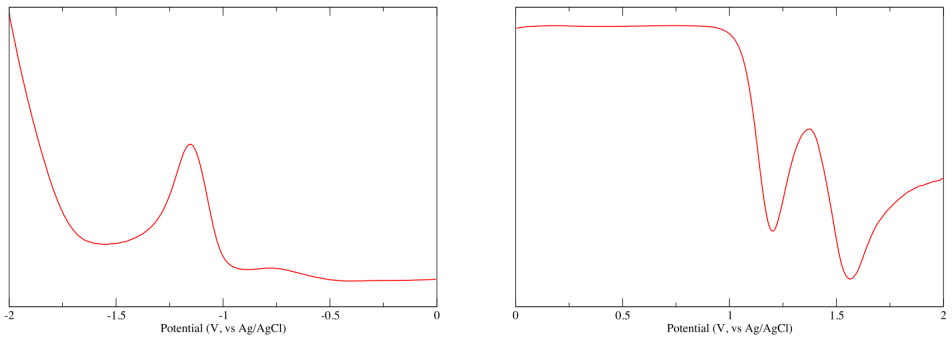

FIGURE 5.7: Left: Cathodic DPV of 5.2. Right: Anodic DPV of 5.2. Performed in DCM at a scan rate of 25mV/s, y-axis is μA

5.3 $[\mathbf{Co(QAPL)_2}]\mathbf{Cl}(5.3)$

5.3.1 Structural Characterization

Complex 5.3 is generated by coordination of 5.2 with $CoCl_2 \cdot 6H_2O$ in an acetonitrile/DCM mixture under an inert atmosphere. Stirring the reaction mixture produces a clear royal purple colour over 12 hours. Layering of diethyl ether followed by subsequent slow evaporation (either under N_2 or air) produced purple plate-like single crystals of 5.3.

The FT-IR spectrum obtained for 5.3 is similar to the spectrum obtained for complexes of 3.1. The absence of NH or OH stretches in the spectrum of 5.3 indicates that 5.2 is fully coordinated to Co(III). The crystal structure was determined to contain 1.5 equivalents of acetonitrile, and one equivalent of water by microanalytical analysis, and single crystal X-ray diffraction.

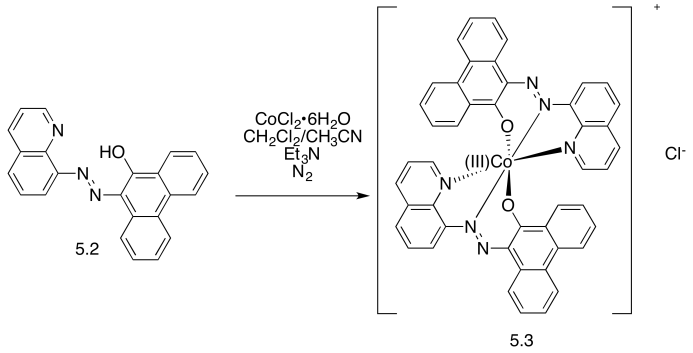

SCHEME 5.2: Synthesis of complex 5.3

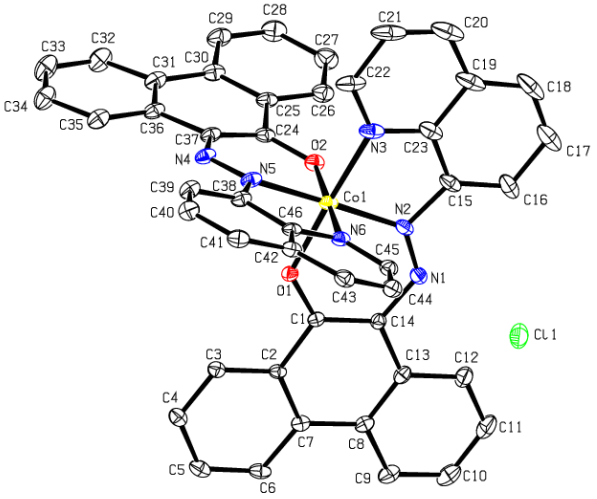

FIGURE 5.8: Displacement ellipsoid plot of 5.3: Solvent and H atoms omitted for clarity. Bond lengths in $\AA$, and bond angles in ^{o}: Co(1)-O(1), 1.8717(17); Co(1)-O(2), 1.8842(18); Co(1)-N(2), 1.891(2); Co(1)-N(5), 1.895(2); Co(1)-N(6), 1.920(2); Co(1)-N(3), 1.923(2); O(1)-C(1), 1.284(3); O(2)-C(24), 1.288(3); N(1)-N(2), 1.284(3); N(1)-C(14), 1.349(3); N(2)-C(15), 1.413(3); N(3)-C(22), 1.327(4); N(3)-C(23), 1.369(4); N(4)-N(5), 1.286(3); N(4)-C(37), 1.356(3); N(5)-C(38), 1.412(3); N(6)-C(45), 1.322(3); N(6)-C(46), 1.369(3). O(1)-Co(1)-O(2), 92.09(8); O(1)-Co(1)-N(2),92.28(8); O(2)-Co(1)-N(2), 87.03(9); O(1)-Co(1)-N(5), 86.03(8); O(2)-Co(1)-N(5), 92.32(9); N(2)-Co(1)-N(5), 178.17(9); O(1)-Co(1)-N(6), 90.46(8); O(2)-Co(1)-N(6), 176.07(9); N(2)-Co(1)-N(6), 95.85(9); N(5)-Co(1)-N(6), 84.87(9); O(1)-Co(1)-N(3), 176.81(10); O(2)-Co(1)-N(3), 86.91(8); N(2)-Co(1)-N(3), 84.65(10); N(5)-Co(1)-N(3), 97.03(10); N(6)-Co(1)-N(3), 90.70(9);

A single crystal X-ray diffraction experiment revealed a metal centered oxidation occurred (Co(II) to Co(III)) during the coordination reaction. The reaction was carried out under nitrogen, using a similar procedure as the coordination reaction which produced 3.2, so it was surprising to find that oxidation occurred. In the X-ray structure of 5.3, ligand 5.2 binds purely in the enolate state, similar to 3.1, as well as other azo-aromatic ligands[92]. Also the binding motif of 5.2 is different then that of 3.1. In complex 5.3, ligand 5.2 binds through the $N_{quionoline}$, $O^{-}_{phenanthrol}$, and N_{azo} donor atoms, but the N_{azo} atom which coordinates cobalt ion is the nitrogen atom closest to the quinoline ring. In all but one of the complexes for 3.1 the other N_{azo} atom coordinates the metal ion.

Complex 5.2 features distorted octahedral geometry about the cobalt ion, with coordinate bond lengths that are short similar to those reported for $[Co(PAPL)_2]Cl$[59]. The azo bond lengths are $1.284(3)\mathring{A}$ and $1.286(3)\mathring{A}$, which is similar to the azo bond distances of the anionic complexes of 3.1. In addition the C-O bond length is typical of a C-O single bond. The presence of the anion Cl^{-} in the structure, as well as the noted bond lengths place the oxidation state of cobalt at 3+ by charge balance.

5.3.2 Electronic Properties

The electronic spectrum of 5.3 was measured in DCM (figure 5.9). The peak with a maximum at 600nm ($\epsilon = 2x10^4 M^{-}1cm^{-1}$), with a shoulder that extends past

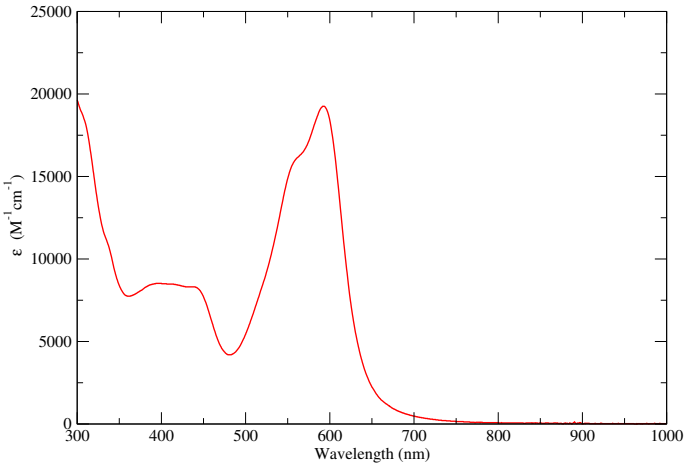

FIGURE 5.9: UV-Visible spectrum of 5.3: Performed in DCM at room temperature.

700nm, is much weaker than the maximum observed QAPL as well as the divalent iron complex, a trend that corresponds well with ligand 3.1. This spectrum is very similar to what is seen for the cobalt(III) PAPL complex[59], which indicates that the observed absorptions are mostly of ILCT character, with some minor LMCT character included.

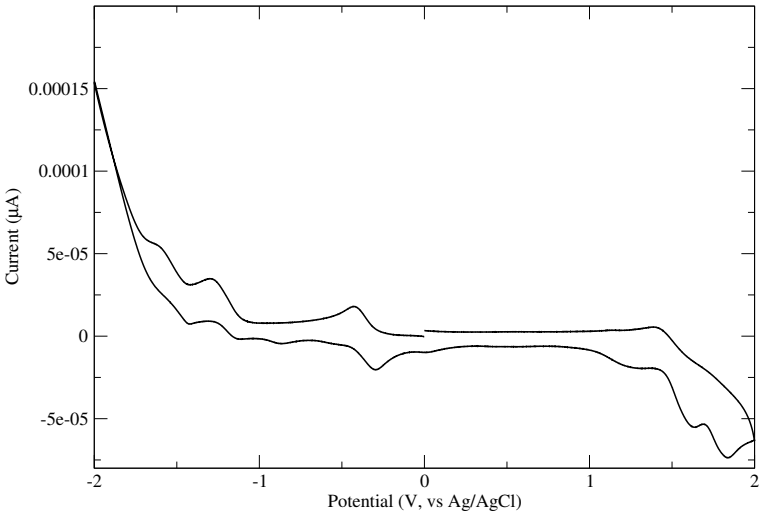

FIGURE 5.10: CV of 5.3 in DCM over the range of -2V to 2V at a scan rate of 200mV/s

The redox properties of 5.3 were investigated by CV (figure 5.10), and DPV (figure 5.11). At cathodic potentials the two quasi-reversible waves centered at -1.2, and -1.5V correspond to the ligand centered reduction of the azo bond. The quasi-reversible wave at -0.4V is assigned to the Co(3+/2+) couple. At high anodic potentials the waves centered at 1.2, and 1.3V are assigned as ligand centered oxidations.

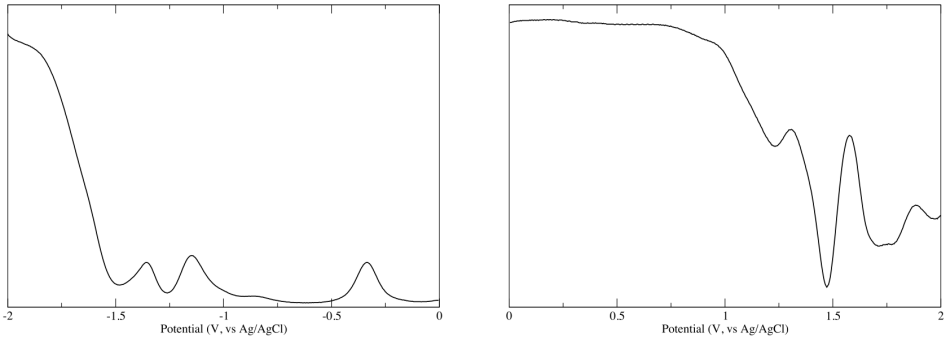

FIGURE 5.11: Left: Cathodic DPV of 5.3. Right: Anodic DPV of 5.3. Performed in DCM at a scan rate of 25mV/s, y-axis is μA

5.4 Fe(QAPL)$_2$(5.4)

5.4.1 Structural Characterization

The combination of 5.2 and $Fe(NO_3)_3 \cdot 9H_2O$ in a mixture of chloroform/methanol produced a black solution (scheme 5.3). Slow evaporation of the reaction mixture

provided a deep red precipitate that was analytically pure without the addition of solvent.

The FT-IR spectrum of the red powder was very similar to the divalent iron complexes of 3.1. There were no absorptions above $3000cm^{-1}$ to indicate that the powder contained uncoordinated ligand (no NH or OH stretches), as well as any absorptions which could belong to nitrate, which offers evidence for a divalent complex.

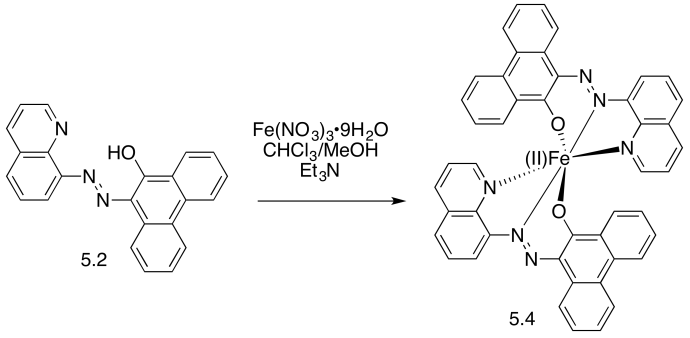

SCHEME 5.3: Synthesis of compound 5.4

5.4.2 Electronic Properties

The electronic spectrum of 5.4 was measured in DCM at 298K (figure 5.12). The spectrum features an intense absorption at nearly the same wavelength (500nm) as uncoordinated 5.2, but is slightly less intense ($\epsilon = 3x10^4 M^{-1}cm^{-1}$). This band is likely the result of ligand centered $n - \pi^*$ transitions. The higher energy peak is also similar to that of uncoordinated 5.2, and is likely $\pi - \pi^*$ transitions of the ligand. Of interest are two broad lower energy bands centred at 800nm

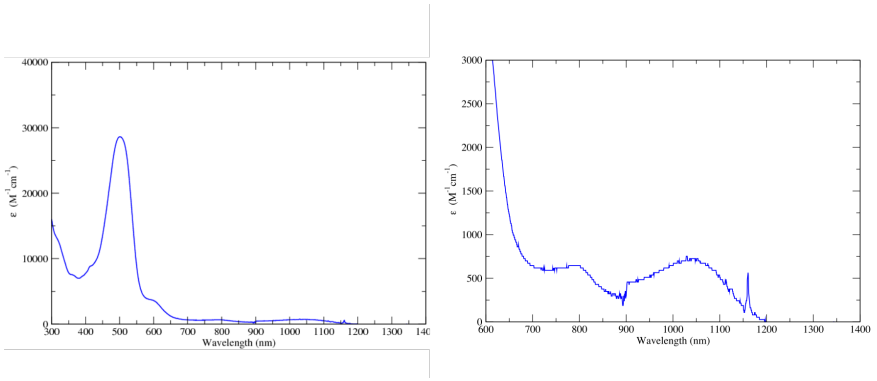

FIGURE 5.12: UV-Visible spectrum of 5.4 (left). Close up of the two low energy, weak absorption bands(right): Performed in DCM at room temperature.

($\epsilon = 600 M^{-1} cm^{-1}$) and 1050nm ($\epsilon = 700 M^{-1} cm^{-1}$). These bands are likely d-d transitions, however, TD-DFT is needed in order to confirm this assignment. Of note is the lack of the intense low energy band that is present in the iron complexes of ligand 3.1. This is likely due to an increase in coordinate bond lengths in 5.4, which results in weakened $\pi-$backdonation.

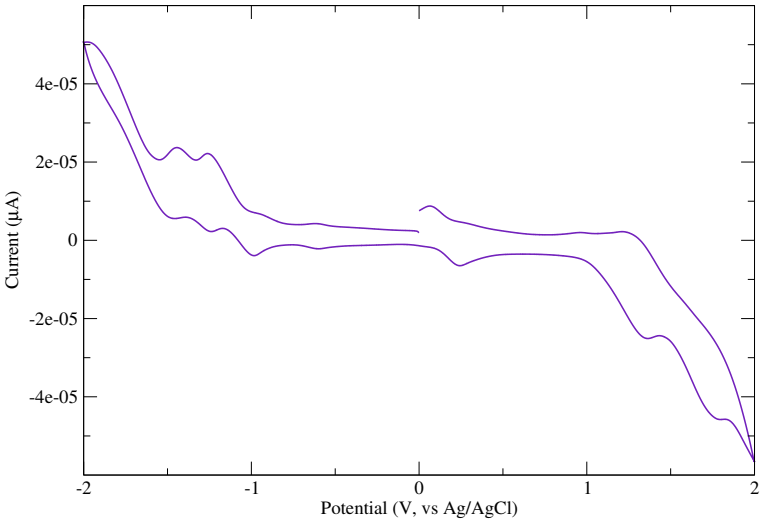

FIGURE 5.13: CV of 5.4 in DCM over the range of -2V to 2V at a scan rate of 200mV/s

The redox activity of 5.4 was investigated by CV (figure 5.13), and DPV (figure

5.14). The quasi-reversible wave at cathodic potentials -1.3, and -1.7V are assigned as the azo centered reduction of the coordinated 5.2. At anodic potentials the quasi-reversible low potential wave at 0.1V is assigned to the Fe(2+/3+) couple. The higher potential anodic waves at 1.3, and 1.8V are likely ligand centered oxidations.

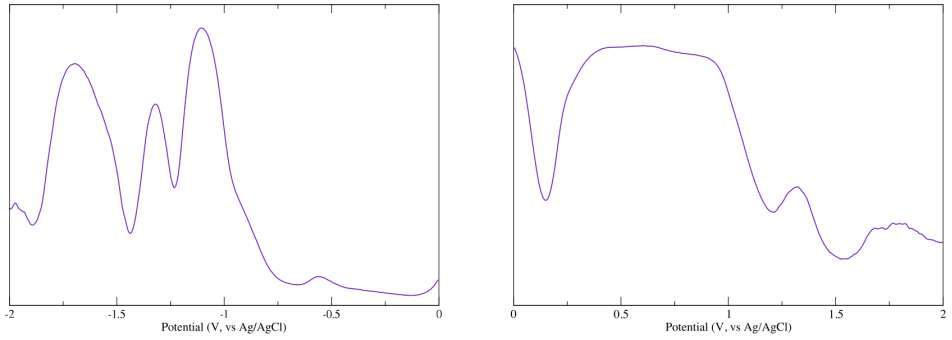

FIGURE 5.14: Left: Cathodic DPV of 5.4. Right: Anodic DPV of 5.4. Performed in DCM at a scan rate of 25mV/s, y-axis is μA

Chapter 6

Conclusions and Perspectives

In conclusion we have herein reported seven transition metal complexes with the ligand PAPL. The complexes were characterized by CV, DPV, mass spectrometry, UV-Visible spectroscopy, FT-IR spectroscopy, and X-ray diffraction (for six of the seven complexes). Paramagnetic complexes (3.2, 3.6 and 3.7) were further characterized by SQUID magnetometry, and EPR spectroscopy. In general all complexes of 3.1 feature intense absorptions in the visible region. Of particular interest is complex 3.2, which is a rare example of a Co(II) spin crossover complex with an NNO donor set. The presence of spin crossover was confirmed by a combination of SQUID magnetometry, solid state variable temperature EPR, and X-ray diffraction. In general all complexes of 3.1 share interesting structural features including short $\pi - \pi$ contacts.

Reduction attempts with uncoordinated 3.1 and its complexes were unsuccessful. For radicals generated by reduction to be stable, the radical must be both kinetically and thermodynamically stable. It is theorized that that reduced complexes of 3.1 are thermodynamically stable but kinetically unstable. The addition of large functional groups, such as *tert*-butyl groups, can sterically hinder the radical from reacting with other molecules, such as water or oxygen. The steric protection may allow for complexes with radical ligands similar to PAPL to be synthesized.

We also reported three lanthanide complexes with the ligand PAPL. These complexes were fully characterized by UV-Visible, and FT-IR spectroscopy, mass spectrometry, CV, and DPV electrochemical techniques, VSM magnetometry, and luminescence experiments. These complexes not only possess intense visible absorptions, on the order of $6x10^4 M^{-1}cm^{-1}$, but also interesting emmissive properties which were probed in collaboration with Hanan group at the University of Montreal. These complexes are of interest as there are few lanthanide azo-aromatic complexes that have been documented. Of particular interest is the ligand based luminescence seen in 4.1, and the quenching seen in complexes 4.2 and 4.3.

Finally we reported the synthesis of the new ligand QAPL. The new ligand and associated complexes were characterized by $^1H/^{13}C$ NMR, FT-IR and UV-Visible spectroscopy, mass spectrometry, CV, and DPV. The ligand 5.2 has intense absorption bands before coordination, as well as low potential quasi-reversible reductions presented in the CV. Preliminary coordination with Co(III) and Fe(II) offer insight into the coordination trends seen for this ligand, including a crystal

structure for 5.3. The electrochemical data found for these complexes suggest they are better candidates for one-electron reduction than complexes of 3.1. Complexes with this ligand framework may present charge transfer properties such as valence tautomerism, as well as other electron transfer induced spin-transitions.

Very few research groups actively study the magnetic properties of arylazo ligands. The azo-aromatic framework presented supports the use of arylazo ligands in the synthesis of spin-switching materials. Combined with the intense absorptions seen in nearly all the complexes presented, as well as interesting emission profiles, the azo-aromatic class of redox active ligands should be a future focus of materials chemists working with multifunctional materials.

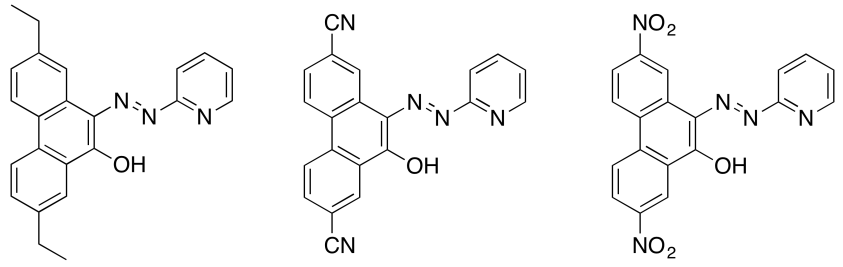

FIGURE 6.1: Possible synthetic targets based on the ligand PAPL

The findings of the present study indicate that future work performed in this area should have multiple foci. The azo-aromatic ligands presented have been shown to produce interesting magnetic properties. Tuning of the ligand field by either adding electron withdrawing/donating groups to either the phenanthrol group or the pyridine/quinoline group (figure 6.1) should allow for the generation of new spin crossover or charge transfer complexes. The other focus of future work should

pertain to poly-metal systems based on extending the azo-aromatic structure explored using ligand 3.1(figure 6.2). Initial attempts at synthesis presented interesting but insoluble complexes which were theorized to possess a grid structure[93]. Increasing the solubility by the addition of alkyl chains should allow for complete characterization of the complexes generated using polytopic ligands. The complexes should be interesting as they may exhibit interesting magnetic properties, such as valence tautomerism, or intense ligand based luminescence. Reduction of the azo bond in these complexes could lead to strong magnetic coupling, which may result in interesting magnetic behaviour including multi-step spin crossover in iron and cobalt complexes, or SMMs possessing large anisotropic barriers to thermal relaxation.

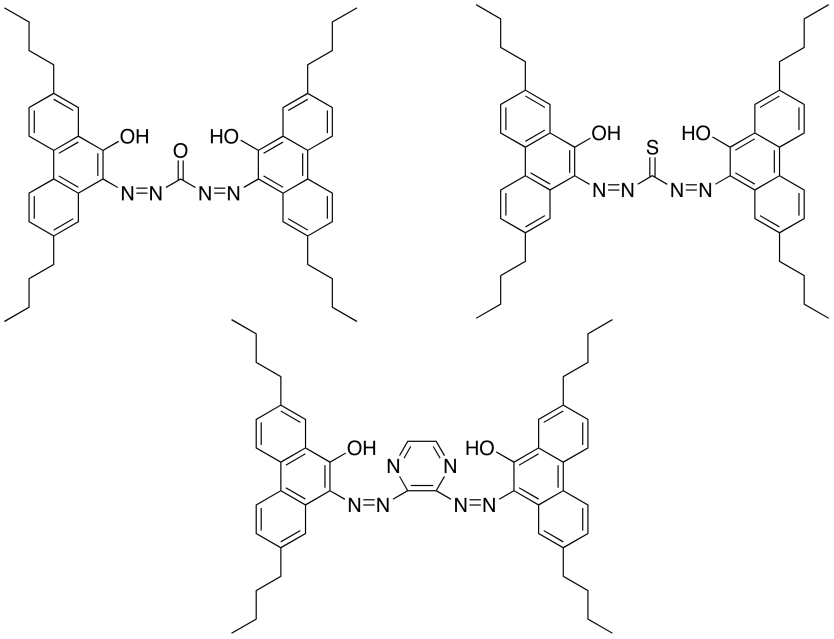

FIGURE 6.2: Possible synthetic targets based on the ligand PAPL

Appendix A

Additional Structural Information

A.1 $Co(PAPL)_2 \cdot CH_2Cl_2$

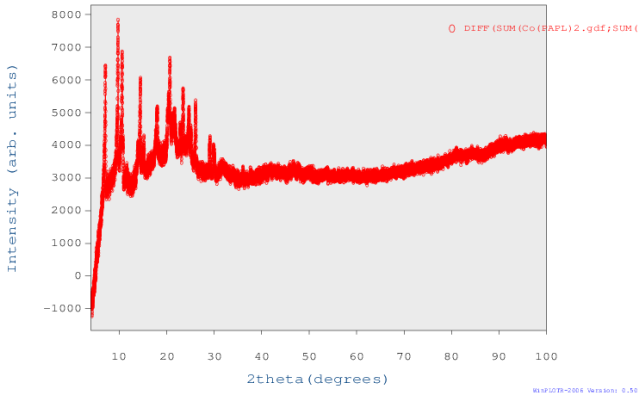

FIGURE A.1: pXRD spectrum of a powder sample of 3.2 at 300K.

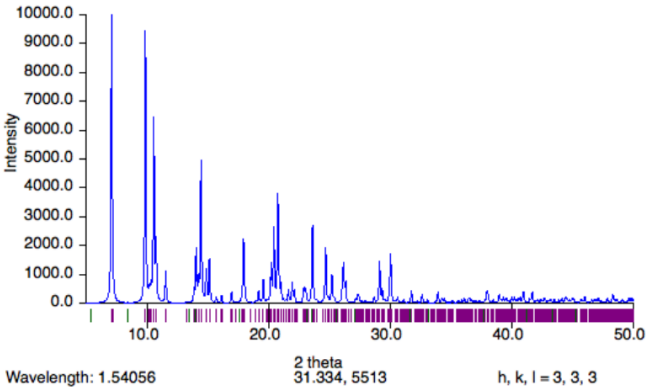

FIGURE A.2: Simulated pXRD spectrum of 3.2

A.2 $Fe(PAPL)_2$

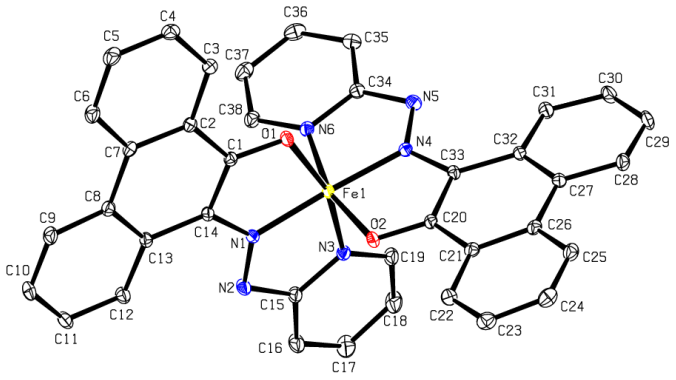

FIGURE A.3: Displacement ellipsoid plot of decomposed 3.7: H atoms omitted for clarity. Select bond lengths ($\AA$) and bond angles (^{o}) with standard uncertainties in brackets: Fe1-O1, 1.9597(13); Fe1-O2, 1.9561(14); Fe1-N1, 1.8703(16); Fe1-N3, 1.9288(16); Fe1-N4, 1.8683(16); Fe1-N6, 1.9263(17); N1-N2, 1.321(2); N4-N5, 1.320(2); C1-O1, 1.292(2); C20-O2, 1.290(2); C14-N1, 1.373(82); C33-N4, 1.371(2); C1-C14, 1.414(3); C20-C33, 1.418(3). N4-Fe1-N1, 177.07(7); N4-Fe1-N6, 80.41(7); N1-Fe1-N6, 100.68(7); N4-Fe1-O2, 82.56(6); N1-Fe1-O2, 96.44(6); N6-Fe1-O2, 162.84(6); N4-Fe1-N3, 96.90(7); N1-Fe1-N3, 80.40(7); N6-Fe1-N3, 90.68(7); O2-Fe1-N3, 93.42(6); N4-Fe1-O1, 100.02(6); N1-Fe1-O1, 82.74(6); N6-Fe1-O1, 89.12(6); O2-Fe1-O1, 91.82(6); N3-Fe1-O1, 162.80(6).

A.3 $Tb(PAPL)_3 \cdot 0.4CHCl_3$

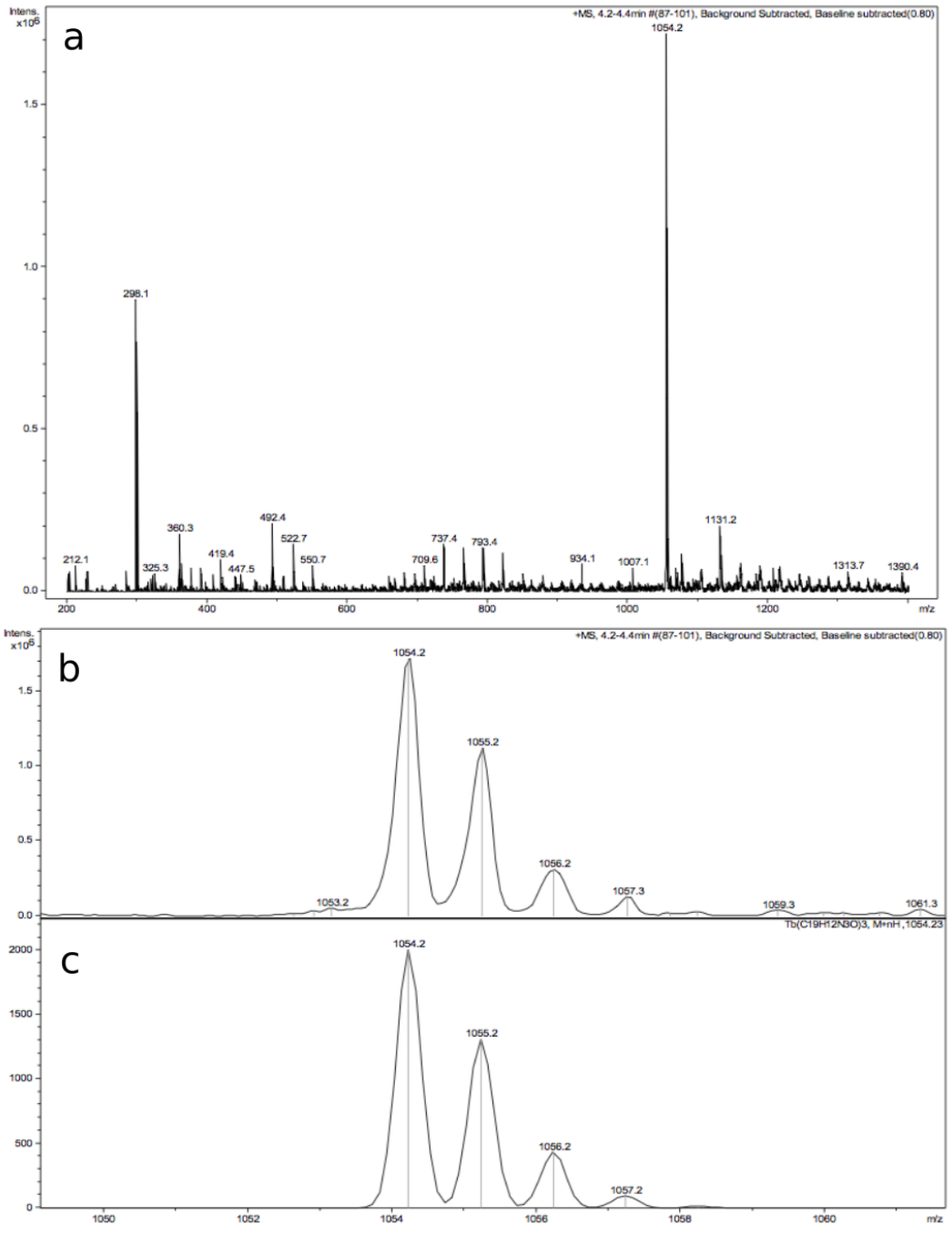

FIGURE A.4: a: Mass spectrum for 4.2 b: Observed isotope pattern for 4.2 c: Simulated isotope pattern for 4.2

A.4 $Dy(PAPL)_3$

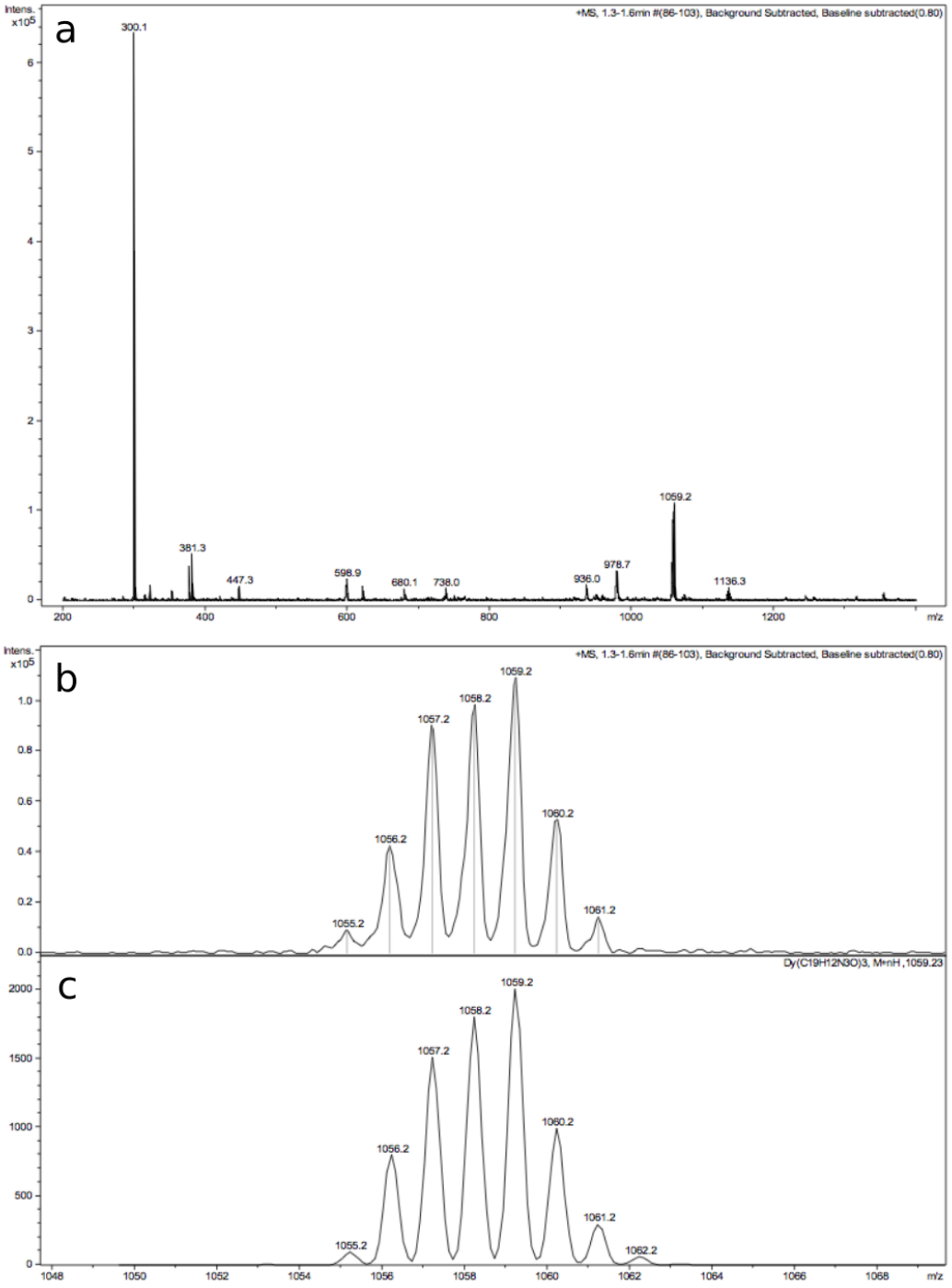

FIGURE A.5: a: Mass spectrum for 4.3 b: Observed isotope pattern for 4.3 c: Simulated isotope pattern for 4.3

Appendix B

Additional Magnetic Data

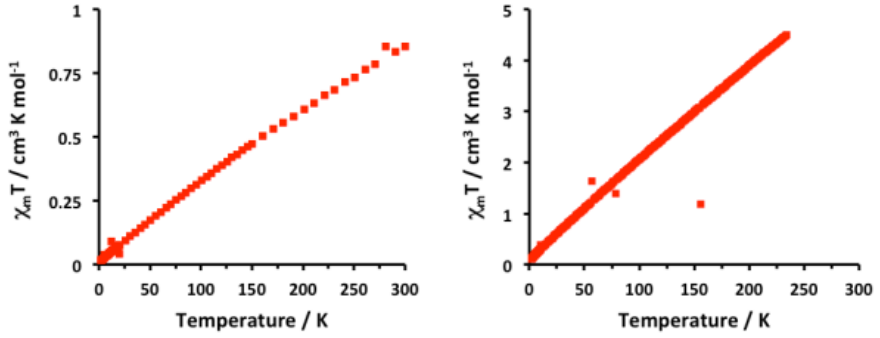

FIGURE B.1: $\chi_m TvsT$ plot for multiple runs of 3.3: with an unknown paramagnetic impurity in an external field of $2000Oe$

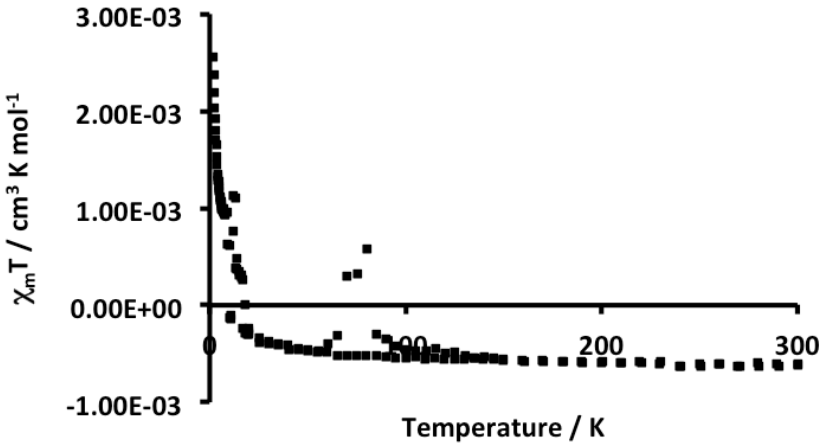

FIGURE B.2: $\chi_m TvsT$ plot for multiple runs of 3.4: in an external field of $2000Oe$

Appendix C

Additional Electrochemical Data

C.1 $Ru(PAPL)_2 \cdot 3.9CH_3OH(3.5)$

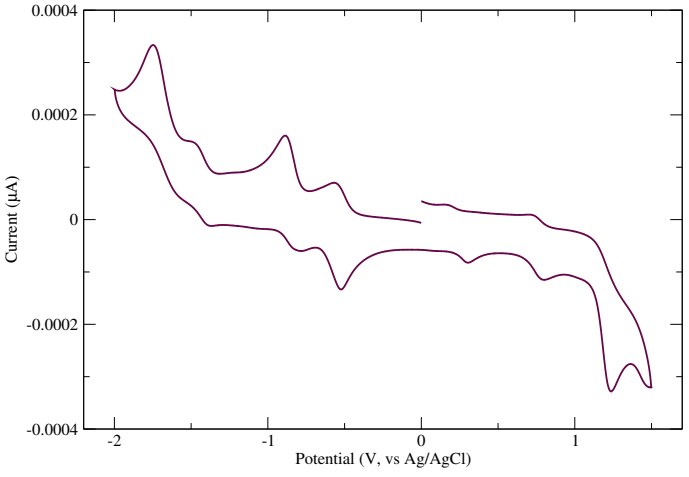

FIGURE C.1: CV of 3.5 over the range of -2V to 1.5V, performed in DMF at a scan rate of 100mV/s

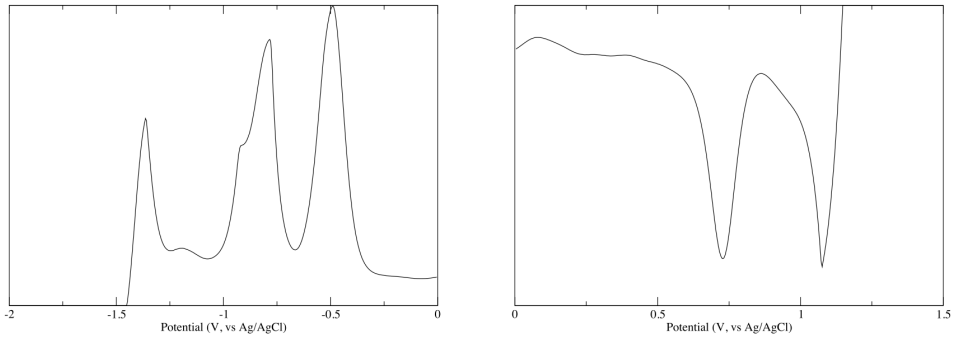

FIGURE C.2: Left: Cathodic DPV of 3.5, over the range of -2.0V to 0V. Right: Anodic DPV of 3.5, over the range of 0V to 1.5V. In both cases performed in DMF, y-axis is μA.

C.2 $[Fe(PAPL)_2]I_3 \cdot 1.55CH_2Cl_2$(3.7)

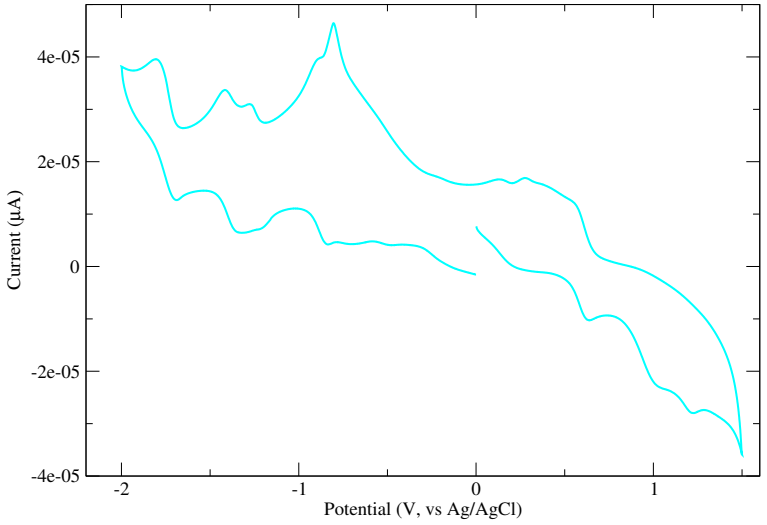

FIGURE C.3: CV of 3.7 in DMF over the range of -2.5V to 1.5V at a scan rate of 100mV/s

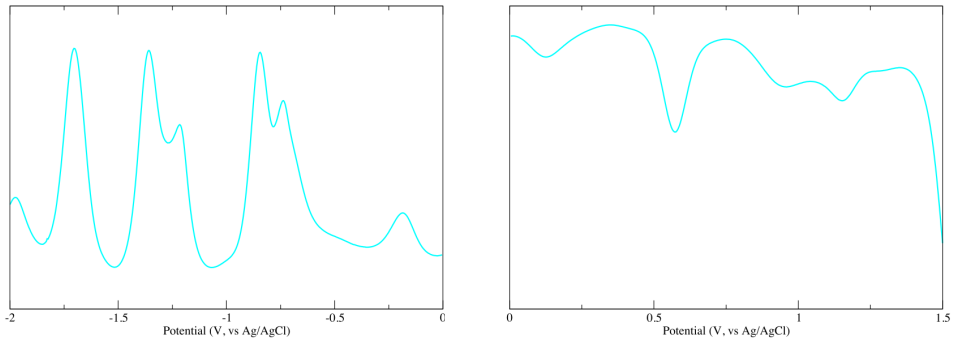

FIGURE C.4: Left: Cathodic DPV of 3.7, over the range of -2.0V to 0V Right: Anodic DPV of 3.7, over the range of 0V to 1.5V. In both cases performed in DMF, scan rate 25mV/s, y-axis is μA.

C.3 $[(\mathbf{PAPL})\mathbf{VO}]_2\mu - \mathbf{O_2}(\mathbf{3.8})$

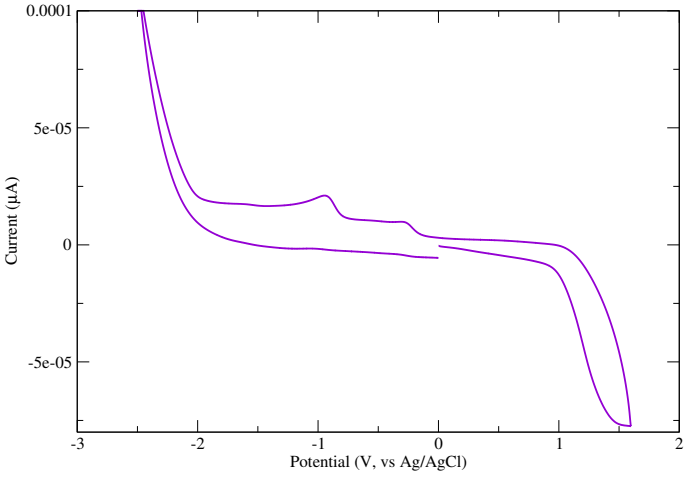

FIGURE C.5: Cyclic voltammogram of 3.8, performed in DMF over the range of -2.5V to 1.5V at a scan rate of 200mV/s

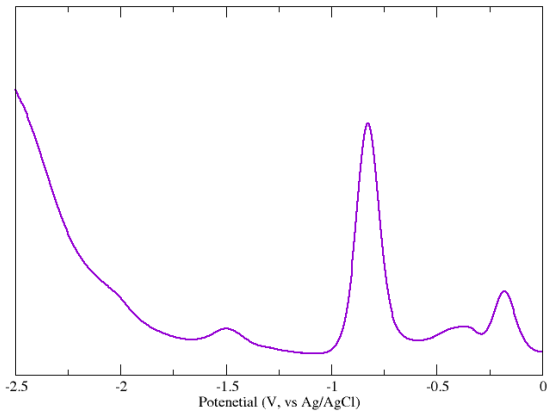

FIGURE C.6: Cathodic DPV of 3.8 performed in DMF over the range of -2.5V to 0V at a scan rate of 25mV/s

C.4 $CuPAPL_2 \cdot 0.3CH_2Cl_2$(3.6)

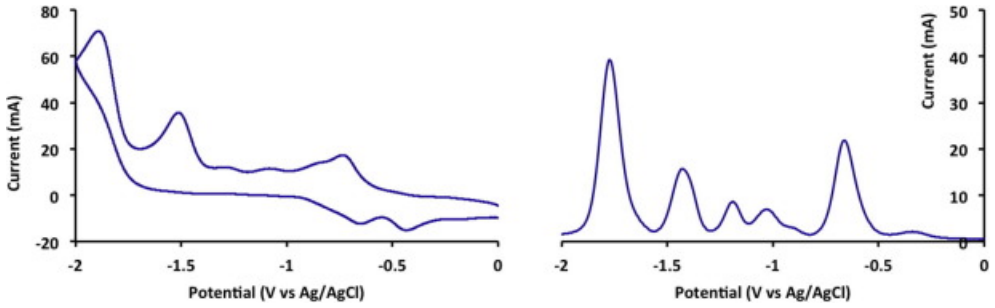

FIGURE C.7: Cathodic CV(left) and DPV(right) of 3.6, performed in DCM at a scan rate of 100mV/s (for CV) and 25mV/s (for DPV)

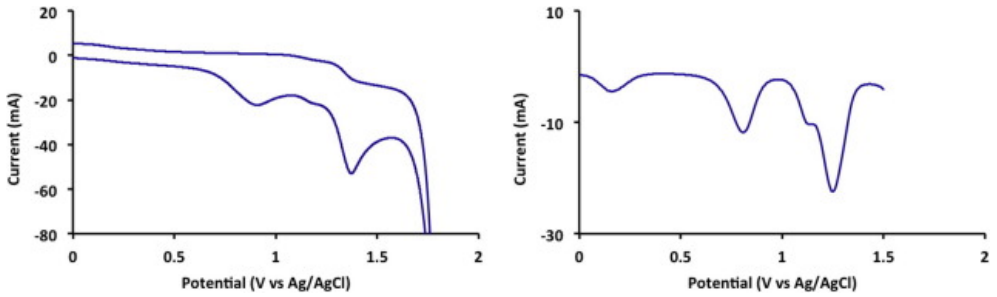

FIGURE C.8: Anodic CV(left) and DPV(right) of 3.6, performed in DCM at a scan rate of 100mV/s (for CV) and 25mV/s (for DPV)

C.5 Lanthanide PAPL complexes

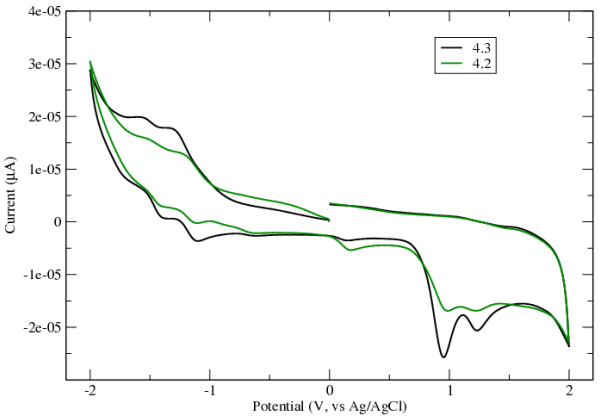

FIGURE C.9: CVs of 4.2 amd 4.3, performed in DCM at a scan rate of 200mV/s

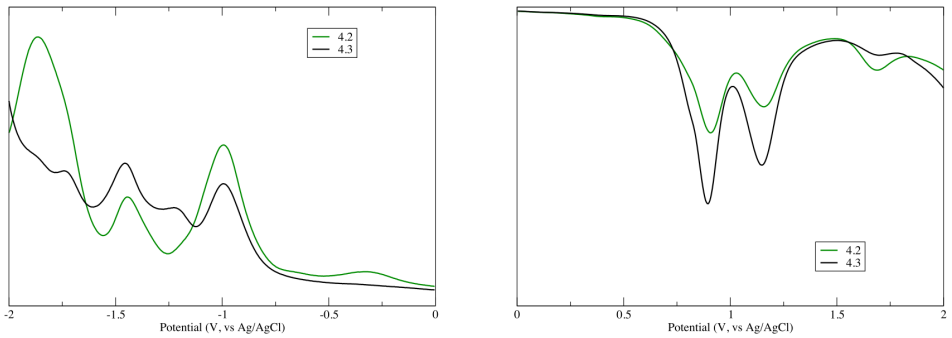

FIGURE C.10: Left: Cathodic DPVs of 4.2, and 4.3. Right: Anodic DPVs of 4.2 and 4.3. Performed in DCM at a scan rate of 25mV/s. In both cases the y-axis scale is in μA

Appendix D

Additional Luminescence Data

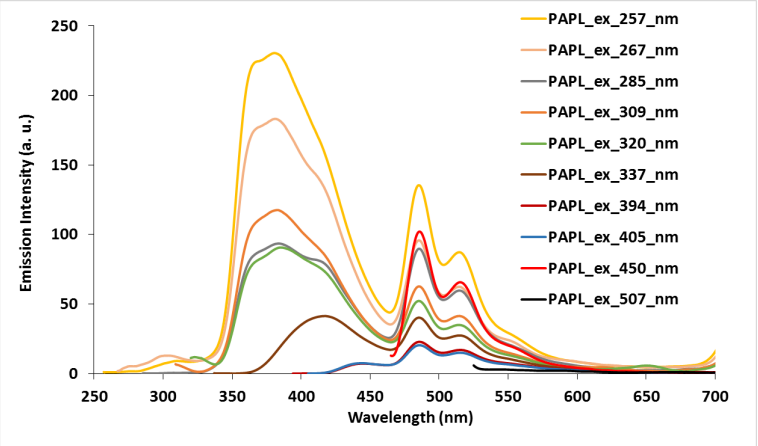

FIGURE D.1: Emission profile of 3.1 at multiple λ_{exc}(257-507nm): Performed in DCM at room temperature

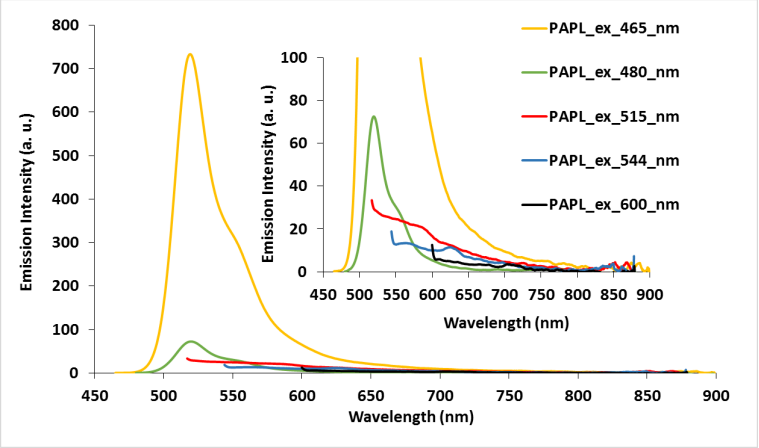

FIGURE D.2: Emission profile of 3.1 at multiple λ_{exc}(465-600nm): Performed in DCM at room temperature

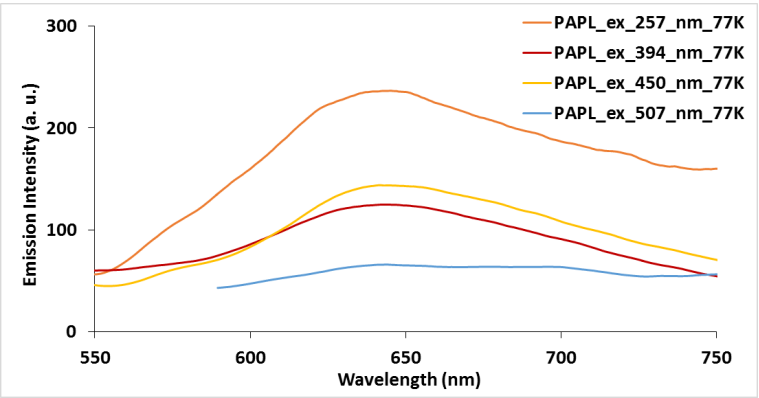

FIGURE D.3: Emission profile of 3.1 at multiple λ_{exc}(257-507nm) at 77K: Performed in DCM

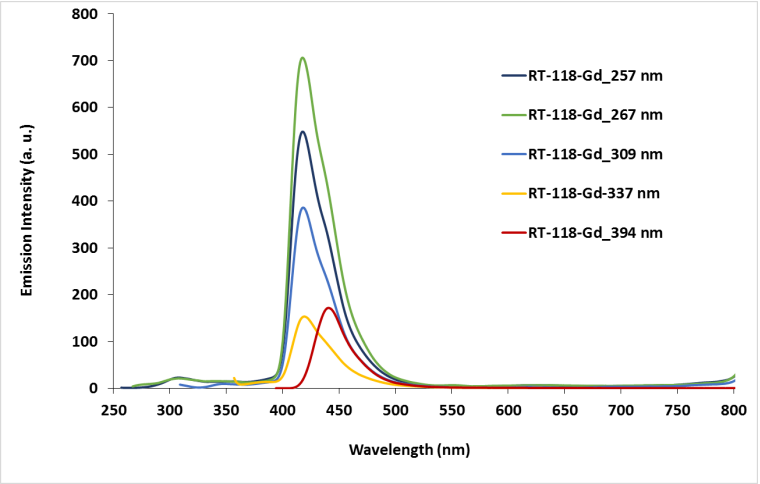

FIGURE D.4: Emission profile of 4.1 at multiple λ_{exc} at room temperature: Performed in DCM. There was no emission observed for λ_{exc} =517, 544, and 600nm. $\lambda_{max,emission} = 419nm$.

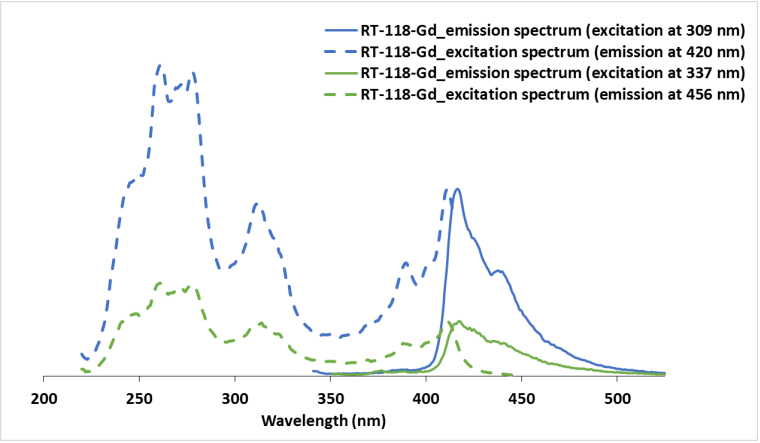

FIGURE D.5: Emission and excitation profiles of 4.1 at room temperature: Performed in DCM.

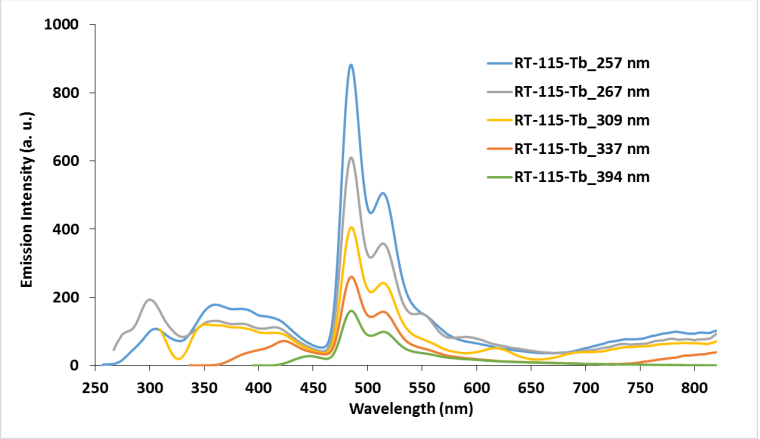

FIGURE D.6: Emission profile of 4.2 at multiple λ_{exc} at room temperature: Performed in DCM. There was no emission observed for λ_{exc} =517, 544, and 600nm. $\lambda_{max,emission}$=419, 485, and 515nm.

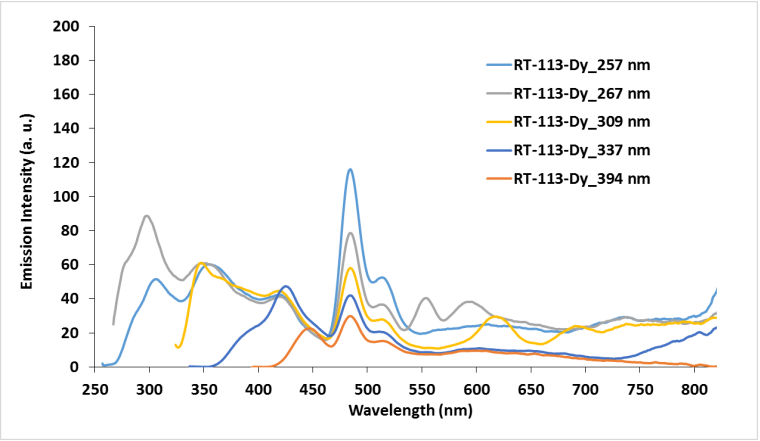

FIGURE D.7: Emission profile of 4.3 at multiple λ_{exc} at room temperature: Performed in DCM. There was no emission observed for λ_{exc} =517, 544, and 600nm. $\lambda_{max,emission}$=419, 485, and 515nm. Due to the very weak emission, the emission from the solvent is observed which is supported by figures D.8-D.11

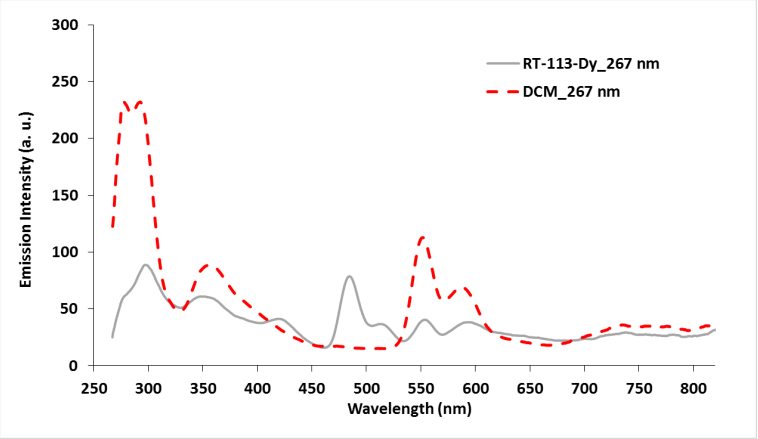

FIGURE D.8: Emission profile of 4.3 and DCM $\lambda_{exc} = 267nm$ at room temperature: Emission of 4.3 performed in DCM.

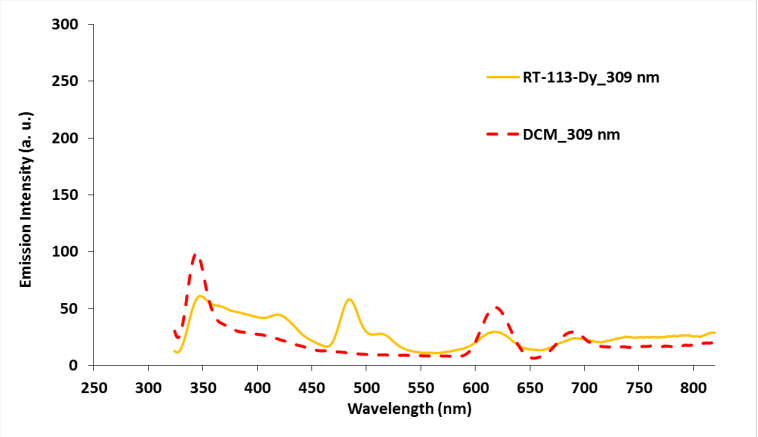

FIGURE D.9: Emission profile of 4.3 and DCM $\lambda_{exc} = 309nm$ at room temperature: Emission of 4.3 performed in DCM.

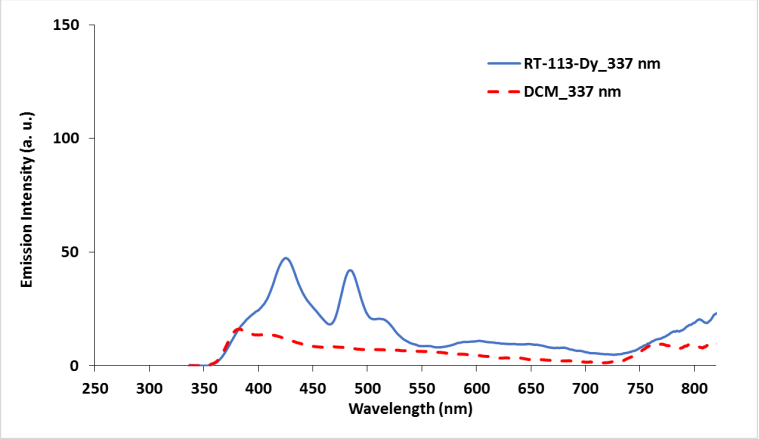

FIGURE D.10: Emission profile of 4.3 and DCM $\lambda_{exc} = 337nm$ at room temperature: Emission of 4.3 performed in DCM.

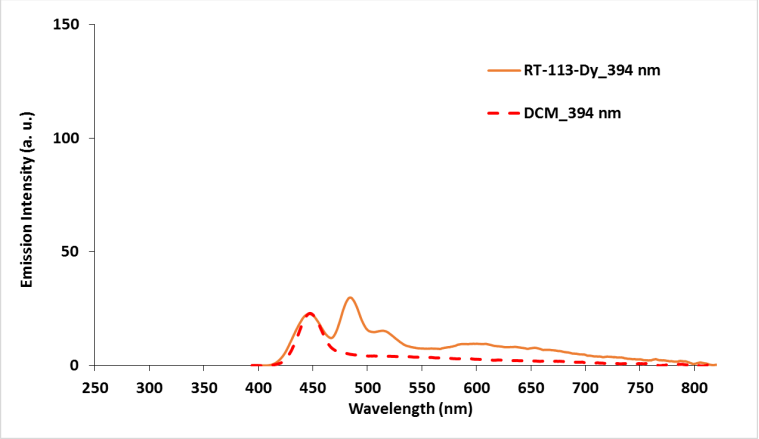

FIGURE D.11: Emission profile of 4.3 and DCM $\lambda_{exc} = 394nm$ at room temperature: Emission of 4.3 performed in DCM.

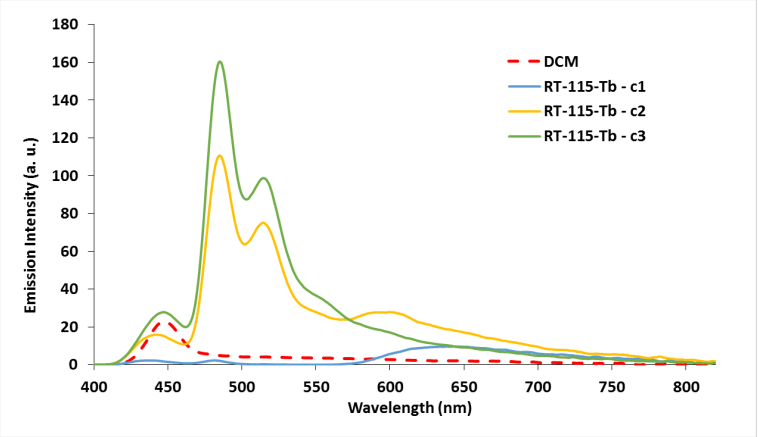

FIGURE D.12: Emission profile of 4.2 at different concentrations:$\lambda_{exc} = 394nm$ at room temperature: Performed in DCM; c1=$1.0X1O^{-4}M$, c2=$5.7X10^{-5}M$, c3=$9.5x10^{-6}M$.

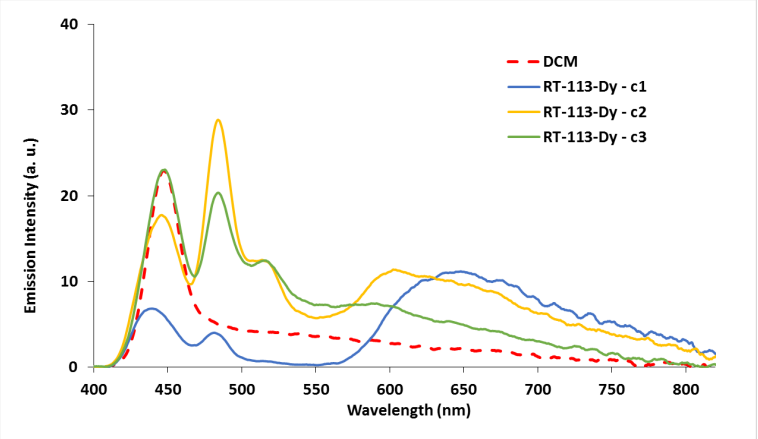

FIGURE D.13: Emission profile of 4.3 at different concentrations: $\lambda_{exc} = 394nm$ at room temperature: Performed in DCM; c1=$2.1X1O^{-4}M$, c2=$4.2X10^{-5}M$, c3=$6.9x10^{-6}M$.

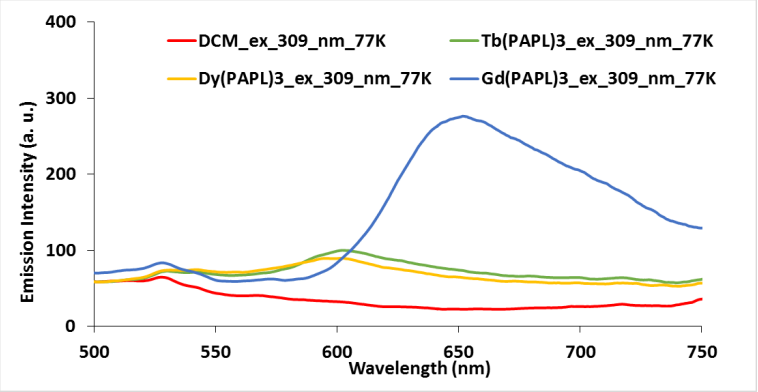

FIGURE D.14: Emission profile of 4.1-4.3 (performed in DCM) and DCM $\lambda_{exc} = 309nm$ at 77K

Appendix E

Crystallographic Information

Property	3.2 (147K)	3.2 (325K)
Empirical formula	$C_{38}H_{24}CoN_6O_2$	$C_{38}H_{24}CoN_6O_2$
Formula weight	655.56	655.56
Temperature	147(2)K	325(2)K
Wavelength	1.54178Å	1.54178Å
Crystal system	Monoclinic	Monoclinic
Space group	C2/c	C2/c
a	20.8833(6)Å	21.2693(9)Å
b	17.2831(4)Å	17.2515(7)Å
c	19.1606(8)Å	19.1030(8)Å
α	90^o	90^o
β	$121.054(1)^o$	$120.899(2)^o$
γ	90^o	90^o
Volume	$5924.5(3)Å^3$	$6014.6(4)Å^3$
Z	8	8
Density (calculated)	$1.470Mg/m^3$	$1.448Mg/m^3$
Absorption coefficient	$4.926mm^{-1}$	$4.852mm^{-1}$
F(000)	2696	2696
Crystal size	$0.200x0.150x0.130mm^3$	$0.200x0.150x0.130mm^3$
Theta range for data collection	3.556 to 67.273^o	3.525 to 67.293^o
Index ranges	-24≤h≤24, -20≤k≤20, -22≤l≤22	-25≤h≤24, -20≤k≤20, -22≤l≤22
Reflections collected	58184	35226
Independent reflections	5287 [R(int)=0.0772]	5341 [R(int)=0.0574]
Completeness to theta	99.5%	98.8%
Absorption correction	Semi-empirical from equivalents	Semi-empirical from equivalents
Max. and min. transmission	0.7529 and 0.6328	0.7529 and 0.6426
Refinement method	Full-matrix least-squares on F^2	Full-matrix least-squares on F^2
Data /restraints/parameters	5287/0/424	5341/0/424
Goodness-of-fit on F^2	1.031	1.021
Final R indices [I>2sigma(I)]	R1=0.0368, wR2=0.0852	R1=0.0368, wR2=0.0830
R indices (all data)	R1=0.0489, wR2=0.0912	R1=0.0566, wR2=0.0935
Extinction coefficient	n/a	n/a
Largest diff. peak and hole	0.250 and -0.454 $e.Å^{-3}$	0.169 and -0.202$e.Å^{-3}$

TABLE E.1: Crystal data and structure refinement for 3.2

Property	3.3 (120K)	3.3 (250K)
Empirical formula	$C_{39}H_{26}Cl_2FeN_6O_2$	$C_{38}H_{24}FeN_6O_2$
Formula weight	737.41	652.48
Temperature	120(2)K	250(2)K
Wavelength	0.71073Å	0.71073Å
Crystal system	Triclinic	Monoclinic
Space group	P-1	C2/c
Unit cell dimensions: a	10.5502(14)Å	22.189(2)Å
b	12.1178(16)Å	10.646(1)Å
c	14.5785(19)Å	14.7519(13)Å
α	109.524(4)^o	90^o
β	91.936(4)^o	112.713(3)^o
γ	114.382(4)^o	90^o
Volume	1567.6(4)Å^3	3214.5(5)Å^3
Z	2	4
Density (calculated)	1.562Mg/m^3	1.348Mg/m^3
Absorption coefficient	0.701mm^{-1}	0.513mm^{-1}
F(000)	756	1344
Crystal size	0.200x0.180x0.160mm^3	0.200x0.180x0.160mm^3
Theta range for data collection	1.513 to 27.660^o	1.990 to 27.558^o
Index ranges	-13≤h≤13, -15≤k≤14, 0≤l≤18, -22≤l≤22	-28≤h≤28, -13≤k≤13, -19≤l≤17
Reflections collected	49096	22529
Independent reflections	7157 [R(int)=0.0863]	3696 [R(int)=0.0587]
Completeness to theta	100%	100%
Absorption correction	Semi-empirical from equivalents	1.319
Max. and min. transmission	0.7456 and 0.6673	0.7456 and 0.6807
Refinement method	Full-matrix least-squares on F^2	Refinement method
Data /restraints/parameters	7157/0/461	3696/0/213
Goodness-of-fit on F^2	1.070	1.005
Final R indices [I>2sigma(I)]	R1=0.0794, wR2=0.1318	R1=0.0414, wR2=0.0959
R indices (all data)	R1=0.1236, wR2=0.1508	R1=0.0858, wR2=0.1173
Extinction coefficient	n/a	n/a
Largest diff. peak and hole	1.001 and -1.010 $e.Å^{-3}$	0.353 and -0.321$e.Å^{-3}$

TABLE E.2: Crystal data and structure refinement for 3.3

Property	3.4	3.7 (decomposed)
Empirical formula	$C_{38}H_{24}FeN_6O_2$	$C_{38}H_{24}FeN_6O_2$
Formula weight	652.48	652.48
Temperature	147(2)K	147(2)K
Wavelength	1.54178Å	0.71073Å
Crystal system	Orthorhombic	Triclinic
Space group	$Pca2_1$	P-1
Unit cell dimensions: a	12.7792(3)Å	10.212(1)Å
b	22.9446(5)Å	10.9635(11)Å
c	22.4688(7)Å	14.2193(14)Å
α	90^o	$92.843(3)^o$
β	90^o	$98.863(3)^o$
γ	90^o	$112.451(3)^o$
Volume	6588.2(3)$Å^3$	1443.5(2)$Å^3$
Z	8	2
Density (calculated)	$1.316Mg/m^3$	$1.501Mg/m^3$
Absorption coefficient	$4.017mm^{-1}$	$0.571mm^{-1}$
F(000)	2688	672
Crystal size	0.190x0.150x0.080mm^3	0.150x0.100x0.080mm^3
Theta range for data collection	1.925 to 67.231^o	1.460 to 27.571^o
Index ranges	-15≤h≤14, -27≤k≤20, -25≤l≤26	-13≤h≤13, -14≤k≤14, -18≤l≤18
Reflections collected	28054	39357
Independent reflections	9808 [R(int)=0.0527]	6664 [R(int)=0.0494]
Completeness to theta	98.5%	100.0%
Absorption correction	Semi-empirical from equivalents	Semi-empirical from equivalents
Max. and min. transmission	0.7529 and 0.5883	0.7456 and 0.7164
Refinement method	Full-matrix least-squares on F^2	Full-matrix least-squares on F^2
Data /restraints/parameters	9808/1/848	6664/0/424
Goodness-of-fit on F^2	1.030	1.039
Final R indices [I>2sigma(I)]	R1=0.0440, wR2=0.1083	R1=0.0368, wR2=0.0792
R indices (all data)	R1=0.0577, wR2=0.1145	R1=0.0597, wR2=0.0883
Absolute structure parameter	0.339(6)	-
Extinction coefficient	n/a	n/a
Largest diff. peak and hole	0.592 and -0.392$e.Å^{-3}$	0.651 and -0.419$e.Å^{-3}$

TABLE E.3: Crystal data and structure refinement for 3.4 and 3.7

Property	3.5	3.6
Empirical formula	$C_{42}H_{32}N_6O_3Ru$	$C_{38}H_{24}CuN_6O_2$
Formula weight	769.80	660.17
Temperature	120(2)K	147(2)K
Wavelength	0.71073Å	0.71073Å
Crystal system	Orthorhombic	Monoclinic
Space group	Pbcn	$P2_1/c$
Unit cell dimensions: a	22.5822(8Å	13.1831(12)Å
b	12.8588(6)Å	22.225(2)Å
c	22.8253(11)Å	12.9700(11)Å
α	90^o	90^o
β	90^o	$118.373(2)^o$
γ	90^o	90^o
Volume	$6628.0(5)Å^3$	$3343.7(5)Å^3$
Z	8	4
Density (calculated)	$1.543Mg/m^3$	$1.311Mg/m^3$
Absorption coefficient	$0.526mm^{-1}$	$0.696mm^{-1}$
F(000)	3152	1356
Crystal size	$0.180x0.100x0.050mm^3$	$0.330x0.200x0.080mm^3$
Theta range for data collection	1.784 to 27.514^o	1.756 to 27.636^o
Index ranges	-29≤h≤20, -16≤k≤15, -22≤l≤29	-17≤h≤17, -28≤k≤28, -16≤l≤16
Reflections collected	34211	58184
Independent reflections	7593 [R(int)=0.0374]	7715 [R(int)=0.0856]
Completeness to theta	99.8%	100.0%
Absorption correction	Semi-empirical from equivalents	Semi-empirical from equivalents
Max. and min. transmission	0.7456 and 0.6873	0.7456 and 0.6306
Refinement method	Full-matrix least-squares on F^2	Full-matrix least-squares on F^2
Data /restraints/parameters	7593/0/469	7715/0/417
Goodness-of-fit on F^2	1.276	1.029
Final R indices [I>2sigma(I)]	R1 =0.0587, wR2=0.1239	R1=0.0517, wR2=0.1159
R indices (all data)	R1=0.0745, wR2=0.1302	R1=0.1252, wR2=0.1423
Extinction coefficient	n/a	n/a
Largest diff. peak and hole	1.006 and $-1.240e.Å^{-3}$	0.486 and $-0.728e.Å^{-3}$

TABLE E.4: Crystal data and structure refinement for 3.5 and 3.6

Property	3.8	5.3
Empirical formula	$C_{38}H_{24}N_6O_6V_2$	$C_{49}H_{34.50}ClCoN_{7.50}O_3$
Formula weight	762.51	870.72
Temperature	147(2)K	147(2)K
Wavelength	1.54178Å	1.54178Å
Crystal system	Monoclinic	Monoclinic
Space group	$P2_1/n$	$P2_1/c$
Unit cell dimensions: a	8.3617(4)Å	15.8960(5)Å
b	10.4391(6)Å	16.4685(6)Å
c	18.2180(9)Å	16.0428(5)Å
α	90^o	90^o
β	$100.116(3)^o$	$107.730(2)^o$
γ	90^o	90^o
Volume	$1565.50(14)Å^3$	$4000.3(2)Å^3$
Z	2	4
Density (calculated)	$1.618Mg/m^3$	$1.446Mg/m^3$
Absorption coefficient	$5.531mm^{-1}$	$4.427mm^{-1}$
F(000)	776	1796
Crystal size	$0.060\text{x}0.010\text{x}0.010mm^3$	$0.100\text{x}0.080\text{x}0.080mm^3$
Theta range for data collection	4.902 to 67.155^o	2.918 to 67.320^o
Index ranges	-9≤h≤9, -12≤k≤12, -21≤l≤20	-18≤h≤18, -19≤k≤19, -19≤l≤19
Reflections collected	25179	79324
Independent reflections	2770 [R(int)=0.0651]	7102 [R(int)=0.0806]
Completeness to theta	99.2%	98.8%
Absorption correction	Semi-empirical from equivalents	Semi-empirical from equivalents
Max. and min. transmission	0.7529 and 0.6344	0.7529 and 0.6196
Refinement method	Full-matrix least-squares on F^2	Full-matrix least-squares on F^2
Data /restraints/parameters	2770/0/235	7102/1/568
Goodness-of-fit on F^2	1.057	1.023
Final R indices [I>2sigma(I)]	R1=0.0369, wR2=0.0960	R1=0.0448, wR2=0.1089
R indices (all data)	R1=0.0482, wR2=0.1015	R1=0.0576, wR2=0.1168
Extinction coefficient	n/a	n/a
Largest diff. peak and hole	0.278 and $-0.342e.Å^{-3}$	0.798 and $-0.525e.Å^{-3}$

TABLE E.5: Crystal data and structure refinement for 3.8 and 5.3

Bibliography

[1] Werner, A. A. Z. *Anorg. Chem* **1897**, *14*.

[2] Jacobs, P. W. *Group theory with applications in chemical physics*; Cambridge University Press, 2005.

[3] Jahn, H. A.; Teller, E. *Proc. R. Soc. London, Ser. A* **1937**, *161*, 220–235.

[4] Murphy, B.; Hathaway, B. *Coord. Chem. Rev.* **2003**, *243*, 237 – 262.

[5] Sessoli, R.; Powell, A. K. *Coord. Chem. Rev.* **2009**, *253*, 2328 – 2341, Deutsche Forschungsgemeinschaft Molecular Magnetism Research Report.

[6] Buenzli, J.-C. G. *Coord. Chem. Rev.* **2015**, *293*, 19–47.

[7] Abbas, G.; Lan, Y.; Kostakis, G. E.; Wernsdorfer, W.; Anson, C. E.; Powell, A. K. *Inorg. Chem.* **2010**, *49*, 8067–8072.

[8] Woods, M.; Woessner, D. E.; Sherry, A. D. *Chem. Soc. Rev.* **2006**, *35*, 500–511.

[9] Kittel, C. *Introduction to solid state*; John Wiley & Sons, 1966.

[10] Benelli, C.; Gatteschi, D. *Introduction to molecular magnetism: From transition metals to lanthanides*; John Wiley & Sons, 2015.

[11] Gispert, J. R. *Coordination chemistry*; Wiley-VCH Weinheim, 2008; Vol. 483.

[12] Miller, J. S.; Epstein, A. J. *Chem. Comm.* **1998**, 1319–1325.

[13] Gütlich, P. *Eur. J. Inorg. Chem.* **2013**, *2013*, 581–591.

[14] Jr., W. A. B.; Bobonich, H. M. *Inorg. Chem.* **1964**, *3*, 1184–1188.

[15] Gamez, P.; Costa, J. S.; Quesada, M.; Aromi, G. *Dalton Trans.* **2009**, 7845–7853.

[16] Krivokapic, I.; Zerara, M.; Daku, M. L.; Vargas, A.; Enachescu, C.; Ambrus, C.; Tregenna-Piggott, P.; Amstutz, N.; Krausz, E.; Hauser, A. *Coord. Chem. Rev.* **2007**, *251*, 364 – 378, A Special Issue Highlighting the Many Aspects of the Electronic Spectrosocpy of Inorganic Compounds.

[17] Hayami, S.; Komatsu, Y.; Shimizu, T.; Kamihata, H.; Lee, Y. H. *Coord. Chem. Rev.* **2011**, *255*, 1981 – 1990, Special Issue: 39th International Conference on Coordination Chemistry.

[18] Klaui, W. *J. Chem. Soc., Chem. Commun.* **1979**, 700–700.

[19] Halepoto, D. M.; Holt, D. G. L.; Larkworthy, L. F.; Leigh, G. J.; Povey, D. C.; Smith, G. W. *J. Chem. Soc., Chem. Commun.* **1989**, 1322–1323.

[20] Hughes, A. K.; Murphy, V. J.; O'Hare, D. *J. Chem. Soc., Chem. Commun.* **1994**, 163–164.

[21] Benmansour, S.; Triki, S.; Gómez-García, C. J. *Magnetochemistry* **2016**, *2*, 1.

[22] Sim, P. G.; Sinn, E. *J. Am. Chem. Soc.* **1981**, *103*, 241–243.

[23] Real, J. A.; Gaspar, A. B.; Munoz, M. C. *Dalton Trans.* **2005**, 2062–2079.

[24] Sciortino, N. F.; Scherl-Gruenwald, K. R.; Chastanet, G.; Halder, G. J.; Chapman, K. W.; Létard, J.-F.; Kepert, C. J. *Angew. Chem. Int. Ed.* **2012**, *51*, 10154–10158.

[25] Neville, S. M.; Leita, B. A.; Halder, G. J.; Kepert, C. J.; Moubaraki, B.; Létard, J.-F.; Murray, K. S. *Chem. Eur. J.* **2008**, *14*, 10123–10133.

[26] Yang, F.-L.; Li, B.; Hanajima, T.; Einaga, Y.; Huang, R.-B.; Zheng, L.-S.; Tao, J. *Dalton Trans.* **2010**, *39*, 2288–2292.

[27] Zhang, L.; Wang, J.-J.; Xu, G.-C.; Li, J.; Jia, D.-Z.; Gao, S. *Dalton Trans.* **2013**, *42*, 8205–8208.

[28] Gütlich, P.; Ksenofontov, V.; Gaspar, A. B. *Coord. Chem. Rev.* **2005**, *249*, 1811–1829.

[29] Tezgerevska, T.; Alley, K. G.; Boskovic, C. *Coord. Chem. Rev.* **2014**, *268*, 23 – 40.

[30] Lis, T. *Acta Crystallogr. Sect. C. Cryst. Struct. Commun.* **1980**, *36*, 2042–2046.

[31] Sessoli, R.; Gatteschi, D.; Caneschi, A.; Novak, M. A. *Nature* **1993**, *365*, 141–143.

[32] Paulsen, C.; Park, J.-G.; Barbara, B.; Sessoli, R.; Caneschi, A. *J. Magn. Magn. Mater.* **1995**, *140*, 1891 – 1892.

[33] Demir, S.; Jeon, I.-R.; Long, J. R.; Harris, T. D. *Coord. Chem. Rev.* **2015**, *289–290*, 149 – 176, Progress in Magnetochemistry.

[34] Rinehart, J. D.; Ming, F.; Evans, W. J.; Long, J. R. *Nat. Chem.* **2011**, *3*, 538 – 542.

[35] Luca, O. R.; Crabtree, R. H. *Chem. Soc. Rev.* **2013**, *42*, 1440–1459.

[36] Kaim, W.; Schwederski, B. *Coord. Chem. Rev.* **2010**, *254*, 1580–1588.

[37] Gamez, P.; Koval, I. A.; Reedijk, J. *Dalton Trans.* **2004**, 4079–4088.

[38] Caneschi, A.; Gatteschi, D.; Sessoli, R.; Rey, P. *Acc. Chem. Res.* **1989**, *22*, 392–398.

[39] Veber, S. L.; Fedin, M. V.; Potapov, A. I.; Maryunina, K. Y.; Romanenko, G. V.; Sagdeev, R. Z.; Ovcharenko, V. I.; Goldfarb, D.; Bagryanskaya, E. G. *J. Am. Chem. Soc.* **2008**, *130*, 2444–2445.

[40] Wallenfels, K.; Bechtler, G.; Kuhn, R.; Trischmann, H.; Egge, H. *Angew. Chem. Int. Ed.* **1963**, *2*, 515–523.

[41] Brook, D. J.; Lynch, V.; Conklin, B.; Fox, M. A. *J. Am. Chem. Soc.* **1997**, *119*, 5155–5162.

[42] Hicks, R. G.; Lemaire, M. T.; Thompson, L. K.; Barclay, T. M. *J. Am. Chem. Soc.* **2000**, *122*, 8077–8078.

[43] Hunter, E. P.; Desrosiers, M. F.; Simic, M. G. *Free Radical Biol. Med.* **1989**, *6*, 581–585.

[44] Witting, P. K.; Mauk, A. G. *J. Biol. Chem.* **2001**, *276*, 16540–16547.

[45] Chaudhuri, P.; Wieghardt, K. *Prog. Inorg. Chem.* **2001**, *50*, 151–216.

[46] Land, E.; Porter, G. *J. Chem. Soc. Faraday Trans.* **1963**, *59*, 2016–2026.

[47] Samanta, S.; Ghosh, P.; Goswami, S. *Dalton Trans.* **2012**, *41*, 2213–2226.

[48] Kaim, W. *Inorg. Chem.* **2011**, *50*, 9752–9765.

[49] Basu, S.; Halder, S.; Pal, I.; Samanta, S.; Karmakar, P.; Drew, M. G.; Bhattacharya, S. *Polyhedron* **2008**, *27*, 2943 – 2951.

[50] Samanta, S.; Ghosh, P.; Goswami, S. *Dalton Trans.* **2012**, *41*, 2213–2226.

[51] Shivakumar, M.; Pramanik, K.; Bhattacharyya, I.; Chakravorty, A. *Inorg. Chem.* **2000**, *39*, 4332–4338.

[52] Antunes, M. A.; Coutinho, J. T.; Santos, I. C.; Marcalo, J.; Almeida, M.; Baldovi, J. J.; Pereira, L. C. J.; Gaita-Arino, A.; Coronado, E. *Chem. Eur. J.* **2015**, *21*, 17817–17826.

[53] Chiswell, B.; Lions, F.; Tomlinson, M. L. *Inorg. Chem.* **1964**, *3*, 492–499.

[54] Bhoon, Y.; Pandeya, K.; Singh, R. *Indian J. Chem.* **1975**, *13*, 84–85.

[55] Pandeya, K.; Singh, R.; Bhoon, Y. *Bull. Soc. Chim. Fr.* **1979**, *I104*.

[56] Pandeya, K.; Singh, R.; Sawhney, G.; Baijal, J. *Solid State Commun.* **1979**, *32*, 823–825.

[57] Pandeya, K.; Singh, R.; Bhoon, Y. *J. Coord. Chem.* **1976**, *6*, 71–74.

[58] Damme, N. V.; Lough, A. J.; Gorelsky, S. I.; Lemaire, M. T. *Inorg. Chem.* **2013**, *52*, 13021–13028.

[59] Damme, N. V.; Zaliskyy, V.; Lough, A. J.; Lemaire, M. T. *Polyhedron* **2015**, *89*, 155–159.

[60] Steinhauser, G.; Giester, G.; Wagner, C.; Leopold, N.; Sterba, J.; Lendl, B.; Bichler, M. *Helv. Chim. Acta* **2009**, *92*, 1371–1384.

[61] Abdel-Latif, S. *Synth. React. Inorg. Met. Org. Chem.* **2001**, *31*, 1355–1374.

[62] Ahlrichs, R.; Bär, M.; Häser, M.; Horn, H.; Kölmel, C. *Chem. Phys. Lett.* **1989**, *162*, 165–169.

[63] Treutler, O.; Ahlrichs, R. *J. Chem. Phys.* **1995**, *102*, 346–354.

[64] Schäfer, A.; Horn, H.; Ahlrichs, R. *J. Chem. Phys.* **1992**, *97*, 2571–2577.

[65] Weigend, F.; Ahlrichs, R. *Phys. Chem. Chem. Phys.* **2005**, *7*, 3297–3305.

[66] Becke, A. D. *Phys. Rev. A. At. Mol. Opt. Phys.* **1988**, *38*, 3098.

[67] Vosko, S. H.; Wilk, L.; Nusair, M. *Can. J. Chem.* **1980**, *58*, 1200–1211.

[68] Perdew, J. P. *Phys. Rev. B: Condens. Matter.* **1986**, *33*, 8822.

[69] Eichkorn, K.; Treutler, O.; Öhm, H.; Häser, M.; Ahlrichs, R. *Chem. Phys. Lett.* **1995**, *240*, 283–290.

[70] Eichkorn, K.; Weigend, F.; Treutler, O.; Ahlrichs, R. *Theor. Chem. Acc.* **1997**, *97*, 119–124.

[71] Sierka, M.; Hogekamp, A.; Ahlrichs, R. *J. Chem. Phys.* **2003**, *118*, 9136–9148.

[72] Bauernschmitt, R.; Häser, M.; Treutler, O.; Ahlrichs, R. *Chem. Phys. Lett.* **1997**, *264*, 573–578.

[73] Deglmann, P.; May, K.; Furche, F.; Ahlrichs, R. *Chem. Phys. Lett.* **2004**, *384*, 103–107.

[74] Becke, A. D. *J. Chem. Phys.* **1993**, *98*, 5648–5652.

[75] Lee, C.; Yang, W.; Parr, R. G. *Phys. Rev. B: Condens. Matter.* **1988**, *37*, 785.

[76] Frisch, M. J. et al. Gaussian09 Revision D.01. Gaussian Inc. Wallingford CT 2009.

[77] Stratmann, R. E.; Scuseria, G. E.; Frisch, M. J. *J. Chem. Phys.* **1998**, *109*, 8218–8224.

[78] Skripnikov, L. Chemissian Version 4.01 Visualization Computer Program. `www.chemissian.com/`, 2015.

[79] Tenderholt, A. QMForge, Version 2.4. `http://qmforge.sourceforge.net/`, 2015.

[80] Zarembowitch, J.; Kahn, O. *Inorganic Chemistry* **1984**, *23*, 589–593.

[81] Bancroft, G.; Mays, M.; Prater, B. *J. Chem. Soc. A. Inorg. phys. theor.* **1970**, 956–968.

[82] Taylor, R. A.; Lough, A. J.; Lemaire, M. T. *J. Mater. Chem. C* **2016**, *4*, 455–459.

[83] Taylor, R. A.; Lough, A. J.; Poddutoori, P. K.; Lemaire, M. T. *Polyhedron* **2016**, *108*, 74 – 79, Modern Canadian Inorganic Chemistry.

[84] Rajput, A.; Sharma, A. K.; Barman, S. K.; Koley, D.; Steinert, M.; Mukherjee, R. *Inorg. Chem.* **2013**, *53*, 36–48.

[85] Oosterhuis, W.; Lang, G. *J. Chem. Phys.* **1969**, *50*, 4381–4387.

[86] Hamada, D.; Fujinami, T.; Yamauchi, S.; Matsumoto, N.; Mochida, N.; Ishida, T.; Sunatsuki, Y.; Tsuchimoto, M.; Coletti, C.; Re, N. *Polyhedron* **2016**, *109*, 120 – 128.

[87] Demir, S.; Nippe, M.; Gonzalez, M. I.; Long, J. R. *Chem. Sci.* **2014**, *5*, 4701–4711.

[88] Jiang, Z.-X.; Liu, J.-L.; Chen, Y.-C.; Liu, J.; Jia, J.-H.; Tong, M.-L. *Chem. Commun.* **2016**, *52*, 6261–6264.

[89] Santos, F. d. S.; Descalzo, R. R.; Goncalves, P. F. B.; Benvenutti, E. V.; Rodembusch, F. S. *Phys. Chem. Chem. Phys.* **2012**, *14*, 10994–11001.

[90] Shuvaev, S.; Utochnikova, V.; Marciniak, L.; Freidzon, A.; Sinev, I.; Van Deun, R.; Freire, R. O.; Zubavichus, Y.; Grunert, W.; Kuzmina, N. *Dalton Trans.* **2014**, *43*, 3121–3136.

[91] Bunzli, J.-C. G.; Piguet, C. *Chem. Soc. Rev.* **2005**, *34*, 1048–1077.

[92] Pramanik, N. C.; Pramanik, K.; Ghosh, P.; Bhattacharya, S. *Polyhedron* **1998**, *17*, 1525–1534.

[93] Bonanno, N. M.; Van Damme, N.; Lough, A. J.; Lemaire, M. T. *Dyes Pigm.* **2015**, *123*, 212–217.